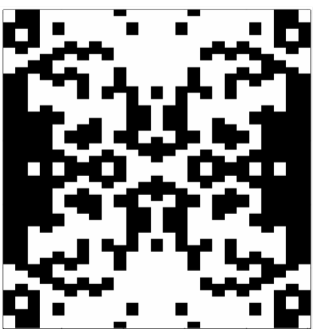


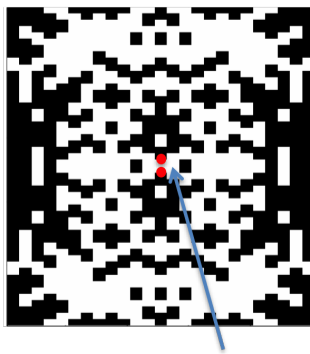
Fragmented Aperture Antennas

Computational Design of Antenna Structure

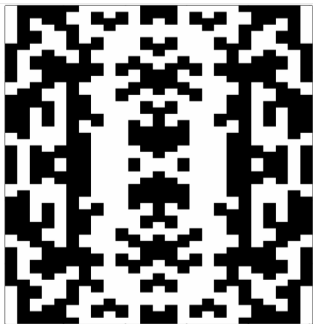
0.5 – 0.8 GHz



0.8 – 1.2 GHz



1.2-1.6 GHz



1.6 – 2.0 GHz



Feed Pt

Dr. James G. Maloney

Inventor of the Fragmented Aperture Antenna

Contents

1	Introduction to Fragmented Aperture Antennas	19
1.1	Overview	19
1.2	Antenna Fundamentals	19
1.2.1	Radiation Pattern	20
1.2.2	Directivity and Gain	20
1.2.3	Aperture and Aperture Efficiency	21
1.2.4	Bandwidth	21
1.2.5	Polarization	21
1.3	Antenna Arrays	22
1.4	Limitations of Traditional Antenna Design	22
1.5	The Fragmented Aperture Concept	23
1.6	Novelty and Significance	24
1.7	Organization of the Book	24
2	Original Approach to Design Fragmented Apertures	27
2.1	Aperture Utilization	27
2.2	Original Genetic Design Approach	27
2.2.1	Binary Encoding of Antenna Geometry	27
2.2.2	Two-Stage Optimization	29
2.2.3	Fitness Evaluation with FDTD	29
2.2.4	Symmetry Constraints	29
2.3	First Success	32
2.4	Bidirectional Radiation	32
2.5	Fragmented Broadband Ground Planes	36
2.6	The Original Patent and Early Publications	36
2.7	Lessons Learned	38
3	Improved Approach to Design Fragmented Apertures	41
3.1	Overview	41
3.2	Limitations with Fragmented Apertures	41
3.3	Initial Approaches to mitigate diagonal touching	44
3.4	Three Improved Fragmented Aperture Antenna Embodiments	46
3.4.1	First Approach	46
3.4.2	Second Approach	47
3.4.3	Third Approach	47

3.5 Improved Mutation Algorithm to Improve Convergence Rate of Fragmented Apertures	47
3.6 Sample Planar Improved Fragmented Aperture Designs	50
3.6.1 First Approach	50
3.6.2 Second Approach	50
3.6.3 Third Approach	54
4 Sample Antenna Design	57
4.1 feed strategies	57
4.2 First Success	57
5 Reconfigurable Fragmented Aperture Antennas	61
5.1 Introduction	61
5.2 The Agile Aperture Antenna Concept	61
5.3 Static Proof of Concept	63
5.4 Reconfigurable Proof of Concept	63
5.4.1 Prototype Description	63
5.4.2 Measurement Setup	63
5.4.3 Design Procedure	64
5.4.4 Broadside Design	64
5.4.5 End-Fire Design	65
5.4.6 Observations on the Designed Configurations	71
5.5 Discussion	71
5.6 Acknowledgement	71
References	71
6 Fragmented Array Elements	73
6.1 Direct Element Design	73
6.2 First Success	73
7 Wideband, Antenna Arrays	77
7.1 Introduction	77
7.2 Fragmented Array Antennas	78
7.3 Wideband Backplanes: Planar 10:1 Arrays	80
7.4 Multi-layer Radiators: 33:1 Bandwidth Arrays	85
7.5 Acknowledgement	94
References	94
8 MetaMaterials and Antennas	95
<i>John Schultz and James G. Maloney</i>	
8.1 Introduction To MetaMaterials	95
8.2 Slicing	95
8.2.1 examples	95
8.3 Dicing	95
A Computational Modeling of Antennas	99

A.1	Acknowledgement	99
A.2	Introduction	99
A.3	The Basic FDTD Algorithm	100
A.4	Formulation of the Antenna Problem in the FDTD Method	103
A.4.1	Transmitting Antenna	104
A.4.2	Receiving Antenna	107
A.4.3	Reciprocity	108
A.4.4	Frequency Domain	108
A.5	Examples of the Use of the Method for Antenna Analysis	111
A.5.1	Cylindrical Monopole: Theoretical Model Versus Experimental Model	111
A.5.2	Metallic Horns and Spirals: Stair-Stepped Surfaces	120
A.5.3	Microstrip Patches: Excessive Ringing for Narrow-Band Antennas	131
A.6	Summary and Conclusions	138

List of Figures

2.1	The fragmented aperture concept: a planar surface divided into a grid of sub-wavelength pixels, each either conducting (black) or non-conducting (white). The pattern of conducting and non-conducting elements defines the antenna geometry [1].	28
2.2	First optimization stage: the aperture is described using trapezoidal conducting strips of variable length arranged about a coaxial feed. This coarse parameterization enables rapid exploration of the design space [1].	30
2.3	Flowchart of the genetic optimization process for fragmented aperture design. The algorithm iteratively toggles pixels between conducting and non-conducting states, evaluating the antenna performance at each step using full-wave electromagnetic simulation [1].	31
2.4	The first successful fragmented aperture antenna: a 10-inch \times 10-inch aperture optimized for 800 MHz to 2.5 GHz. The complex pattern of conducting (black) and non-conducting (white) regions was determined entirely by the genetic algorithm and FDTD simulation. The feed is located at the right side of the aperture. Left-right and top-bottom symmetry lines are indicated by the dashed lines [1].	33
2.5	Measured and predicted broadside gain for the first fragmented aperture antenna (Figure 2.4). The fragmented design closely approaches the uniform aperture gain limit across the 800 MHz to 2.5 GHz optimization range, and significantly outperforms a spiral antenna of the same aperture size. The measured and FDTD-predicted gains are in excellent agreement [1].	34
2.6	H-plane radiation pattern of the first fragmented aperture antenna, comparing the measured pattern with the FDTD model prediction. The pattern is clearly bidirectional, with roughly equal radiation into the forward and backward hemispheres [1].	35
2.7	Transmission phase comparison demonstrating the broadband properties of a fragmented surface [1].	37
3.1	Original Fragmented Aperture approach based on lattice of rectangular areas. An example of diagonal touching is shown in the top right of the figure.	42

3.2 Generalized Fragmented Aperture Approach based on parallelograms. Again, an example of diagonal touching is shown in the top right of the figure	43
3.3 (a) Over-etching causing diagonal elements not to touch as shown in top center, (b) close photograph of a etched copper fragmented antenna showing over etch disconnecting diagonal fragments.	43
3.4 Two sample designs from original fragmented patent exhibiting diagonal touching [5]. The most troublesome examples of diagonal-touching near the antenna feed are circled	44
3.5 (a) Super-cell approach; e.g. 3x3 plus signs, (b) Ten Percent Larger Fabrication, (c) Small metal square to ensure contact, (d) Random coin flipping approach	45
3.6 First Approach to Improved Fragmented Aperture Antennas.	46
3.7 Second Approach to Improved Fragmented Aperture Antennas.	47
3.8 Third Approach to Improved Fragmented Aperture Antennas.	48
3.9 Third Approach to Improved Fragmented Aperture Antennas.	49
3.10 Fragmented Aperture shapes of the Improved Fragmented aperture sample designs.	51
3.11 Gain summary of First Approach Sample Designs shown in Figure 3.10. .	52
3.12 VSWR summary of First Approach Sample Designs shown in Figure 3.10.	53
3.13 Two sample designs from the second approach	53
3.14 Gain summary of second approach sample designs shown in Figure 3.13 .	54
3.15 VSWR summary of second approach sample designs shown in Figure 3.13	55
3.16 Four sample designs from the third approach: (a) Broadside Vpol, (b) Broadside Hpol, (c) Broadside slant linear polarization, (d) Vpol Beam Steered 45° from broadside	55
3.17 Gain summary of third approach sample designs shown in Figure 3.13 .	55
3.18 VSWR summary of third approach sample designs shown in Figure 3.13 .	55
3.19 Azimuth Gain Pattern summary at midband of third approach sample designs shown in Figure 3.13	55
4.1 Comparison of fragmented design to uniform aperture limit $2\pi A/\lambda^2$.	58
5.1 Schematic drawing of the Agile Aperture Antenna in dipole form. Square metallic pads are connected by switched links (arrows). The state of each switch (open or closed) determines the antenna configuration [3]. .	62
5.2 Experimental arrangement for measuring the Agile Aperture Antenna in monopole form. The antenna is mounted vertically on a rotatable disc centered in a large metallic image plane [3].	64
5.3 Switch configurations for the Agile Aperture Antenna (monopole form) with hard-wired switches. (a) Broadband, bidirectional, broadside design. (b) Narrowband, unidirectional, end-fire design. The two configurations are strikingly different, yet both are realized on the same physical antenna [3].	66

5.4	Results for the broadband, bidirectional, broadside design with hard-wired switches. (a) Realized gain versus frequency. (b) Gain reduction due to impedance mismatch: $(1 - \Gamma_A ^2)$ [3].	67
5.5	Horizontal radiation pattern at $f = 1.05$ GHz for the broadband, bidirectional, broadside design with hard-wired switches. Both patterns are normalized to 0 dB [3].	68
5.6	Results for the narrowband, unidirectional, end-fire design with hard-wired switches. (a) Realized gain versus frequency. (b) Gain reduction due to impedance mismatch: $(1 - \Gamma_A ^2)$ [3].	69
5.7	Horizontal radiation pattern at $f = 1.05$ GHz for the narrowband, unidirectional, end-fire design with hard-wired switches. Both patterns are normalized to 0 dB [3].	70
6.1	Comparison of fragmented design to uniform aperture limit $2\pi A/\lambda^2$. .	74
7.1	This design experiment compared performance of two 8x8 arrays. (a) Connected array element, (b) Unconnected array element, (c) Embedded element gain comparison for a central element in an 8x8 array. Notice that the connected array element far out performs the unconnected element. [Used with permission of Wiley]	78
7.2	The connected element from Figure 7.1 was simulated in arrays of various sizes. The results show that the low-frequency performance limit is essentially proportional to overall array size. [Used with permission of Wiley]	79
7.3	Embedded element realized gain for a central element of a 10 x 17 array with 3-cm square unit cells. [Used with permission of Wiley]	80
7.4	When a broadband radiating sheet is placed in front of a simple PEC ground plane, the resulting gain pattern will suffer nulls at frequencies where the separation distance is an integer multiple of a half wavelength (in this case, 6 GHz for a 2.5 cm separation). [Used with permission of Wiley]	81
7.5	For normal incidence (or when a phased array is scanned to broadside) pattern nulls will occur when the ground plane is at a half wavelength separation. At scan angles off normal, the null will occur at higher frequencies. This geometry is illustrated in the diagram on the left above. The contour plot on the right shows the relationship between field intensity at the radiating surface and frequency and angle for a 2.5 cm separation. [Used with permission of Wiley]	82
7.6	Here the radiating surface is located 2.5 cm in front of the PEC ground plane, but a 377-ohms/square r-card layer is placed halfway between radiator and ground plane, eliminating the deep null at $\lambda/2$. [Used with permission of Wiley]	82
7.7	This plot of the normalized realized gain at broadside for the configuration of Figure 8 shows that the deep null at 6 GHz has been improved to only 3 dB insertion loss. [Used with permission of Wiley]	83

7.8	The first array built using the broadband screen backplane was this 10:1 design. Efficiency was better than 50% (< 3 dB insertion loss) from 1 to 10 GHz. [Used with permission of Wiley]	84
7.9	Aperture fields 3 inches in front of a PEC surface, with and without a broadband screen backplane in place. [Used with permission of Wiley] . .	84
7.10	Contour plots comparing the configurations of Figure 7.9 over a range of scan angles. [Used with permission of Wiley]	85
7.11	Thought experiment demonstrating the benefit of preferentially radiating in one direction to mitigate ground plane nulls. This is possible with asymmetric radiation, which can be achieved with a radiator thickness \neq 0. [Used with permission of Wiley]	86
7.12	Idealized design with simultaneously optimized radiating layers. The design goal was to maximize front-to-back ratio. [Used with permission of Wiley]	87
7.13	The use of parasitic layers to direct radiation forward may also be accomplished in the presence of a PEC backplane, as in this example, where insertion loss is kept below 2 dB over most of a 10:1 bandwidth. [Used with permission of Wiley]	87
7.14	Design experiments with two and three radiating face sheets. The ground plane has been replaced in each simulation with a perfectly absorbing layer as the back boundary condition. Thus, normalized gain levels above -3 dB may be attributed to the F/B ratio. [Used with permission of Wiley]	88
7.15	Predicted performance of the 33:1 antenna design. In this periodic simulation, antenna efficiency is shown to be better than 50% over the entire bandwidth of 0.3-10 GHz for an actual antenna designed with realistic feed structures. [Used with permission of Wiley]	89
7.16	Construction details of one 33:1 antenna design, including a photo of the test piece used to measure embedded element realized gain (EERG). [Used with permission of Wiley]	90
7.17	The plot shows a compilation of measured data at broadside for the 33:1 test antenna (3 antenna ranges, two polarizations). The measured data is plotted against numerical predictions of performance, along with the element area gain representing ideal performance. [Used with permission of Wiley]	91
7.18	Comparison of modeled (solid lines) and measured (data markers) EERG pattern cuts at several discrete frequencies. Again, note the excellent agreement between prediction and measurement. [Used with permission of Wiley]	92
7.19	Compilation of measured angle cuts normalized to the maximum value at each frequency. Resulting contours indicate achievable scan volume. Note the lack of scan blindness in the operating regions. [Used with permission of IEEE]	92
7.20	Results of several design exercises for fragmented arrays. For air-filled cavities, the antenna thickness is approximately $l/12$ at the lowest operating frequency. [Used with permission of IEEE]	93

8.1	Schematic drawing showing the computational volume, FDTD spatial lattice, and unit cell.	96
A.1	Schematic drawing showing the computational volume, FDTD spatial lattice, and unit cell.	101
A.2	Numerical dispersion as a function of the number of cells per wavelength, N_λ , for a time-harmonic plane wave propagating along one of the axes of an FDTD lattice of cubical cells. Solid line, the relative error in the phase velocity in percent. Dashed line, the error in the phase per cell in degrees. $S = 0.5$	103
A.3	(a) Schematic drawing showing the basic elements involved in the FDTD analysis of a transmitting antenna. (b) Details for the near-field to far-field transformation.	105
A.4	The details for the feed region of (a) the transmitting antenna and (b) the receiving antenna. The characteristic impedance of the transmission line is R_o , and the source and termination are matched to this impedance	106
A.5	(a) Schematic drawing showing the basic elements involved in the FDTD analysis of a receiving antenna. (b) Details for the plane-wave source. .	109
A.6	(a) The Gaussian pulse (solid line) and the differentiated Gaussian pulse (dashed line) and the magnitude of their Fourier transforms. (b) The sinusoid of frequency amplitude modulated by a Gaussian pulse and the magnitude of its Fourier transform, . All waveforms are normalized to have a maximum value of 1.0.	112
A.7	(a) Cylindrical monopole antenna fed through an image plane from a coaxial transmission line. (b) FDTD model for the cylindrical monopole antenna. The PML that surrounds the computational space is not shown.	113
A.8	Comparision of theoretical and measured results for the cylindrical monopole antenna. (a) Reflected voltage in the coaxial line. (b) Electric field on the image plane at $\rho/h = 12.7$	115
A.9	Three snapshots in time showing the magnitude (right) and direction (left) of the Poynting vector surrounding the cylindrical monopole antenna: (a) near the coaxial aperture at time , (b) near the open end of the monopole at time , and (c) around the whole structure at time . Logarithmic scaling is used for both plots. Notice that (a) and (b) only show a portion of the monopole. (After Smith and Hertel [17], 2001 IEEE.) .	116
A.10	Comparison of theoretical and measured results for the input admittance of the cylindrical monopole antenna. Results are shown for three levels of discretization (A, B, C) in the FDTD method. (After Hertel and Smith [18], 2003 IEEE.)	118
A.11	Simplified models for the cylindrical monopole antenna. (a) Model incorporating a ?hard source.? (b) Model incorporating a virtual one-dimensional transmission line. The monopole conductor has a square cross section in both models.	119
A.12	Comparison of theoretical and measured results for the input admittance of the cylindrical monopole antenna. Results are shown for the two simplified FDTD models. (After Hertel and Smith [18], 2003 IEEE.)	120

A.13 (a) Rectangular FDTD lattice superimposed on the cross section of an object that is a perfect electric conductor (PEC). (b) The surface of the object has been deformed to conform to the rectangular lattice; the surface of the object has been replaced by a stair-stepped approximation.	121
A.14 Schematic drawing for the pyramidal horn antenna. The inset shows the FDTD cells used to model the bottom of the horn.	122
A.15 Comparison of theoretical and measured results for the pyramidal horn antenna. (a) E-plane pattern and (b) H-plane pattern at 10 GHz. (c) Boresite gain versus frequency.	124
A.16 Gray scale plots for the magnitude of the electric field on the vertical symmetry plane of the transmitting horn antenna. The excitation is a sinusoid amplitude modulated by a Gaussian pulse.	126
A.17 Geometry for the two-arm conical spiral antenna. (After Hertel and Smith [26], 2002 IEEE.)	127
A.18 Schematic drawing showing the arrangement of FDTD cells used to model the conical spiral antenna. For clarity, only the lower 10% of the antenna is shown. (After Hertel and Smith [26], 2002 IEEE.)	128
A.19 Comparison of theoretical and measured results for the conical spiral antenna. (a) Magnitude of reflection coefficient versus frequency. (b) Realized gain in the boresite direction versus frequency. (After Hertel and Smith [26], 2002 IEEE.)	129
A.20 Gray scale plots for the magnitude of the electric field near the conical spiral antenna for three instants in time: (a) $t/\tau_L = 0.1$, (b) $t/\tau_L = 0.6$, and (c) $t/\tau_L = 1.1$, where τ_L is the time for light to travel the length of the spiral arm. (After Hertel and Smith [27], 2003 IEEE.)	130
A.21 (a) Schematic drawing for the TEM horn antenna (monopole configuration). (b) Cross sections showing the stair-stepped approximation to the plate for two different cases, A and B.	132
A.22 Results for two different stair-stepped approximations (A and B) applied to the TEM horn antenna. (a) The reflected voltage in the feeding transmission line; the reflection from the open end of the horn has been windowed out. (b) The magnitude of the Fourier transform of the reflection coefficient for the antenna.	133
A.23 Rectangular microstrip patch antenna fed by a coaxial line probe.	134
A.24 The magnitude of the reflected voltage in the feeding coaxial line versus the normalized time. (a) Rectangular microstrip patch. (b) Narrow-band, rectangular microstrip patch.	136
A.25 Comparison of theoretical and measured results for the rectangular microstrip patch antenna. (a) Magnitude of reflection coefficient versus frequency. (b) Field patterns for E and H planes at the frequency $f = 6.8$ GHz. Measured results from [33]	137
A.26 Narrow-band, rectangular microstrip patch antenna. Magnitude of reflection coefficient versus frequency for three different numbers of time steps.	139

- A.27 Number of documents published over the a twenty year span that include the words ?finite-difference time-domain? or ?FDTD? in the title. Each bar shows the total number of documents published during a five year period. 140

List of Tables

3.1 Comparison across the three convergence trials (Higher number is better)	49
A.1 Characteristics for Various Input Signals	111

Dedicated to my wife Kate, my children Kelsey, Emily, Grace and Sam.

Acknowledgements

Over the years, I have had the pleasure to work with many smart individuals who each contributed to the development of Fragmented Aperture Antennas.

For my whole career, Prof. Glenn Smith has always be a major supporter of my research efforts. Starting with teaching me how to do research during my Ph.D. thesis, to discussing many research issues over coffee during my university lab years, to co-authoring many book chapters with me, to helping invent the Fragmented Aperture, Dr Smith became a treasured collaborator and friend.

In the early years, I had the good fortune to work with one of the brightest minds, Dr. Morris Kesler. Morris was also one of the co-inventors of the Fragmented Aperture. Morris also assisted me in writing book chapters on Modeling Periodic Structures that are used in the analysis and design of phased array antennas and other periodic structures.

I had many conversations with Dr. Eric Kuster when stuck on a research topic, and his non-engineer view point was very helpful to me over the years.

I would like to thank Mr. Paul Friederich, Dr. Lon Pringle, Mr. Jim Acree for their dedicated support as project directors for both the research on Fragmented Apertures and for helping advocate for customer solutions based on Fragmented Apertures.

In the later years, the development of Fragmented Aperture solutions for many diverse applications were impacted by the assistance of Mr. Brad Baker, Mr. Kevin Cook, Dr. Doug Denison, Ms. Lynn Fountain, Mr. James Fraley, Mr. David Landgren, and Dr. Todd Lee.

The fabrication of many of the Fragmented Apertures relied heavily on the machining skills of the best machinist I ever met, Mr. Kurt Weismayer. Without Kurt's skills, many of the antennas certainly would not have been built exactly, and the measured RF performance would have been in worse agreement with the model predictions.

I also have greatly enjoyed working closely with Dr. John Schultz over the last 10+ years. Collaborating with John on many research projects has been rewarding. Specifically, learning from John about the design of metamaterials and collaborating on their use with Fragmented antennas was always a pleasure.

Lastly, I want to thank Ms. Rebecca Schultz and Dr. Kate Malone for allowing me to assist Compass Technology Groups research efforts over the last few years. Also, I would like to thank them for their support in further developing the Fragment Aperture antenna.

Chapter 1

Introduction to Fragmented Aperture Antennas

1.1 Overview

This book describes a class of antennas called Fragmented Aperture Antennas. Unlike traditional antennas whose physical shapes are guided by analytical insight and engineering intuition, fragmented aperture antennas are designed computationally. A planar conducting surface is divided into many sub-wavelength regions, or pixels, each of which may be either conducting or non-conducting. A genetic algorithm, working in concert with a full-wave electromagnetic simulation, determines which pixels should be conducting and which should not, so as to best satisfy a given set of antenna performance requirements. The resulting antenna structures are complex, non-intuitive metallic patterns that often approach the theoretical limits of antenna performance for a given aperture size.

The fragmented aperture concept was invented in the late 1990s [1], and the term “Fragmented Aperture Antenna” was coined by the author upon visual inspection of the optimized designs, which consistently showed metallic pixels forming many connected and disconnected fragments across the aperture surface. Since then, the concept has been extended to reconfigurable antennas, ultra-wideband phased arrays with bandwidths exceeding 33:1, and metamaterial-enhanced designs. Fragmented aperture antennas have been successfully designed, fabricated, and measured for a wide variety of applications spanning frequencies from UHF through millimeter wave.

This introductory chapter provides background on fundamental antenna concepts, motivates the need for a computational approach to antenna design, introduces the fragmented aperture concept, and concludes with a roadmap for the remainder of the book.

1.2 Antenna Fundamentals

An antenna is a transducer between guided electromagnetic waves, such as those on a transmission line or waveguide, and free-space electromagnetic waves that propagate

away from the antenna. When used for transmission, an antenna converts a guided signal into radiation; when used for reception, it captures incident radiation and converts it into a guided signal. By the principle of reciprocity, the properties of an antenna are the same whether it is transmitting or receiving [2].

Several key parameters characterize the performance of an antenna:

1.2.1 Radiation Pattern

The radiation pattern describes the spatial distribution of electromagnetic energy radiated by an antenna as a function of direction. It is typically represented as a plot of radiated power (or field strength) versus angle, normalized to the direction of maximum radiation. Important features of the radiation pattern include the main beam (or main lobe), which is the angular region of strongest radiation; the sidelobes, which are regions of lesser radiation surrounding the main beam; and the back lobe, which is radiation in the direction opposite the main beam. The beamwidth, usually defined as the angular width between the half-power (-3 dB) points of the main beam, quantifies how directional the antenna is.

1.2.2 Directivity and Gain

Directivity is a measure of how effectively an antenna concentrates radiated energy in a particular direction compared to an isotropic radiator (a hypothetical antenna that radiates equally in all directions). The directivity D in a given direction is defined as the ratio of the radiation intensity in that direction to the radiation intensity averaged over all directions:

$$D = \frac{U(\theta, \phi)}{U_{\text{avg}}} = \frac{4\pi U(\theta, \phi)}{P_{\text{rad}}} \quad (1.1)$$

where $U(\theta, \phi)$ is the radiation intensity (power per unit solid angle) and P_{rad} is the total radiated power.

Gain is closely related to directivity but also accounts for losses within the antenna. The gain G is related to the directivity D by the radiation efficiency η :

$$G = \eta D \quad (1.2)$$

where η accounts for ohmic and dielectric losses in the antenna structure.

In practice, it is often useful to work with the *realized gain*, which further accounts for impedance mismatch between the antenna and its feed:

$$G_{\text{realized}} = (1 - |\Gamma|^2) G \quad (1.3)$$

where Γ is the voltage reflection coefficient at the antenna terminals. The realized gain captures the overall effectiveness of the antenna in converting guided-wave power into radiation in a given direction.

1.2.3 Aperture and Aperture Efficiency

A fundamental result in antenna theory relates the maximum achievable gain of an antenna to its physical aperture area A :

$$G_{\max} = \frac{4\pi A}{\lambda^2} \quad (1.4)$$

where λ is the free-space wavelength. This result applies to a uniformly illuminated aperture radiating into one hemisphere (i.e., with a ground plane or reflector behind it). For an aperture that radiates equally into both hemispheres (no ground plane), the limit becomes $2\pi A/\lambda^2$.

The aperture efficiency η_a describes how closely an antenna approaches this theoretical limit:

$$\eta_a = \frac{G}{G_{\max}} = \frac{G\lambda^2}{4\pi A} \quad (1.5)$$

Traditional antenna designs rarely achieve aperture efficiencies above 50–70%. As will be shown throughout this book, fragmented aperture antennas routinely approach the theoretical aperture gain limit, often achieving efficiencies that exceed those of conventional designs.

1.2.4 Bandwidth

Every antenna has a finite bandwidth over which it operates satisfactorily. Bandwidth may be defined in terms of several criteria, but the most common is the impedance bandwidth: the range of frequencies over which the antenna maintains an acceptable impedance match to its feed line. A common threshold is a voltage standing wave ratio (VSWR) of 2:1, corresponding to a return loss of approximately 10 dB, meaning that no more than 10% of the incident power is reflected back to the source. More demanding applications may require a VSWR below 1.5:1 (return loss better than 14 dB) or even 1.3:1.

Bandwidth can be expressed as a ratio of the upper to lower frequency limits (e.g., 10:1 bandwidth for an antenna operating from 1 to 10 GHz) or as a fractional bandwidth:

$$\text{BW}_{\text{frac}} = \frac{f_H - f_L}{f_c} \quad (1.6)$$

where f_H and f_L are the upper and lower frequency limits and f_c is the center frequency. Antennas with bandwidths of 2:1 or greater are often called wideband, while those exceeding roughly 10:1 are called ultra-wideband.

Achieving wide bandwidth while maintaining high gain and an acceptable impedance match is one of the central challenges in antenna design and a particular strength of the fragmented aperture approach.

1.2.5 Polarization

The polarization of an antenna describes the orientation of the electric field vector of the radiated wave. Common polarizations include linear (vertical or horizontal), circular (right-hand or left-hand), and elliptical. The polarization of the radiated field is

determined by the currents flowing on the antenna structure, and achieving a desired polarization is an important design goal. Fragmented aperture antennas can be designed for any of these polarizations, including cases where the polarization varies with beam direction.

1.3 Antenna Arrays

A single antenna element has a radiation pattern determined by its geometry and size. To achieve higher gain, narrower beams, or the ability to steer the beam electronically, multiple antenna elements are arranged in an array. In an array, the signals from the individual elements combine coherently, and the resulting radiation pattern is the product of the individual element pattern and the array factor, which depends on the element spacing, number of elements, and the relative amplitude and phase of the excitation at each element.

Electronic beam steering is accomplished by adjusting the relative phases of the signals at each element. This is the basis of the phased array, which can rapidly redirect its beam without physically moving the antenna. Phased arrays are essential in modern radar, communications, and electronic warfare systems.

However, the design of wideband phased arrays presents significant challenges. Mutual coupling between array elements—the electromagnetic interaction between neighboring elements—can cause scan blindness, a condition where the array is poorly matched at certain combinations of frequency and scan angle. Traditional array design approaches attempt to minimize mutual coupling, but as will be shown in this book, the fragmented aperture approach embraces mutual coupling, and in some cases exploits direct electrical connections between elements to achieve bandwidths that far exceed those of conventional array elements.

1.4 Limitations of Traditional Antenna Design

Traditional antenna design relies on a library of known antenna types—dipoles, patches, horns, spirals, log-periodic structures, and others—each with well-understood behavior that can be predicted analytically or with simple numerical models. The designer selects an antenna type appropriate for the application and then adjusts a relatively small number of geometric parameters (lengths, widths, feed positions, spacings) to optimize performance.

This approach has been enormously successful and has produced the antenna designs in widespread use today. However, it is inherently constrained by the set of geometries that have been studied and understood. The designer is limited to exploring variations within known antenna topologies. The number of degrees of freedom available for optimization is small—typically fewer than a dozen parameters—and the design space is correspondingly limited.

Consider, by contrast, an antenna aperture divided into a grid of 200 sub-wavelength pixels, each of which may be independently set to conducting or non-conducting. This seemingly simple description defines a design space of $2^{200} \approx 10^{60}$ possible antenna geometries. The vast majority of these configurations have never been conceived by

any antenna designer, and many of them produce antenna characteristics that are unlike any known antenna type. The challenge, of course, is finding the configurations that produce useful antennas among this enormous number of possibilities.

This is precisely the challenge that the fragmented aperture design approach addresses.

1.5 The Fragmented Aperture Concept

The fragmented aperture antenna design approach combines three essential elements:

1. **A pixelated aperture.** The antenna surface is divided into a grid of sub-wavelength regions, or pixels. Each pixel is assigned a binary state: conducting (metal) or non-conducting (absent). The set of all pixel states defines the antenna geometry. Early fragmented apertures used rectangular pixels on a rectilinear grid, but as described in Chapter 3, improved pixel shapes and lattice geometries have been developed to address fabrication challenges.
2. **A full-wave electromagnetic simulation.** A rigorous numerical solution of Maxwell's equations is used to predict the antenna performance for any given pixel configuration. The finite-difference time-domain (FDTD) method has been used exclusively in the author's work because a single time-domain simulation efficiently produces antenna characteristics across the entire frequency band of interest. A detailed description of the FDTD method as applied to antennas is provided in Appendix A.
3. **An evolutionary optimization algorithm.** Because the design space is far too large for exhaustive search, a genetic algorithm (GA) is used to efficiently explore the space of possible pixel configurations. The GA maintains a population of candidate antenna designs, evaluates each design using the FDTD simulation, and evolves the population over many generations using selection, crossover, and mutation operations. The algorithm converges toward designs that best satisfy the specified performance goals.

The result of this design process is an antenna whose physical structure has been computationally optimized to meet a particular set of performance requirements. The antenna shapes that emerge from this process are invariably complex and non-intuitive. Inspection of the metallic regions on the aperture reveals many interconnected and isolated fragments of conductor—hence the name *fragmented aperture*.

A critical advantage of this approach is that the full-wave simulation captures all of the relevant physics: mutual coupling, surface wave effects, feed interactions, dielectric loading, and diffraction from edges and discontinuities. The optimizer therefore has access to the true electromagnetic behavior of each candidate design, not an approximate or simplified model. This is what allows fragmented aperture designs to routinely approach theoretical performance limits.

1.6 Novelty and Significance

The fragmented aperture antenna represents a fundamentally different philosophy of antenna design. Rather than starting from an analytical understanding of how a particular geometric shape radiates and then perturbing that shape to improve performance, the fragmented aperture approach starts from a general description of the design space (the set of all possible pixel configurations) and uses computation to discover structures that meet the desired specifications. In this sense, the antenna structure itself is the output of the design process, not the input.

This computational approach to designing antenna structure has produced several notable results:

- Single-element fragmented aperture antennas that approach the theoretical aperture gain limit $2\pi A/\lambda^2$ for apertures without a ground plane, across bandwidths exceeding an octave.
- Reconfigurable fragmented aperture antennas (Agile Aperture Antennas) that can electronically switch between different operating modes—changing beam direction, bandwidth, or polarization—by opening and closing switched links between metallic pads.
- Ultra-wideband phased array elements based on the fragmented aperture concept that achieve bandwidths of 33:1, with preliminary work suggesting that 100:1 bandwidths are achievable. A key insight enabling these designs was that electrical connections between array elements should be exploited rather than avoided.
- Improved pixel geometries that eliminate the fabrication issue of “diagonal touching”—a problem that plagued early fragmented aperture designs and caused poor agreement between modeled and measured antenna performance.
- An improved mutation algorithm for the genetic algorithm that significantly accelerates convergence for designs with large numbers of pixels.

These results, and others, are described in detail in the chapters that follow.

1.7 Organization of the Book

The remainder of this book is organized as follows:

Chapter 2: Original Approach to Design Fragmented Apertures. This chapter describes the original fragmented aperture concept as disclosed in U.S. Patent 6,323,809. The genetic algorithm design approach is presented, along with early design results that demonstrated the viability of the concept.

Chapter 3: Improved Approach to Design Fragmented Apertures. The original fragmented aperture approach suffered from the problem of diagonal touching, where pixels that touch only at corners lead to fabrication difficulties and poor model-measurement agreement. This chapter presents three improved pixel geometries that inherently avoid diagonal touching, along with an improved mutation algorithm that accelerates the convergence of the genetic algorithm for designs with many pixels.

Chapter 4: Sample Antenna Designs. This chapter presents a gallery of fragmented aperture antenna designs that illustrate the versatility of the approach. Topics include various feed strategies, bandwidth tailoring, fixed beam steering, polarization control (linear and circular), beamwidth tailoring, and out-of-band rejection.

Chapter 5: Reconfigurable Fragmented Aperture Antennas. This chapter describes the Agile Aperture Antenna, a reconfigurable antenna in which switched links between metallic pads allow the antenna to be electronically reconfigured to meet different performance specifications. Static and reconfigurable proof-of-concept designs are presented with measured results.

Chapter 6: Fragmented Array Elements. This chapter extends the fragmented aperture concept to the design of individual elements for phased array antennas. The approach for incorporating scan performance into the design process is described, and example designs spanning multiple octaves of bandwidth are presented.

Chapter 7: Wideband Antenna Arrays. This chapter describes the development of ultra-wideband phased arrays using fragmented aperture design principles. Key innovations include connected arrays, broadband screen backplanes using resistive card layers to mitigate ground-plane nulls, and multi-layer radiators for improved front-to-back ratio. Measured results for arrays with bandwidths up to 33:1 are presented.

Chapter 8: Metamaterials and Antennas. This chapter, co-authored with Dr. John Schultz, explores the intersection of metamaterial design and fragmented aperture antennas. Techniques for designing metamaterial structures using slicing and dicing approaches are presented.

Chapter 9: Reconfigurable Arrays. This chapter describes reconfigurable phased array antennas that combine the fragmented aperture design approach with electronic reconfiguration, enabling improved scan performance and dynamic polarization control.

Appendix A: Computational Modeling of Antennas. This appendix provides a self-contained introduction to the finite-difference time-domain (FDTD) method as applied to antenna analysis. The basic algorithm is described, the formulation for both transmitting and receiving antennas is presented, and several examples are provided to illustrate the accuracy and utility of the method.

References

- [1] J. G. Maloney, M. P. Kesler, P. H. Harms, T. L. Fountain and G. S. Smith, “The fragmented aperture antenna: FDTD analysis and measurement”, Proc. ICAP/JINA Conf. Antennas and Propagation, 2000, pg. 93.
- [2] IEEE Standard for Definitions of Terms for Antennas, IEEE Std 145-2013.
- [3] J.G. Maloney, M.P. Kesler, P.H. Harms, and G.S. Smith, Fragmented Aperture Antennas and Broadband Ground Planes, U.S. Patent, No. 6,323,809 B1, November 27, 2001.
- [4] J. Maloney, J. Fraley, M. Habib, J. Schultz, K. C. Maloney, “Focused Beam Measurement of Antenna Gain Patterns”, AMTA, 2012.

- [5] John W. Schultz, Focused Beam Methods, 2012.
- [6] David Reid, A full electromagnetic analysis of fresnel zone plate antennas and the application to a free-space focused-beam measurement system, PhD. Thesis, Georgia Tech, Nov. 2009.

Chapter 2

Original Approach to Design Fragmented Apertures

2.1 Aperture Utilization

A central goal in antenna design is to make effective use of the available aperture area. As discussed in Chapter 1, the theoretical maximum gain for a uniformly illuminated planar aperture of area A radiating into one hemisphere is $4\pi A/\lambda^2$, and for an aperture radiating into both hemispheres (no ground plane), the limit is $2\pi A/\lambda^2$. Traditional antenna designs—dipoles, patches, spirals, and the like—typically utilize only a fraction of the available aperture area at any given frequency. For example, a spiral antenna uses an “active region” whose size scales with frequency; at any given operating frequency, much of the physical aperture is not contributing to the radiation.

The original fragmented aperture concept was motivated by a simple question: *can one design a planar antenna that utilizes the entire aperture area across a wide frequency band, thereby approaching the theoretical gain limit?* The answer, as demonstrated in this chapter, is yes—provided one is willing to abandon traditional antenna geometries in favor of computationally optimized structures.

2.2 Original Genetic Design Approach

2.2.1 Binary Encoding of Antenna Geometry

The fundamental idea behind the fragmented aperture antenna is to represent the antenna geometry as a binary string that can be manipulated by an evolutionary optimization algorithm. The antenna surface is divided into a grid of sub-wavelength rectangular pixels, as illustrated in Figure 2.1. Each pixel is assigned a single binary value: 1 for conducting (metal present) and 0 for non-conducting (metal absent). The collection of all pixel states defines the antenna geometry and constitutes the “genetic code” of the antenna.

This binary representation maps naturally onto a genetic algorithm (GA). The

RANDOM PATTERN OF CONDUCTING AND NON-CONDUCTING ELEMENTS.

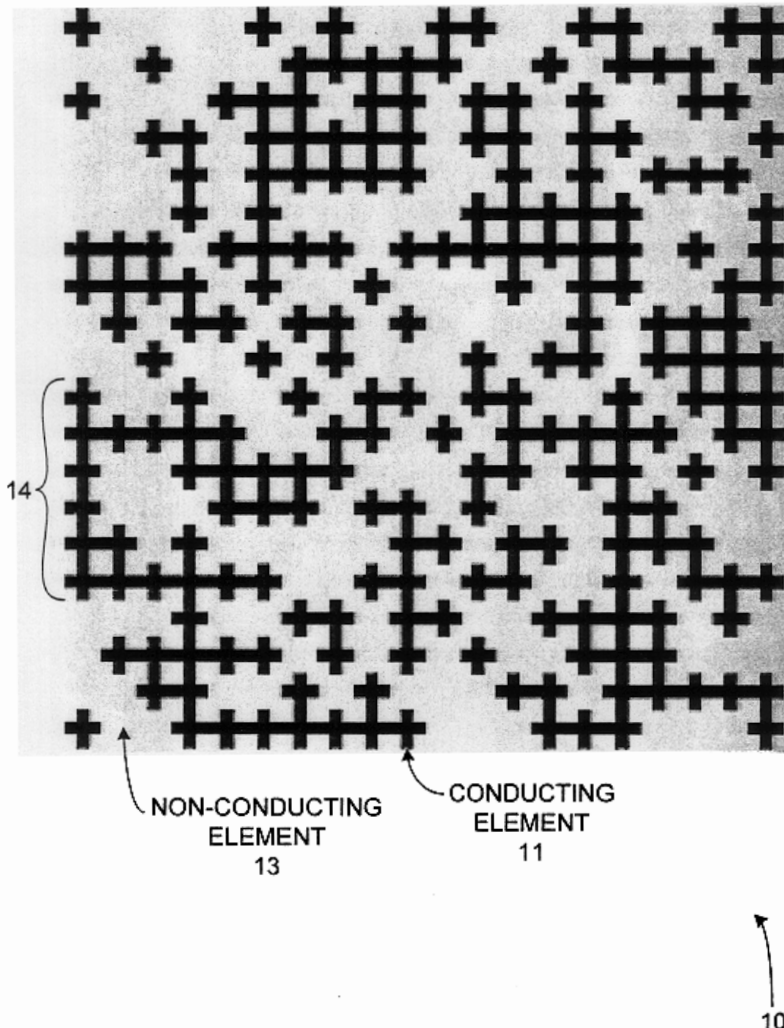


FIG. 1

Figure 2.1: The fragmented aperture concept: a planar surface divided into a grid of sub-wavelength pixels, each either conducting (black) or non-conducting (white). The pattern of conducting and non-conducting elements defines the antenna geometry [1].

GA maintains a population of candidate antenna designs, each represented by a binary string. Over successive generations, the population evolves toward better antenna designs through the standard genetic operations of selection, crossover, and mutation.

2.2.2 Two-Stage Optimization

The original design process employed a two-stage optimization approach, as illustrated in Figure 2.2. In the first stage, the aperture area is described using a relatively small number of trapezoidal conducting strips arranged symmetrically about a coaxial feed point. Each strip has a variable length that is encoded in the binary representation. This coarse description of the antenna geometry allows the GA to quickly explore the design space and identify promising regions.

In the second stage, the best design from the first stage is converted to the full pixel representation and the GA continues to optimize at the pixel level, refining the antenna geometry to improve performance. The flowchart for this second stage is shown in Figure 2.3.

2.2.3 Fitness Evaluation with FDTD

At each generation of the GA, every candidate antenna in the population must be evaluated to determine how well it meets the design objectives. This evaluation requires a full-wave electromagnetic simulation of each candidate antenna. The finite-difference time-domain (FDTD) method was used exclusively for this purpose because a single time-domain simulation produces the antenna response across the entire frequency band of interest via Fourier transformation (see Appendix A for details).

The fitness function used to evaluate each candidate antenna was typically based on the broadside realized gain across the design bandwidth. Designs that achieved good impedance match (low VSWR) and high broadside gain over the specified frequency range received higher fitness scores. The GA then preferentially selected high-fitness individuals for reproduction, driving the population toward better antenna designs over successive generations.

Even with the efficiency of the FDTD method, the computational cost of evaluating hundreds or thousands of candidate antennas over many GA generations was substantial. This was one of the earliest applications of large-scale parallel computing to antenna design, with populations of antennas evaluated simultaneously on clusters of workstations.

2.2.4 Symmetry Constraints

To reduce the size of the design space and to ensure that the resulting antenna designs had desirable radiation characteristics, symmetry constraints were typically imposed during the optimization. For a vertically polarized broadside antenna, left-right and top-bottom symmetry were enforced, reducing the number of independent pixels (and hence the length of the binary string) by a factor of four. For example, an aperture with 400 pixels and both symmetries enforced has only 100 independent degrees of freedom, corresponding to a design space of 2^{100} possible configurations—still enormous, but

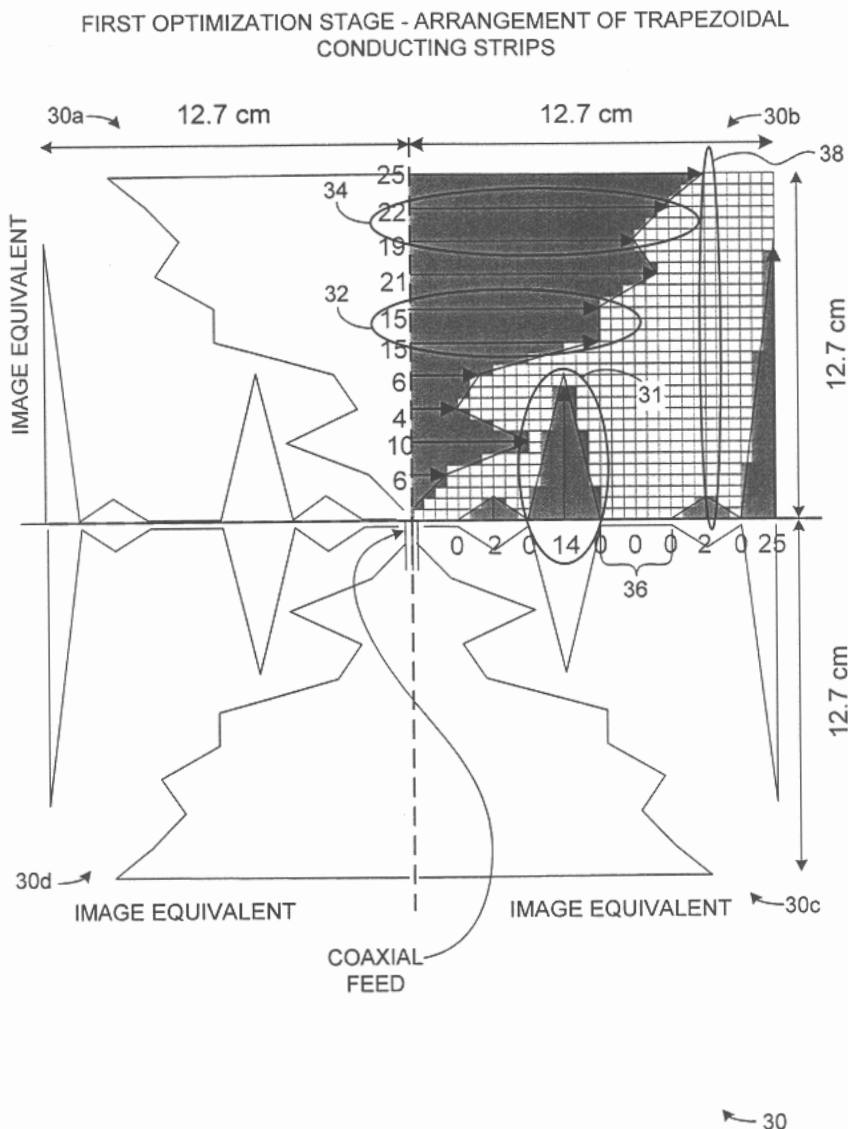


FIG. 4

Figure 2.2: First optimization stage: the aperture is described using trapezoidal conducting strips of variable length arranged about a coaxial feed. This coarse parameterization enables rapid exploration of the design space [1].

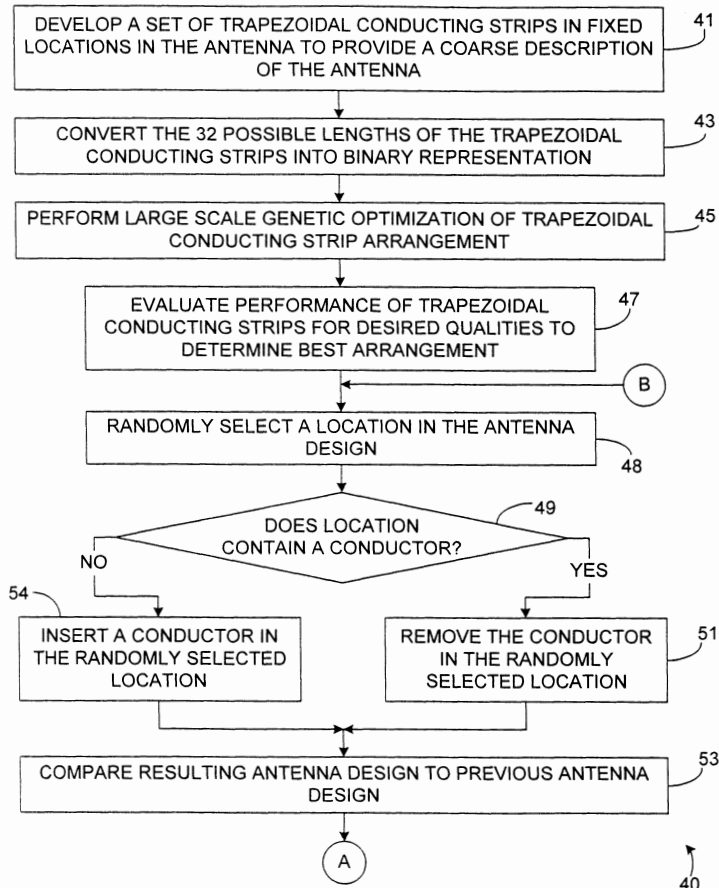
**FIG. 5**

Figure 2.3: Flowchart of the genetic optimization process for fragmented aperture design. The algorithm iteratively toggles pixels between conducting and non-conducting states, evaluating the antenna performance at each step using full-wave electromagnetic simulation [1].

significantly more tractable for the GA.

2.3 First Success

The first successful fragmented aperture antenna design was a planar aperture optimized to operate from 800 MHz to 2.5 GHz (a bandwidth of approximately 3:1). The aperture was 10 inches \times 10 inches (25.4 cm \times 25.4 cm) and was excited at a feed point near the center of the aperture. The optimized design is shown in Figure 2.4.

The visual complexity of the design in Figure 2.4 is striking. The conducting regions form an intricate pattern of connected and disconnected fragments that bears no resemblance to any traditional antenna geometry. It was this visual character—the many fragments of conductor scattered across the aperture—that led to the name “Fragmented Aperture Antenna.”

Despite the non-intuitive appearance of the design, the measured performance was excellent. Figure 2.5 compares the measured broadside gain with the FDTD prediction and with two reference curves: the uniform aperture gain limit ($2\pi A/\lambda^2$, since there is no ground plane) and the gain of a spiral antenna of the same aperture size.

Several important observations can be drawn from Figure 2.5:

- Within the optimization range of 800 MHz to 2.5 GHz, the fragmented aperture closely approaches the uniform aperture gain limit. This demonstrates that the GA/FDTD design process is effective at utilizing the full aperture area.
- The measured and FDTD-predicted gains are in excellent agreement across the entire frequency range, validating the accuracy of the FDTD model used in the design process.
- The fragmented aperture significantly outperforms a spiral antenna of the same physical aperture size. The spiral, being a traveling-wave antenna with a frequency-dependent active region, does not utilize the full aperture at any given frequency.
- Outside the optimization range, the antenna performance degrades, as expected. The GA optimized the design specifically for the 800 MHz to 2.5 GHz band, and performance outside this band was not part of the fitness function.

2.4 Bidirectional Radiation

Because the first fragmented aperture antennas were single-layer planar structures with no ground plane, they radiated into both hemispheres. Figure 2.6 shows the H-plane radiation pattern of the first successful design, comparing the FDTD prediction with the measured pattern.

The bidirectional radiation pattern is clearly visible in Figure 2.6, with the antenna producing roughly equal radiation in the forward and backward directions. The model-measurement agreement is again excellent. This bidirectional behavior is a natural consequence of the single-layer planar geometry: since the antenna structure is symmetric about the plane of the aperture (to within the thickness of the conductor), there is no physical mechanism to preferentially direct radiation into one hemisphere.

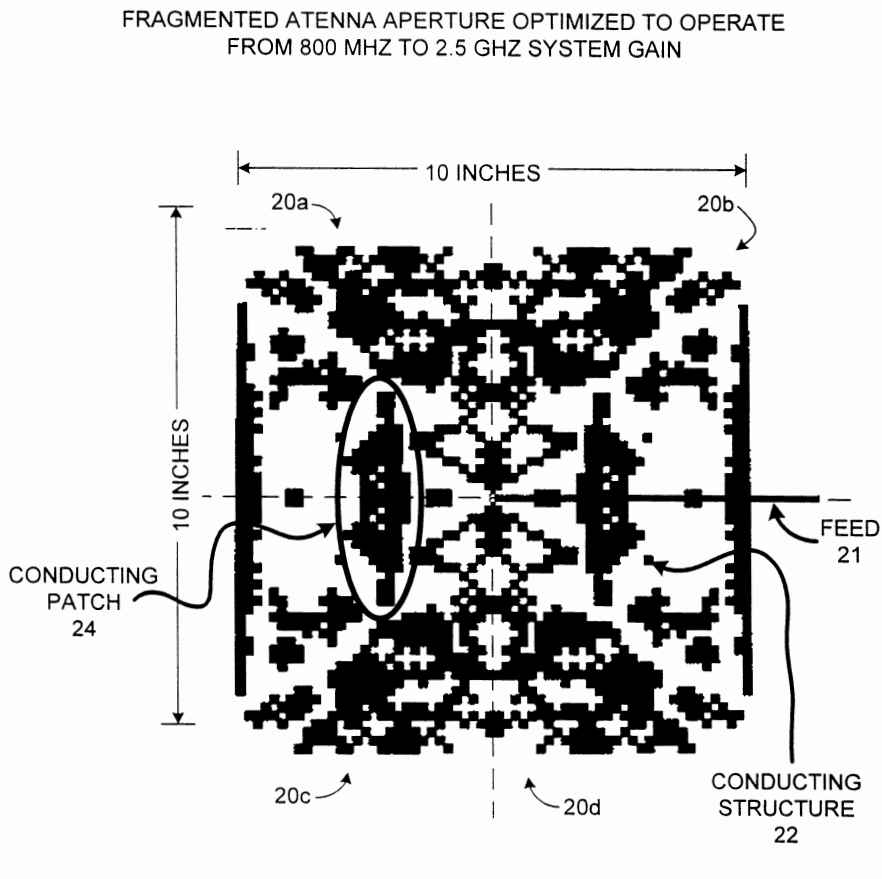
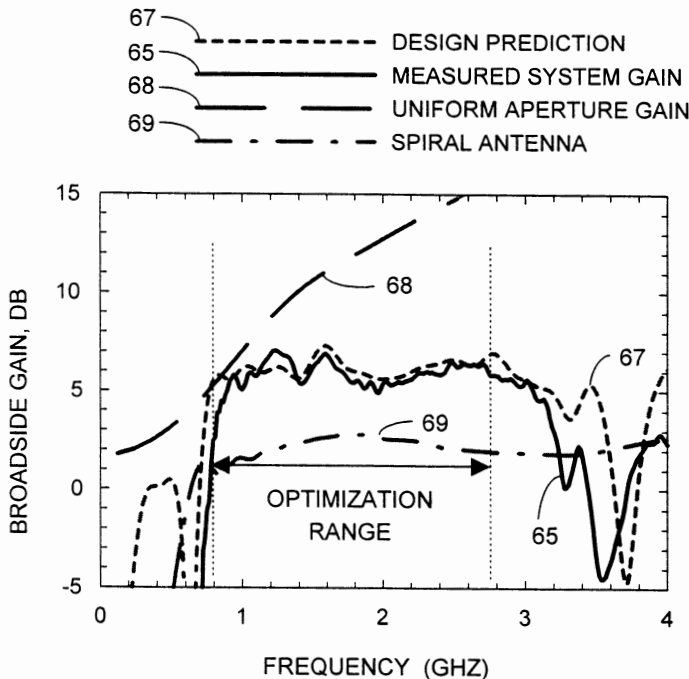
**FIG. 3**

Figure 2.4: The first successful fragmented aperture antenna: a 10-inch \times 10-inch aperture optimized for 800 MHz to 2.5 GHz. The complex pattern of conducting (black) and non-conducting (white) regions was determined entirely by the genetic algorithm and FDTD simulation. The feed is located at the right side of the aperture. Left-right and top-bottom symmetry lines are indicated by the dashed lines [1].

MEASURED AND PREDICTED PERFORMANCE FOR ANTENNA 20



64

FIG. 7

Figure 2.5: Measured and predicted broadside gain for the first fragmented aperture antenna (Figure 2.4). The fragmented design closely approaches the uniform aperture gain limit across the 800 MHz to 2.5 GHz optimization range, and significantly outperforms a spiral antenna of the same aperture size. The measured and FDTD-predicted gains are in excellent agreement [1].

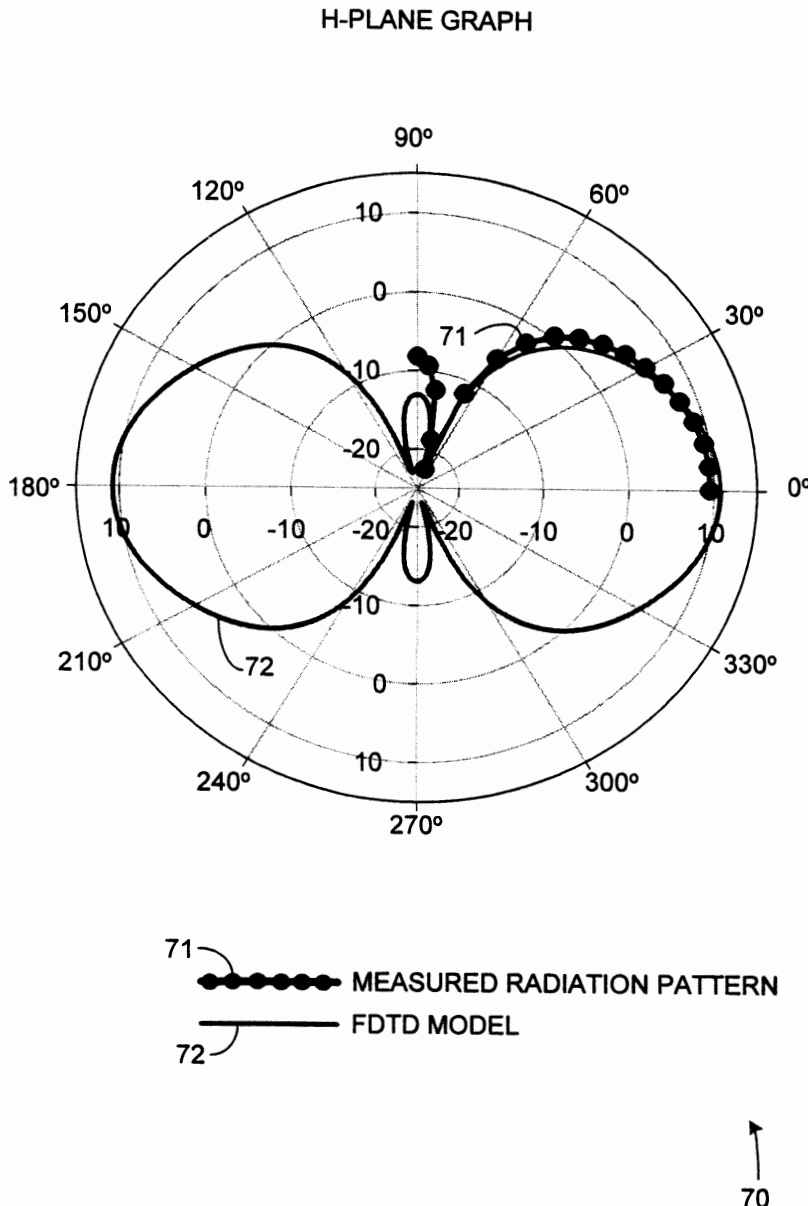
**FIG. 8**

Figure 2.6: H-plane radiation pattern of the first fragmented aperture antenna, comparing the measured pattern with the FDTD model prediction. The pattern is clearly bidirectional, with roughly equal radiation into the forward and backward hemispheres [1].

For many applications, bidirectional radiation is undesirable—half of the radiated power is directed away from the intended coverage area. This motivates the use of a ground plane behind the aperture. However, as will be discussed in detail in Chapter 7, a simple conducting ground plane introduces half-wave nulls at frequencies where the aperture-to-ground-plane spacing is an integer multiple of $\lambda/2$. Addressing this challenge led to the development of broadband screen backplanes and multi-layer radiating structures that are key features of the wideband fragmented array designs.

2.5 Fragmented Broadband Ground Planes

An interesting early application of the fragmented aperture concept was the design of broadband ground planes. Just as the pixel pattern on the radiating aperture can be optimized to achieve desired antenna characteristics, the pixel pattern on a surface behind the aperture can be optimized to function as a broadband ground plane.

A conventional conducting ground plane placed a quarter wavelength behind a radiating aperture provides constructive interference at the design frequency: the backward-radiated wave reflects off the ground plane and, after traveling an additional half wavelength (round trip), arrives back at the aperture in phase with the forward-radiated wave. However, this constructive interference is inherently narrowband.

By replacing the solid conducting ground plane with a fragmented surface—a pixelated pattern of conducting and non-conducting regions—it is possible to design a reflector that provides a more uniform phase response over a wider bandwidth. Figure 2.7 shows the transmission phase through a fragmented surface compared with a reference.

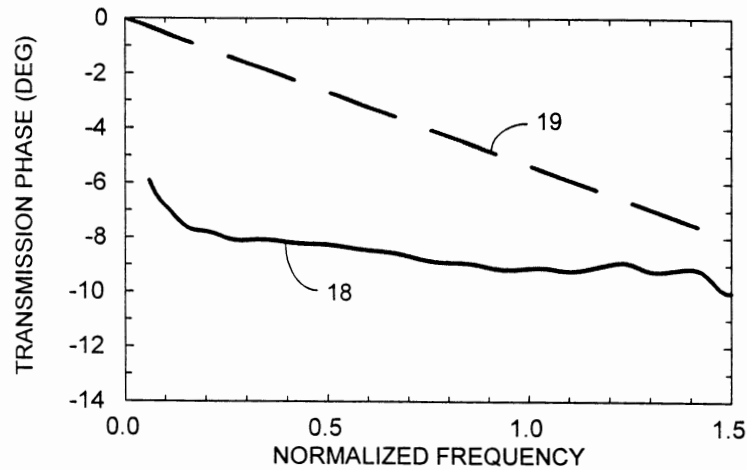
This early exploration of fragmented ground planes laid the groundwork for the more sophisticated broadband screen backplane designs described in Chapter 7, which use resistive card (r-card) layers in combination with a conducting ground plane to achieve wideband operation.

2.6 The Original Patent and Early Publications

The original fragmented aperture antenna concept, including both the radiating aperture and the broadband ground plane, was disclosed in U.S. Patent 6,323,809, “Fragmented Aperture Antennas and Broadband Ground Planes,” granted November 27, 2001 [1]. The inventors were J. G. Maloney, M. P. Kesler, P. H. Harms, and G. S. Smith.

The first public presentation of the fragmented aperture concept occurred at the ICAP/JINA Conference on Antennas and Propagation in 2000 [2]. The reconfigurable version of the concept (switched fragmented apertures) was presented at the IEEE Antennas and Propagation Symposium later that same year [3]. The concept was subsequently described in a number of conference papers and symposium presentations [4], and was included as part of a chapter on wideband arrays in the Modern Antenna Handbook [5].

Since the original publications, several other research groups have independently adopted the fragmented aperture design approach for their own applications. Herscovici et al. applied the concept to aperture-coupled microstrip antennas [6]. Thors et al. used



16

FIG. 2

Figure 2.7: Transmission phase comparison demonstrating the broadband properties of a fragmented surface [1].

fragmented apertures for broadband phased array element design [7]. Ellgardt and Persson investigated wide-angle scanning fragmented aperture arrays [8]. These and other efforts confirm the broad applicability of the fragmented aperture design philosophy.

2.7 Lessons Learned

The success of the original fragmented aperture antenna validated the fundamental premise that computational optimization could discover antenna geometries far beyond those accessible through traditional design approaches. However, the early work also revealed important limitations that would drive subsequent research:

- **Diagonal touching.** The original rectangular pixel geometry led to situations where conducting pixels touched only at their corners. In the FDTD simulation, these diagonally touching pixels are always electrically connected, but when fabricated (e.g., by printed circuit board etching), the connection is unreliable. This issue, and the solutions to it, are the subject of Chapter 3.
- **Convergence for large pixel counts.** As the number of pixels increased beyond approximately 100, the standard GA mutation operator became increasingly ineffective at exploring the design space. An improved mutation strategy tailored for fragmented apertures is described in Chapter 3.
- **Bidirectional radiation.** Single-layer fragmented apertures without a ground plane radiate equally into both hemispheres, limiting the achievable gain to $2\pi A/\lambda^2$. Addressing this limitation motivated the development of broadband backplanes (Chapter 7) and multi-layer radiating structures (Chapter 7).
- **Fixed designs.** Once fabricated, a fragmented aperture antenna operates with a single set of characteristics. The desire for antennas that could dynamically change their operating characteristics led to the development of reconfigurable fragmented apertures (Chapter 5).

Despite these limitations, the original fragmented aperture concept established a powerful new paradigm for antenna design: one in which the physical structure of the antenna is determined by computation rather than by analytical insight alone. The remaining chapters of this book describe how this paradigm has been extended and refined to address an increasingly wide range of antenna design challenges.

References

- [1] J.G. Maloney, M.P. Kesler, P.H. Harms, and G.S. Smith, Fragmented Aperture Antennas and Broadband Ground Planes, U.S. Patent, No. 6,323,809 B1, November 27, 2001.
- [2] J. G. Maloney, M. P. Kesler, P. H. Harms, T. L. Fountain and G. S. Smith, “The fragmented aperture antenna: FDTD analysis and measurement”, Proc. ICAP/JINA Conf. Antennas and Propagation, 2000, pg. 93.

- [3] J. G. Maloney, M. P. Kesler, L. M. Lust, L. N. Pringle, T. L. Fountain, and P. H. Harms, “Switched Fragmented Aperture Antennas”, in Proc. 2000 IEEE Antennas and Propagation Symposium, Salt Lake City, 2000, pp. 310-313.
- [4] P. Friederich, L. Pringle, L. Fountain, P. Harms, D. Denison, E. Kuster, S. Blalock, G. Smith, J. Maloney and M. Kesler, “A new class of broadband planar apertures,” Proc. 2001 Antenna Applications Symp, Sep 19, 2001, pp. 561-587.
- [5] W. Croswell, T. Durham, M. Jones, D. Schaubert, P. G. Friederich and J. G. Maloney, “Wideband Arrays,” Chapter 12, Modern Antenna Handbook, Balanis, 2011.
- [6] N. Herscovici, J. Ginn, T. Donisi, B. Tomasic, “A fragmented aperture-coupled microstrip antenna,” Proc. 2008 Antennas and Propagation Symp, July 2008, pp. 1-4.
- [7] B. Thors, H. Steyskal, H. Holter, “Broad-band fragmented aperture phased array element design using genetic algorithms,” IEEE Trans. Antennas Propagation, Vol. 53.10, 2005, pp. 3280-3287.
- [8] A. Ellgårdt, P. Persson, “Characteristics of a broad-band wide-scan fragmented aperture phased array antenna”, EuCAP 2006, Nov 2006, pp. 1-5.

Chapter 3

Improved Approach to Design Fragmented Apertures

3.1 Overview

In the late 1990's, Maloney et al. began investigating the design of highly pixelated apertures whose physical shape and size are optimized using genetic algorithms (GA) and full-wave computational electromagnetic simulation tools (i.e. FDTD) to best meet the required antenna performance specification; i.e. gain, bandwidth, polarization, pattern, etc. [1]-[4]. Visual inspection of the optimal designs showed that the metallic pixels formed many connected and disconnected fragments. Hence, I coined the term Fragmented Aperture Antennas for this new class of antennas. A detailed description of the original design approach is disclosed in [5]. Since then, other research groups have been successfully designing fragmented aperture antennas for other applications, see [6]-[8] for three examples.

However, the original fragmented design approach suffers from two major deficiencies. First, the placement of pixels on a generalized, rectilinear grid leads to the problem of diagonal touching. That is, pixels that touch diagonally lead to poor measurement/model agreement. Other research groups are also grappling with this diagonal touching issue [9]. Second, the convergence in the GA stage of the design process is poor for high pixel count apertures ($>> 100$).

This chapter will present solutions to both of these shortcomings. First, alternate approaches to the discretization of the aperture area that inherently avoid diagonal touching will be presented. Second, an improvement to the usual GA mutation step that improves convergence for large pixel count fragmented aperture designs will be presented.

3.2 Limitations with Fragmented Apertures

Originally, fragmented aperture antennas were envisioned as a planar surface with a grid of rectangular regions or pixels that were either conducting or non-conducting,

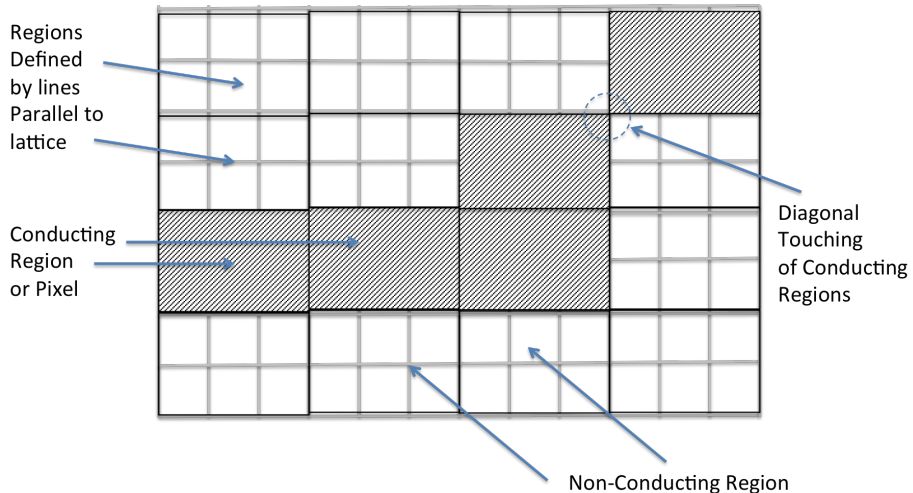


Figure 3.1: Original Fragmented Aperture approach based on lattice of rectangular areas. An example of diagonal touching is shown in the top right of the figure.

as shown in Figure 6.1 . A genetic algorithm and a computational electromagnetic model were used to determine which pixels should be conducting and which should be non-conducting to form an antenna surface suitable for a given use. This concept was generalized to conducting or non-conducting parallelogram pixels as shown in Figure 3.2 in the original fragmented aperture patent [5].

As discussed elsewhere, the approach shown in Figure 6.1 was very successfully used to design novel antennas [1]-[4]. However, many of these designs were troublesome to build and measure. The primary problem is called “diagonal touching” of pixels as illustrated in the top right in Figures 6.1 and reffig:IFAF2 .

Diagonal touching is not a problem during design because in the numerical models the diagonally touching pixels in the antenna are always touching. However, when fabricated using approaches such as printed circuit board etching, the pixels are often disconnected because of over-etching, as illustrated in Figure 3.3(a). Disconnecting metal that should be connected is one of the worst things that can happen within an antenna causing problems with the antenna impedance and gain characteristics.

Other researchers have also observed the trouble with diagonal touching and a nice photograph is shown in Figure 3.3(b) of a etch copper fragmented surface citesomeone

In fact, nearly every antenna design included in the original fragmented aperture patent suffers from this issue of diagonal touching, see Figure 3.4 for a few examples from US Patent 6323809 [5]. It turns out that the fundamental approach of partitioning the area using the approaches in Figures 6.1 or 3.2 was the problem. Specifically, if the fundamental pixels have edges parallel to the lattice forming vectors then the issue of “diagonal touching” will persist.

In the next section, we will discuss four approaches that have been successfully used over the years to mitigate these diagonal touching issues. But, the best approach is to change the area partitioning strategy as presented in Section 3.4.

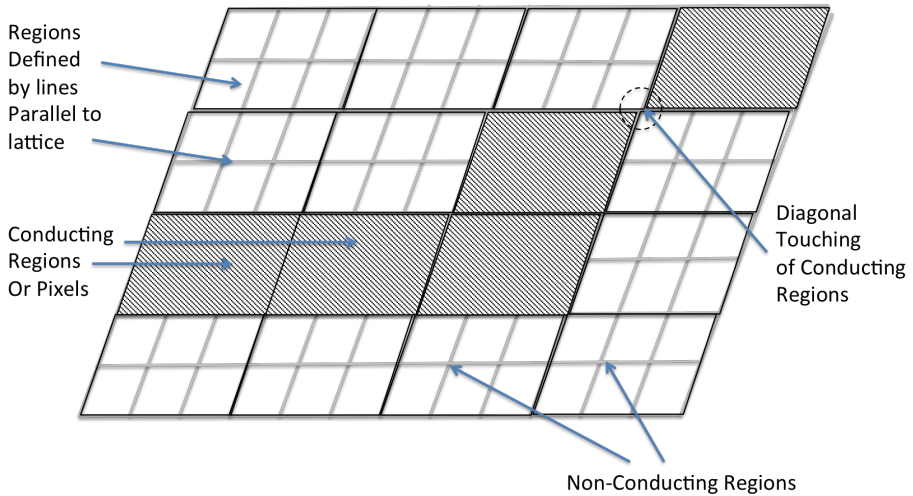


Figure 3.2: Generalized Fragmented Aperture Approach based on parallelograms. Again, an example of diagonal touching is shown in the top right of the figure

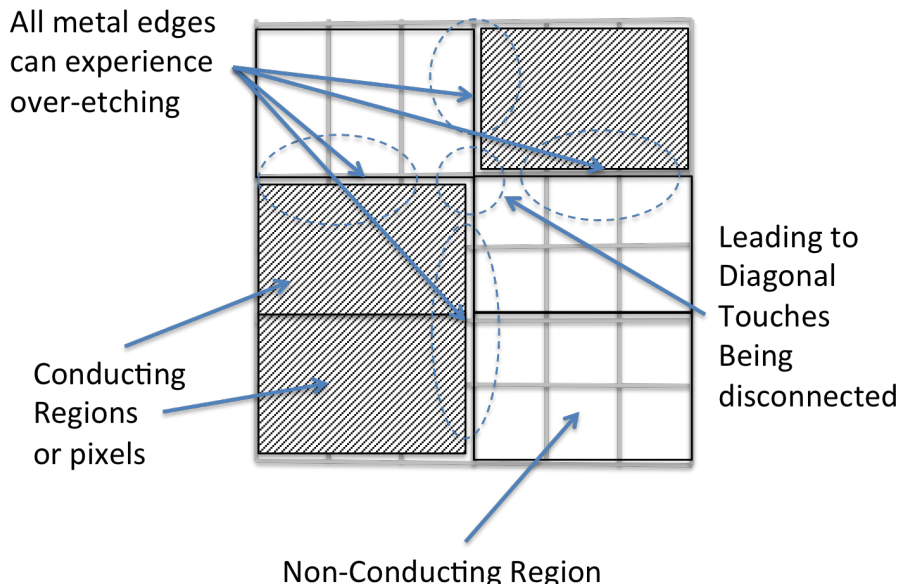


Figure 3.3: (a) Over-etching causing diagonal elements not to touch as shown in top center, (b) close photograph of a etched copper fragmented antenna showing over etch disconnecting diagonal fragments.

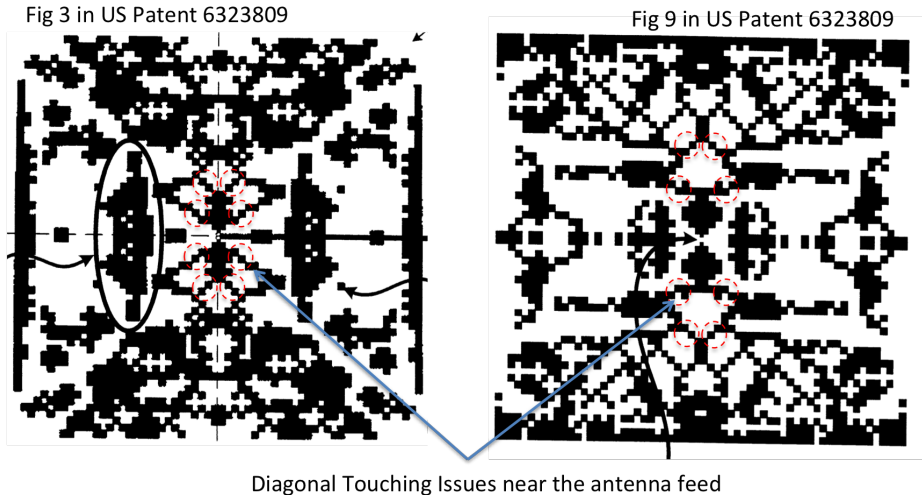


Figure 3.4: Two sample designs from original fragmented patent exhibiting diagonal touching [5]. The most troublesome examples of diagonal-touching near the antenna feed are circled

3.3 Initial Approaches to mitigate diagonal touching

One approach successfully exploited was to consider a super-cell approach as illustrated in Figure 3.5(a). A super-cell is a collection of smaller areas; e.g. the super-cell shown in Figure 3.5 is a 3 by 3 lattice of the smaller pixels. To avoid diagonal touching, we simply define the conducting area as the 5 sub-elements that defined a plus sign. Hence, the absence of conducting material in the corners of the super-cell prevented any potential for diagonal touching. This did successfully allow antennas to be designed and fabricated with a high probability of good correlation between measurement and model.

However, this approach forces electrical currents to flow only in grid conforming directions. This over-constraint could lead to suboptimal antenna designs.

Another successful approach was to intentionally fabricate every pixel roughly 10% larger than designed, as illustrated in Figure 3.5(b). This approach was found to lead to a high percentage of good fabricated antennas. However, this approach leads to the antennas having roughly 10-20% more conductor than originally designed which could lead to less than desired antenna characteristics in the fabricated antennas.

It is worth noting that fabricating the conducting pixels 10% smaller, would guarantee the pixels never diagonally touch, but this would lead to antennas that never have conducting areas larger than one pixel which would almost never be any good. Also, this would be contrary to the numerical models used in design where the elements always touch when diagonally adjacent.

Other research groups are aware of this issue of diagonal touching and have come up with other ways to address it. In [8], the slightly larger pixel strategy shown in Figure 3.5(b) and a variant of placing a small square of metal at the diagonal touching

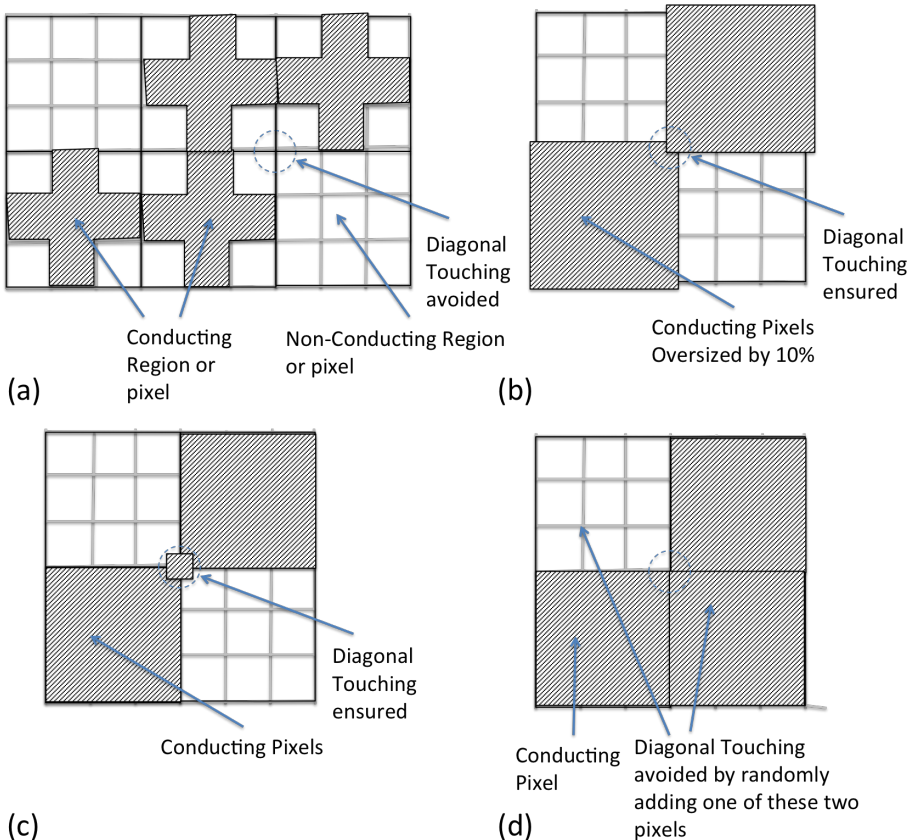


Figure 3.5: (a) Super-cell approach; e.g. 3x3 plus signs, (b) Ten Percent Larger Fabrication, (c) Small metal square to ensure contact, (d) Random coin flipping approach

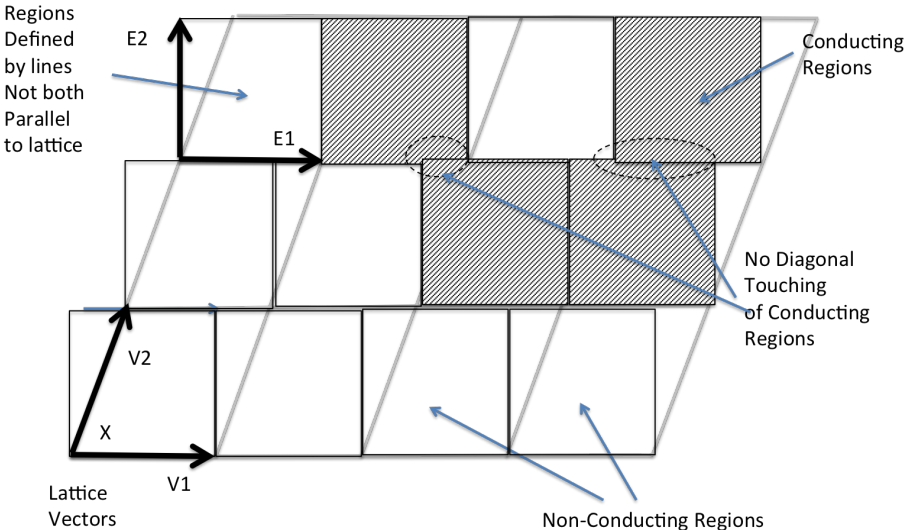


Figure 3.6: First Approach to Improved Fragmented Aperture Antennas.

location shown in Figure 3.5(c) were considered. Prof Rahmat-Samii of UCLA in presentations has discussed how they have used a random coin flipping process to decide which of the two non-conducting pixels to make conducting to fix the diagonal touch as illustrated in Figure 3.5(d).

3.4 Three Improved Fragmented Aperture Antenna Embodiments

The proper approach to avoiding diagonal touching is to break the dependence of element edges and lattice directions implicit in Figures 6.1 and 3.2. The next three subsections discuss three new approaches for breaking this dependence which lead to improved fragmented aperture antennas.

3.4.1 First Approach

In the first approach to improve fragmented apertures, one should define the individual conducting/non-conducting elements using a second set of directions that are not both parallel to the lattice constants as illustrated in Figure 3.6. The example shown in Figure 3.6 consists of square elements on a $X \approx 63.4356^\circ$ skewed lattice.

Notice that skewing the lattice vector, \vec{V}_2 , has removed the diagonal touching possibility.

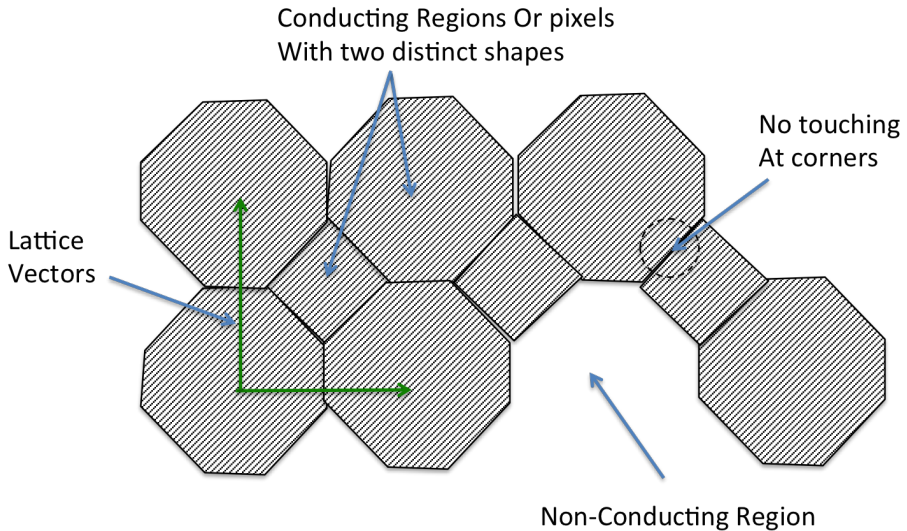


Figure 3.7: Second Approach to Improved Fragmented Aperture Antennas.

3.4.2 Second Approach

In the second approach to improved fragmented apertures, one should alternate the shape of fundamental conducting / non-conducting pixels such that the elements diagonally touch in a definite manner as illustrated in Figure 3.7.

Essentially, the two shapes need to be chosen such that together the pair tessellate the plane.

3.4.3 Third Approach

In the third approach to improved fragmented aperture, one should chose the shape of the fundamental conducting / non-conducting pixels such that the single shape tesselates the plane and does not touch diagonally. Figure 3.8 shows one example of such an element but many others shapes will also work.

3.5 Improved Mutation Algorithm to Improve Convergence Rate of Fragmented Apertures

Traditionally, fragmented aperture antennas are designed using evolutionary algorithms like the genetic algorithm [5]. One important step in the genetic algorithm is called mutation. In a standard genetic algorithm, mutation is a random process where a small number of genes are changed each generation to help avoid convergence to a suboptimal solution. For a fragmented antenna, mutation makes a few pixels randomly conducting or not in the next population of antennas. Many of these mutations will create only an

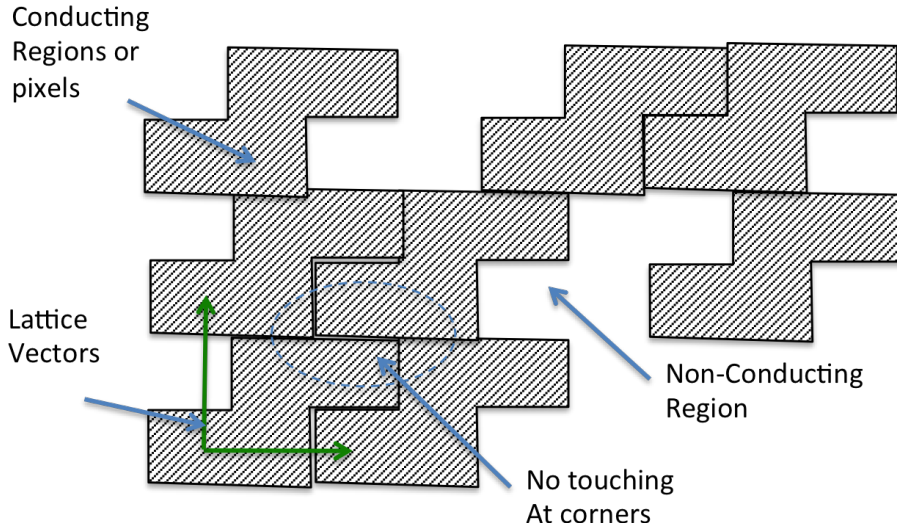


Figure 3.8: Third Approach to Improved Fragmented Aperture Antennas.

isolated metal pixel or small hole in metal that will have a very negligible effect on the antenna performance.

As will be shown below, we have found that introducing a modified mutation algorithm tailored for fragmented aperture antennas helps speed up the convergence of the design process when the number of elements/pixels is high.

The goal of the new mutation process is to bias mutation to either increase the size of conducting fragments in empty regions or increase the size of holes in large metal regions. This new mutation process uses an adjacency matrix that describes which elements/pixels are touching each other.

To demonstrate the efficacy of this adjacency-based mutation strategy, three consecutive design trials were conducted with the traditional mutation algorithm and with the new mutation algorithm. Figure 3.9 shows the convergence of the fitness as a function of generation count. The fitness of any generation is the fitness of the best individual. The y-axis shows the average best individual across three trials. The new mutation algorithm (green line) converges to a better score in less generations.

In fact, as shown in the Table 3.1, the three trials with the new mutation algorithm were each better than the corresponding trial with the traditional mutation algorithm.

The values in the table in Table 3.1 also illustrate that when one is using an evolutionary algorithm; such as, the genetic algorithm, to design an antenna or any electromagnetic device, more than one design trial should always be executed because as we have experienced and is illustrated in this table, the subsequent designs can be more than a dB better than the first.

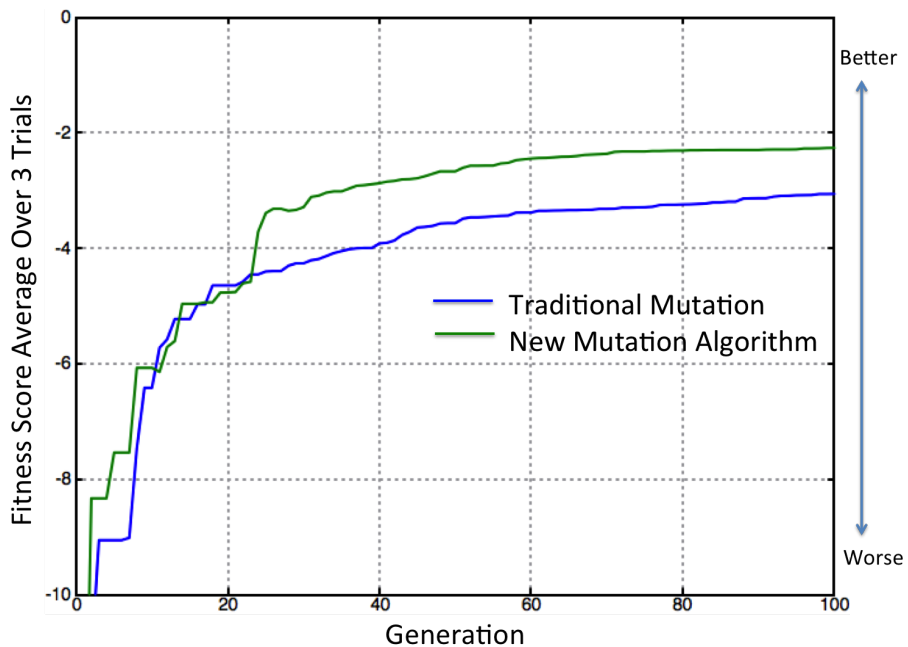


Figure 3.9: Third Approach to Improved Fragmented Aperture Antennas.

Table 3.1: Comparison across the three convergence trials (Higher number is better)

Fitness Score Comparison	Traditional Mutation Algorithm	New Mutation Algorithm
Best of 3 Trials	-2.238	-1.684
Middle	-3.208	-2.461
Worst	-3.727	-2.850

3.6 Sample Planar Improved Fragmented Aperture Designs

3.6.1 First Approach

The approach illustrated in Figure 3.6 was used to design a series of fragmented aperture antennas that spanned from 500 MHz to 2.0 GHz. The lattice skew angle, X, was chosen to be $\tan^{-1}(2) \approx 63.435^\circ$ to give the desired left/right physical symmetry. The square pixels were 10.8 mm on a side and the total aperture area was 25.4 cm x 25.4 cm. Four representative aperture designs are shown in Figure 3.10. Each of the four sample antenna designs are excited at the terminal pair in the center with a 100 ohm transmission line.

The physical shapes of the designed antennas are shown in Figure 3.10. As the drawings show, none of the antennas suffer from diagonal touching issues.

The aperture designs (i.e. placement of conductor and non-conductor) were performed using a genetic algorithm. For these designs, the 25.4 cm x 25.4 cm area consisted of 663 individual pixels. Enforcing left/right and top/down symmetry, the degrees of freedom drops to 169. Hence assigning a single bit to represent the state of each area (1=conducting, 0=non-conducting) yields a 169 bit genetic code. Using a genetic population size of 32 antennas, 100 Genetic Algorithm generations was typically required to realize one of these sample designs. The genetic algorithm used a finite-difference time-domain (FDTD) numerical model of each antenna to compute return loss and radiation properties for the evolving population of antennas (see Appendix A for more information on modeling antennas with FDTD).

The genetic algorithm fitness function rewarded good match (return loss better than 15dB), and as large as possible, broadside realized gain.

Figure 3.11 shows the broadside realized gain of each antenna, while Figure 3.12 shows the return loss of each antenna. The gains are compared with an aperture gain limit (black line). Since these apertures have no ground plane, the aperture gain limit for high frequencies is $2\pi \text{Area}/\lambda^2$.

The VSWR of the four sample designs are below 1.5 across the respective design bands which is consistent with the design intent of return loss better than 15 dB.

3.6.2 Second Approach

The second approach illustrated in Figure 3.7 is also useful for designing antennas. The second approach also supports left/right and top/down symmetry when appropriate.

Now have four 4 designs, redo these 3 Figures and update text

The aperture area was again 25.4 cm x 25.4 cm and was excited in the center with a 100 ohm feed.

The aperture consisted of 841 shaped pixels. When left/right and top/down symmetry was enforced, the number of degrees of freedom dropped to 221.

Figure 3.13 shows two sample designed apertures for the 0.5-0.8 GHz and the 0.8-1.2 GHz bands.

Notice that no diagonal touching is evident in the physical structures shown in Figure 3.13 as desired.

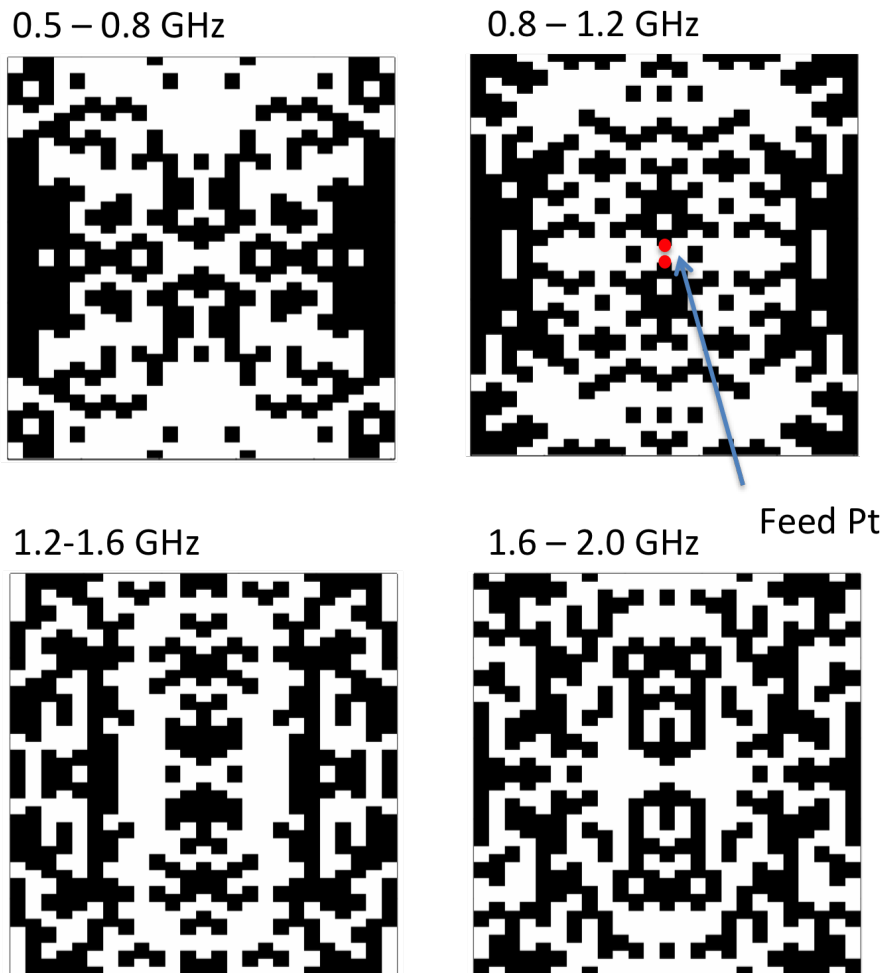


Figure 3.10: Fragmented Aperture shapes of the Improved Fragmented aperture sample designs.

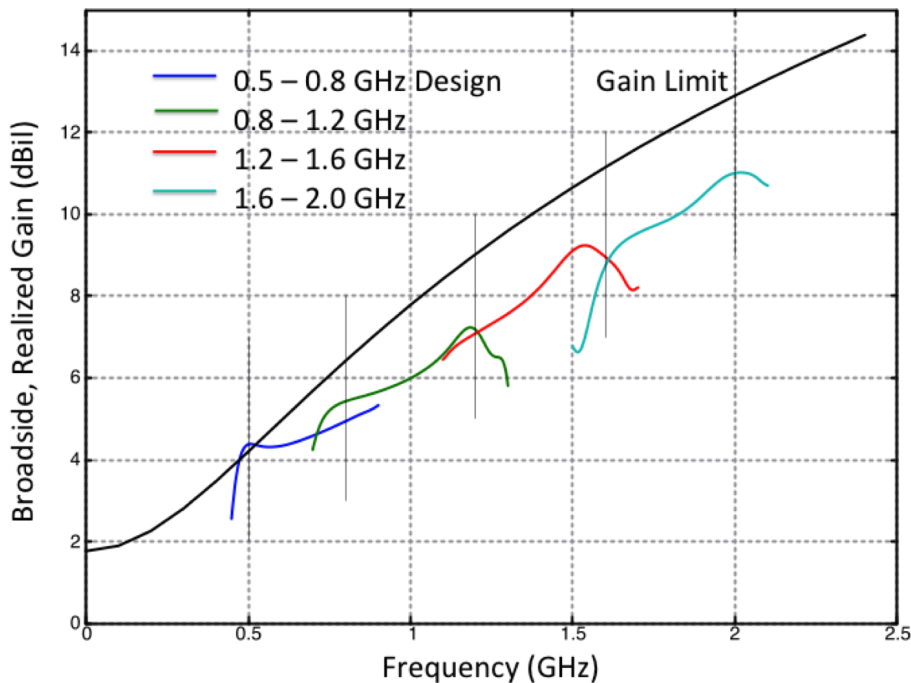


Figure 3.11: Gain summary of First Approach Sample Designs shown in Figure 3.10.

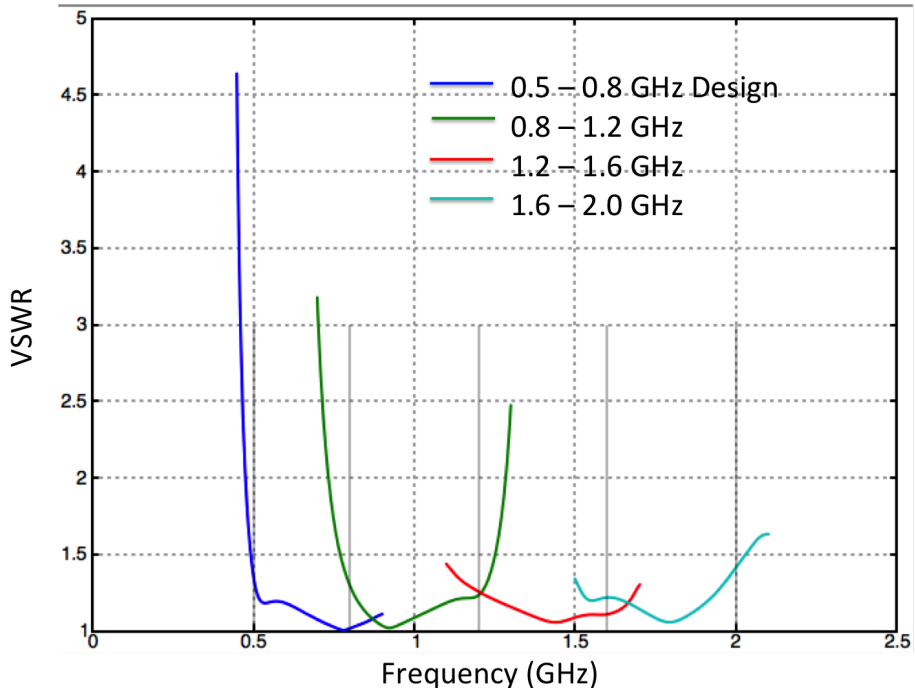


Figure 3.12: VSWR summary of First Approach Sample Designs shown in Figure 3.10.

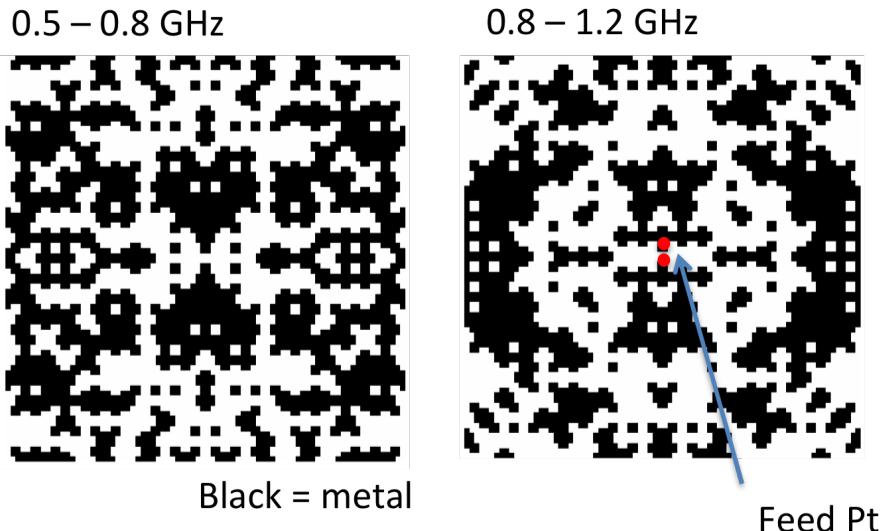


Figure 3.13: Two sample designs from the second approach

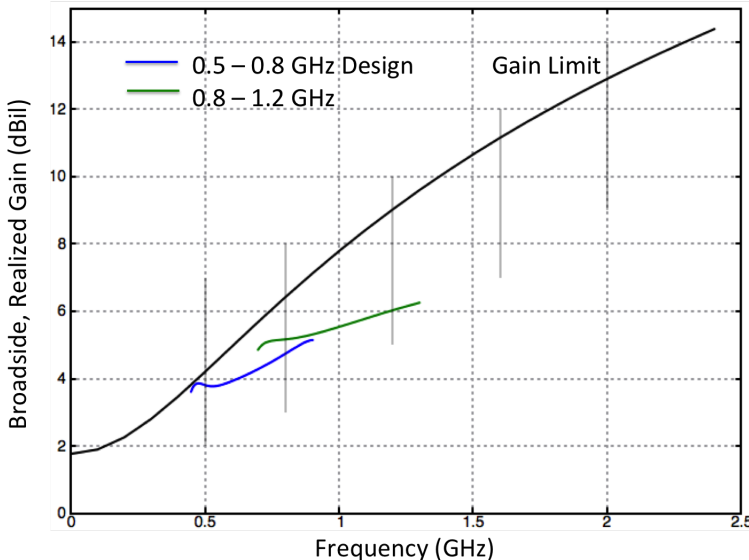


Figure 3.14: Gain summary of second approach sample designs shown in Figure 3.13

Figures 3.14 and 3.15 summarize the broadside gain and VSWR versus frequency of the two sample designs. In general, the performance is quite good.

3.6.3 Third Approach

The third approach illustrated in Figure 3.8 is also useful for designing antennas. However, for the design of vertically or Horizontal polarized elements with a broadside beam, the lack of left/right and top/down symmetry in the third approach is a drawback. For cases where the desired beam direction is not broadside or the desired polarization is different, then the pixelated aperture should not have symmetry and the third approach is comparable to the second or first.

Example Designs needed: -Vpol, Hpol, 45 deg -Vpol beamstear 45 degrees in Az

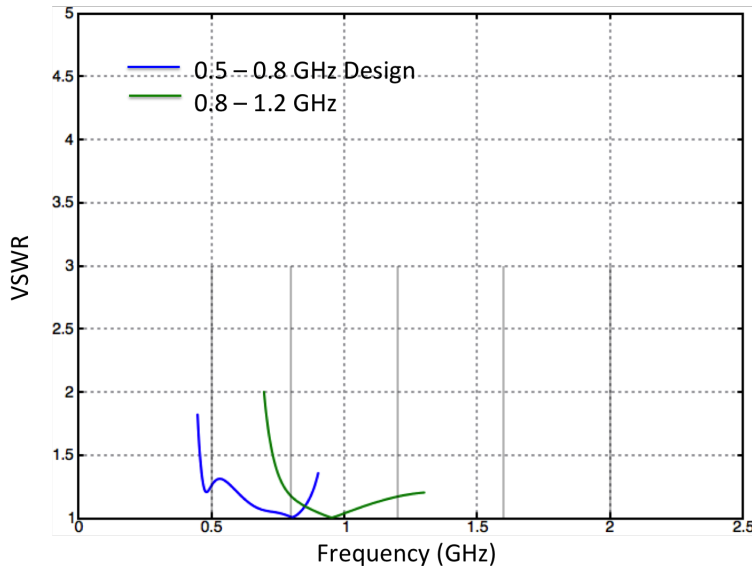


Figure 3.15: VSWR summary of second approach sample designs shown in Figure 3.13

Figure 3.16: Four sample designs from the third approach: (a) Broadside Vpol, (b) Broadside Hpol, (c) Broadside slant linear polarization, (d) Vpol Beam Steered 45° from broadside

Figure 3.17: Gain summary of third approach sample designs shown in Figure 3.13

Figure 3.18: VSWR summary of third approach sample designs shown in Figure 3.13

Figure 3.19: Azimuth Gain Pattern summary at midband of third approach sample designs shown in Figure 3.13

References

- [1] J. G. Maloney, M. P. Kesler, P. H. Harms, T. L. Fountain and G. S. Smith, “The fragmented aperture antenna: FDTD analysis and measurement”, Proc. ICAP/JINA Conf. Antennas and Propagation, 2000, pg. 93.
- [2] J. G. Maloney, M. P. Kesler, L. M. Lust, L. N. Pringle, T. L. Fountain, and P. H. Harms, “Switched Fragmented Aperture Antennas”, in Proc. 2000 IEEE Antennas and Propagation Symposium, Salt Lake City, 2000, pp. 310-313.
- [3] P. Friederich, L. Pringle, L. Fountain, P. Harms, D. Denison, E. Kuster, S. Blalock, G. Smith, J. Maloney and M. Kesler, “A new class of broadband planar apertures,” Proc. 2001 Antenna Applications Symp, Sep 19, 2001, pp. 561-587.
- [4] W. Croswell, T. Durham, M. Jones, D. Schaubert, P. G. Friederich and J. G. Maloney, ”Wideband Arrays,” Chapter 12, Modern Antenna Handbook, Balanis, 2011.
- [5] J.G. Maloney, M.P. Kesler, P.H. Harms, and G.S. Smith, Fragmented Aperture Antennas and Broadband Ground Planes, U.S. Patent, No. 6,323,809 B1, November 27, 2001.
- [6] N. Herscovici, J. Ginn, T. Donisi, B. Tomasic, “A fragmented aperture-coupled microstrip antenna,” Proc. 2008 Antennas and Propagation Symp, July 2008, pp. 1-4.
- [7] B. Thors, H. Steyskal, H. Holter, “Broad-band fragmented aperture phased array element design using genetic algorithms,” IEEE Trans. Antennas Propagation, Vol. 53.10, 2005, pp. 3280-3287.
- [8] A. Ellgårdt, P. Persson, “Characteristics of a broad-band wide-scan fragmented aperture phased array antenna”, EuCAP 2006, Nov 2006, pp. 1-5.
- [9] A. Ellgårdt, “Wide-angle scanning wide-band phased array antennas”, Ph.D. Thesis, KTH School of Electrical Engineering, 2009, pp. 21.

Chapter 4

Sample Antenna Design

4.1 feed strategies

- feed strategies
- in-plane self-balun
- in-Plane twin feed
- unbalanced fed thru ground plane
- balanced fed thru ground plane
- tailor bandwidth
- fixed steering
- broadside
- forward and backward 45
- end fire
- Polarization
 - linear
 - circular
 - non-broadside cp
- tailor beamwidth
- out-band-rejection

4.2 First Success

[2].

Figure A.1 is a schematic drawing showing a typical volume in which Maxwell's equations are to be solved. The volume is divided into unit cells each of volume.

FRAGMENTED ANTENNA APERTURE OPTIMIZED TO OPERATE
FROM 800 MHZ TO 2.5 GHZ SYSTEM GAIN

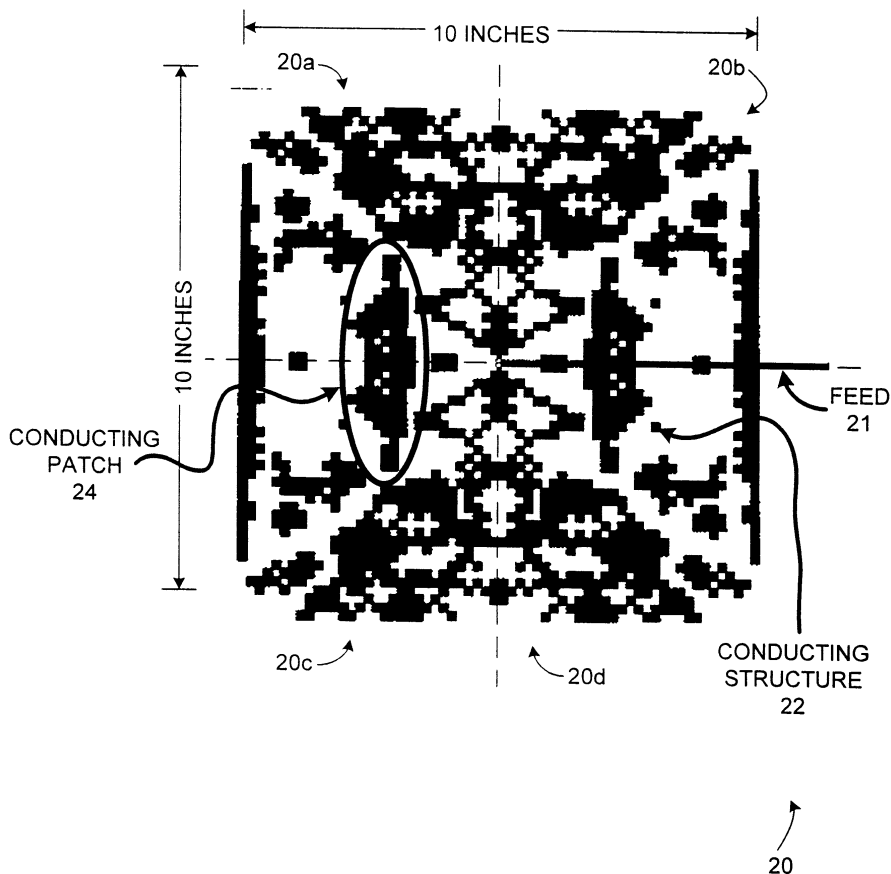


FIG. 3

Figure 4.1: Comparison of fragmented design to uniform aperture limit $2\pi A/\lambda^2$

References

- [1] K. S. Yee, "Numerical Solution of Initial Boundary Value Problems Involving Maxwell's Equations in Isotropic Media," IEEE Trans. Antennas Propagat., Vol. AP-14, pp. 302-307, May 1966.
- [2] J. G. Maloney, G. S. Smith, and W. R. Scott, Jr., "Accurate Computation of the Radiation from Simple Antennas Using the Finite-Difference Time-Domain Method," IEEE Trans. Antennas Propagat., Vol. AP-38, pp. 1059-1068, July 1990.
- [3] J. J. Boonzaaier and C. W. Pistorius, "Thin Wire Dipoles ? A Finite-Difference Time-Domain Approach," Electronics Lett., Vol. 26, pp. 1891-1892, 25 October, 1990.
- [4] D. S. Katz, M. J. Picket-May, A. Taflove, and K. R. Umashankar, "FDTD Analysis of Electromagnetic Wave Radiation from Systems Containing Horn Antennas," IEEE Trans. Antennas Propagat., Vol. AP-39, pp. 1203-1212, August 1991.

Chapter 5

Reconfigurable Fragmented Aperture Antennas

5.1 Introduction

In the preceding chapters, we have shown how the fragmented aperture concept can be used to design antennas that meet particular performance specifications. A planar sheet of conductor is divided into many sub-wavelength pixels, and a genetic algorithm working with an FDTD simulation determines which pixels should be conducting and which should not. Different designs can be obtained to meet different specifications: for example, one design might produce an antenna with a broadside beam optimized for a particular bandwidth, while a second design might produce an antenna with the beam steered to 45° from broadside.

Of course, once a fragmented aperture antenna is fabricated, it can only meet one set of specifications—either the broadside design or the steered design, but not both. It would be enormously useful if a single fragmented aperture could be electronically switched between different configurations to meet different requirements on demand. This would require a mechanism for dynamically changing individual pixels from conducting to non-conducting and vice versa.

One can imagine, for example, making the cladding on a circuit board from a photoconductive material and using a laser to selectively illuminate the pixels that need to be conducting for a particular design. Changing the illumination pattern would reconfigure the antenna. While this particular approach remains impractical with current technology, the underlying idea—a reconfigurable fragmented aperture—motivated the development of the Agile Aperture Antenna described in this chapter.

5.2 The Agile Aperture Antenna Concept

The concept of a reconfigurable fragmented aperture antenna was first published in 2000 under the name “switched fragmented aperture antenna” [2]. Subsequently, DARPA funded a solicitation for “reconfigurable aperture” antennas and coined the acronym

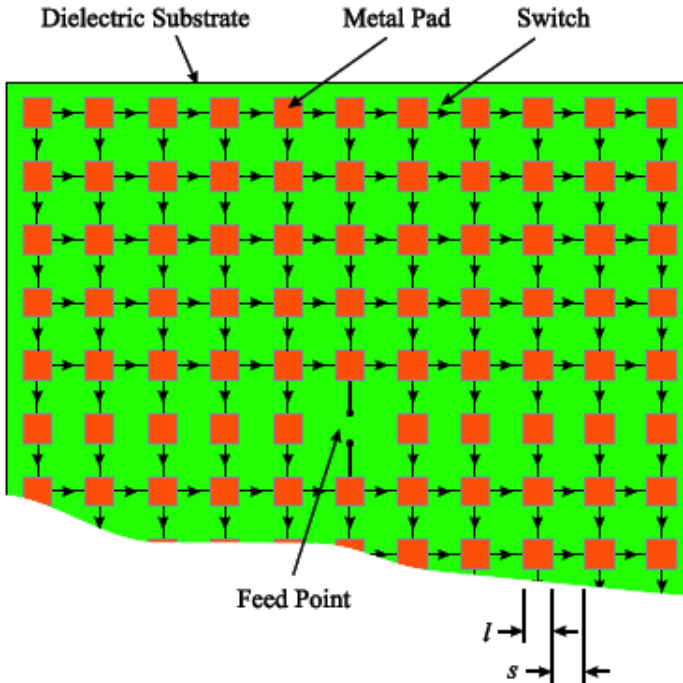


Figure 5.1: Schematic drawing of the Agile Aperture Antenna in dipole form. Square metallic pads are connected by switched links (arrows). The state of each switch (open or closed) determines the antenna configuration [3].

RECAP. To distinguish the fragmented aperture approach from other reconfigurable antenna concepts, we later adopted the term “Agile Aperture Antenna” (A3), emphasizing that the purpose of reconfiguration is to make the antenna *agile*—able to dynamically change its frequency of operation, beam direction, polarization, or other characteristics.

The Agile Aperture Antenna implementation that was successfully demonstrated is shown schematically in Figure 5.1 [3]. A thin dielectric substrate supports an array of square metallic pads. The pads are electrically small, with side length l satisfying $l/\lambda_o \ll 1$, where λ_o is the free-space wavelength at the operating frequency. Each pad is connected to its neighboring pads by switched links, indicated by the arrows in the figure. Each switch may be independently set to open or closed depending on the desired antenna configuration. A single feed point (pair of terminals) is located near the center of the antenna.

The Agile Aperture Antenna can be understood as a variant of the fragmented aperture antenna in which the fundamental unit is not a single pixel but a metallic pad composed of a group of pixels. The pads are not contiguous; they are separated by narrow dielectric gaps. The antenna structure for any given configuration consists of the conducting pads that are connected by closed switches, together with all of the uncon-

nected pads that remain present on the substrate. This is an important distinction from a conventional fragmented aperture: in the Agile Aperture Antenna, the unconnected pads are always physically present and contribute to the electromagnetic behavior of the antenna through scattering, even when they are not part of the connected conducting structure.

5.3 Static Proof of Concept

INSERT: Description of the first two static (hard-wired) pixelated designs that demonstrated the unconnected pads did not prevent good antenna performance. Include figures showing the two designs and their measured performance.

5.4 Reconfigurable Proof of Concept

To prove the validity of the Agile Aperture Antenna concept, a detailed study was conducted using a prototype antenna with hard-wired switches—gaps that were either closed by a soldered wire or left open. This study not only validated the design approach but also identified areas where future research would be needed to extend the concept to practical, electronically reconfigurable antennas.

5.4.1 Prototype Description

For all of the antennas discussed in this section, the aperture was formed from a printed circuit board $22.5 \text{ cm} \times 22 \text{ cm}$ in size, with the pads etched from the copper cladding on one side of the board. The pad side length and spacing were both $l = s = 1.0 \text{ cm}$ (see Figure 5.1). The board contained a total of 120 pads and 208 switches. The dielectric substrate was 1.7 mm thick FR4 circuit board with measured electrical properties $\varepsilon_r = 4.27$ and $\tan \delta = 0.07$ (verify loss tangent value).

The frequency of operation was in the range $0.85 \text{ GHz} \leq f \leq 1.45 \text{ GHz}$, so the pads were electrically small: $0.028 \leq l/\lambda_0 \leq 0.048$. All of the antenna designs described in this section have mirror symmetry about the horizontal line through the feed point, including the states of the switches. This symmetry allows the antennas to be analyzed and measured in either the “dipole form” shown in Figure 5.1 or the “monopole form” shown in Figure 5.2.

5.4.2 Measurement Setup

Figure 5.2 shows the experimental setup used for all of the measurements reported in this section. The monopole version of the Agile Aperture Antenna was mounted vertically on a rotatable disc centered in a large metallic image plane (insert image plane dimensions). The antenna was fed from below the image plane by a 50Ω coaxial line, with the center conductor connected to the bottom pad in the center column of the antenna. A calibrated TEM horn antenna was located at a distance of (insert distance) from the antenna [3]. The scattering parameters for the two-port network formed by the Agile Aperture Antenna and the TEM horn were measured with a network analyzer and

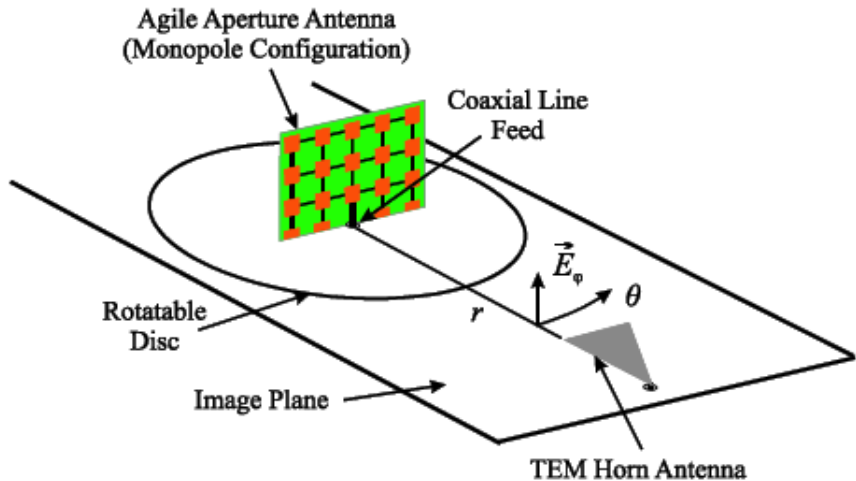


Figure 5.2: Experimental arrangement for measuring the Agile Aperture Antenna in monopole form. The antenna is mounted vertically on a rotatable disc centered in a large metallic image plane [3].

used to determine the absolute gain of the Agile Aperture Antenna [5]. The horizontal radiation pattern ($|E|$ versus azimuth angle ϕ) was obtained by rotating the disc while recording the output signal from the horn.

5.4.3 Design Procedure

The procedure for designing a switch configuration for the Agile Aperture Antenna is conceptually the same as for a conventional fragmented aperture: a rigorous FDTD simulation of the antenna is run in conjunction with a genetic algorithm optimizer (see Appendix A for an introduction to the FDTD method). In all of the FDTD simulations reported here, cubical Yee cells with a side length of 2.5 mm were used.

A performance goal is first established—for example, maximum broadside realized gain over a specified bandwidth. The GA then searches for the switch configuration (which switches should be open and which should be closed) that best meets this goal. Taking into account the mirror symmetry of the antenna, there are $2^{104} \approx 2 \times 10^{31}$ possible switch configurations—far too many to evaluate exhaustively. The GA provides an efficient, though approximate, method for searching this enormous design space.

5.4.4 Broadside Design

The design goal for the first example was to maximize the broadside realized gain over the frequency range $0.85 \text{ GHz} \leq f \leq 1.25 \text{ GHz}$ (a fractional bandwidth of 38%). The

target was that the realized gain should equal or exceed the directivity of a uniform sheet of vertically directed current occupying the same aperture area.

Figure 5.3(a) shows the switch configuration obtained by the GA for this broadband, bidirectional, broadside design. Notice that this configuration has right-left symmetry in addition to the imposed top-bottom symmetry; all of the broadside designs discussed in this chapter are constrained to have this additional symmetry.

Figure 5.4(a) shows the realized gain versus frequency for this design. The dashed blue line is the design goal (uniform aperture directivity), the solid black line is the FDTD simulation, and the red line with markers is the measured result. All realized gain values are for the antenna in the dipole configuration. The simulated and measured realized gains are in good agreement over the design bandwidth, with a maximum difference of approximately 1 dB. The realized gain falls approximately 0.5–1.5 dB below the goal; a portion of this difference is attributable to impedance mismatch at the antenna feed.

Figure 5.4(b) shows the mismatch factor ($1 - |\Gamma_A|^2$) as a function of frequency, where Γ_A is the voltage reflection coefficient at the antenna terminals. Within the design bandwidth, this factor ranges from 0.0 dB to -1.5 dB, confirming that mismatch accounts for a significant portion of the difference between the realized gain and the goal.

Figure 5.5 shows the horizontal radiation pattern at the center frequency $f = 1.05$ GHz. The simulated and measured patterns are nearly identical, with both normalized to a maximum of 0 dB. The heavy line at the center of the pattern indicates the orientation of the dielectric substrate.

5.4.5 End-Fire Design

To demonstrate the versatility of the Agile Aperture Antenna concept, a second design was produced for a completely different objective: a narrowband, unidirectional, end-fire beam over the frequency range $1.0 \text{ GHz} \leq f \leq 1.1 \text{ GHz}$ (a fractional bandwidth of 9.5%). The goal was again that the realized gain should equal or exceed the directivity of a uniform sheet of current, but now with the current phased to produce end-fire radiation.

Figure 5.3(b) shows the switch configuration for this end-fire design. It is immediately apparent that this configuration is strikingly different from the broadside configuration in Figure 5.3(a)—the end-fire design does not have right-left symmetry and produces a fundamentally different current distribution on the aperture. Yet both configurations are realized on the same physical hardware simply by changing which switches are open and which are closed.

Figure 5.6(a) shows the realized gain versus frequency for the end-fire design. The simulated and measured results are again in good agreement over the design bandwidth, with a maximum difference of approximately 1 dB. The realized gain falls approximately 1.0–2.0 dB below the goal. The mismatch factor shown in Figure 5.6(b) is within the range 0.0 dB to -0.8 dB over the design bandwidth.

Figure 5.7 shows the horizontal radiation pattern at $f = 1.05$ GHz. The simulated and measured patterns are in excellent agreement, and both clearly show the characteristic end-fire beam directed to one side of the antenna.

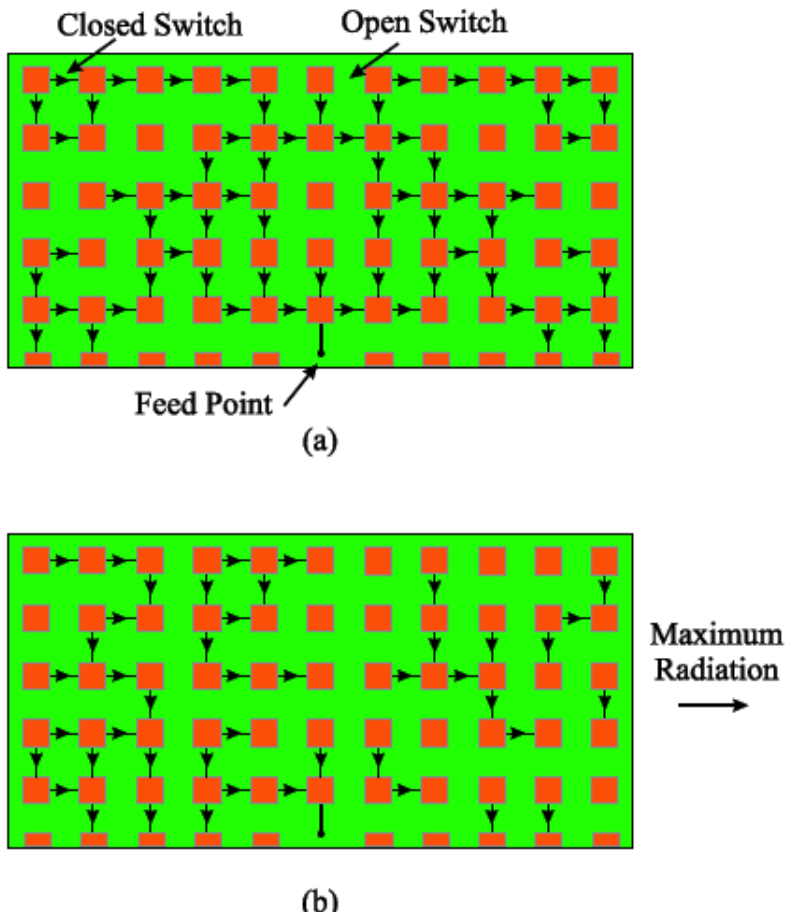


Figure 5.3: Switch configurations for the Agile Aperture Antenna (monopole form) with hard-wired switches. (a) Broadband, bidirectional, broadside design. (b) Narrow-band, unidirectional, end-fire design. The two configurations are strikingly different, yet both are realized on the same physical antenna [3].

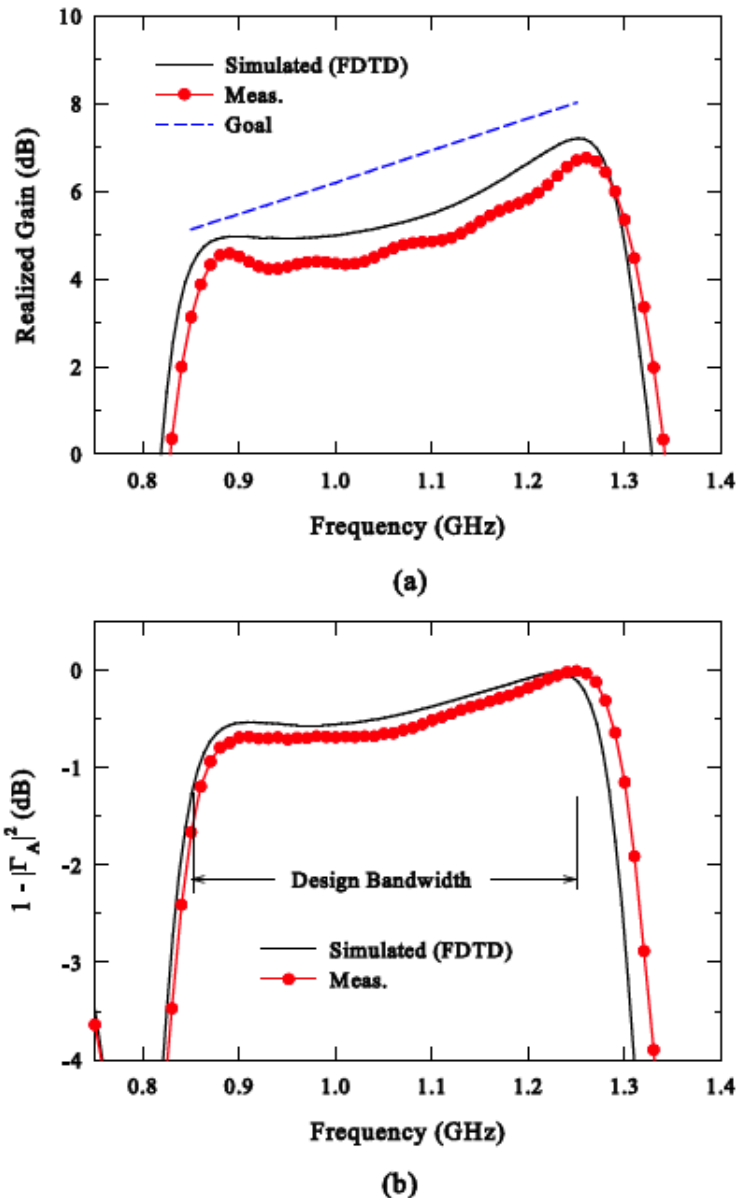


Figure 5.4: Results for the broadband, bidirectional, broadside design with hard-wired switches. (a) Realized gain versus frequency. (b) Gain reduction due to impedance mismatch: $(1 - |\Gamma_A|^2)$ [3].

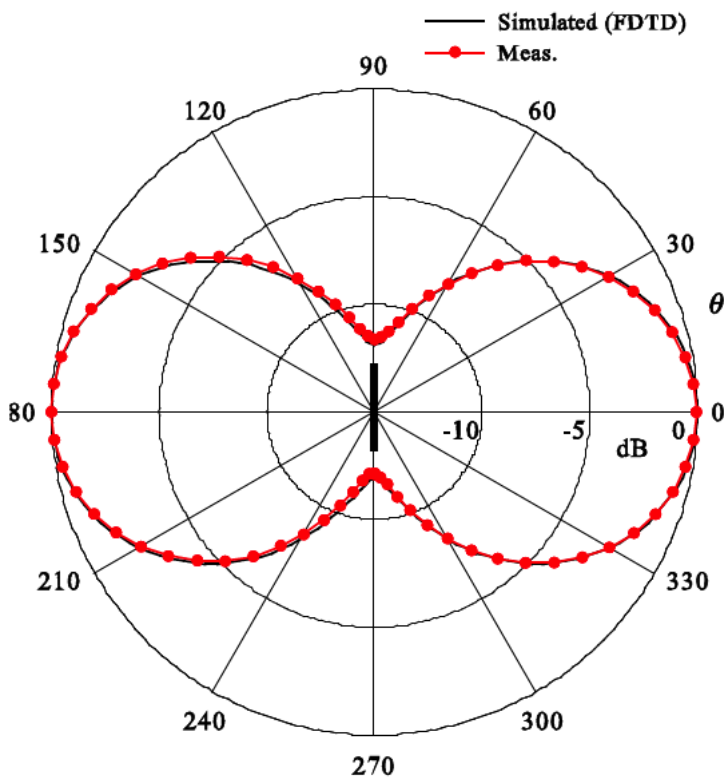


Figure 5.5: Horizontal radiation pattern at $f = 1.05$ GHz for the broadband, bidirectional, broadside design with hard-wired switches. Both patterns are normalized to 0 dB [3].

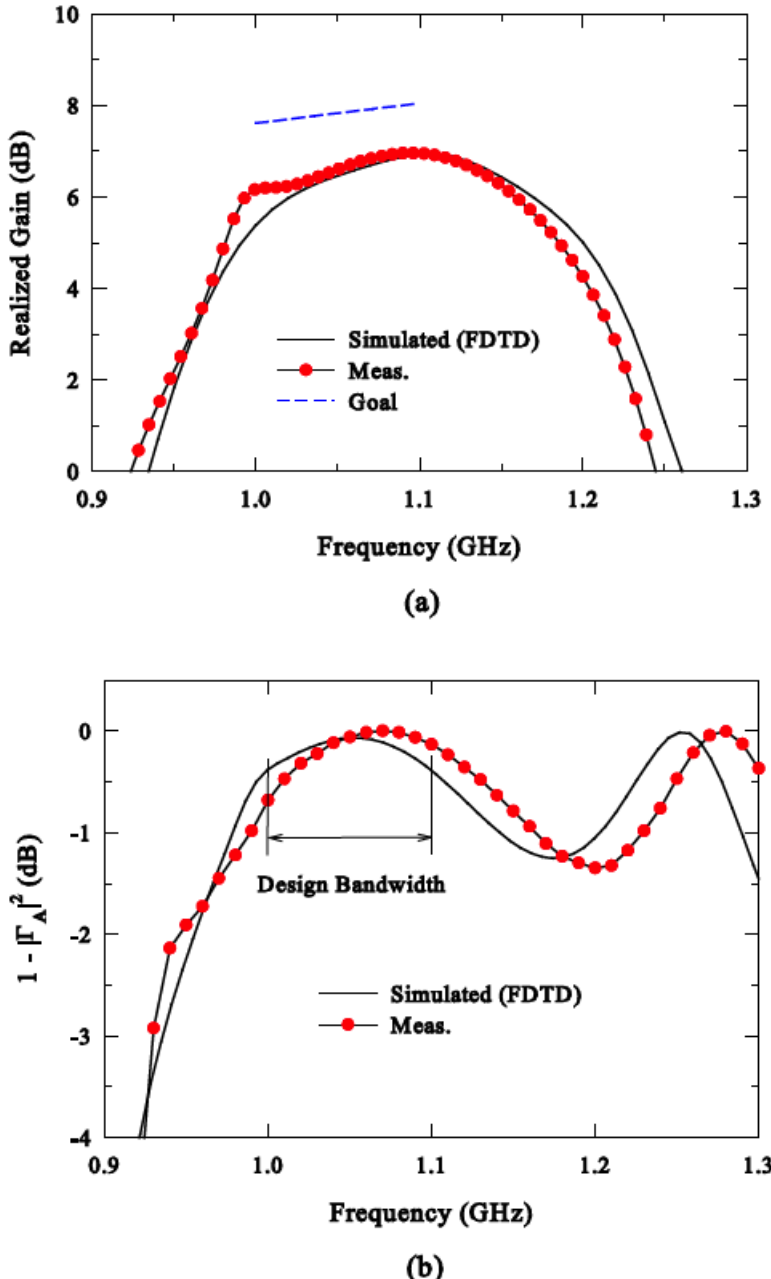


Figure 5.6: Results for the narrowband, unidirectional, end-fire design with hard-wired switches. (a) Realized gain versus frequency. (b) Gain reduction due to impedance mismatch: $(1 - |\Gamma_A|^2)$ [3].

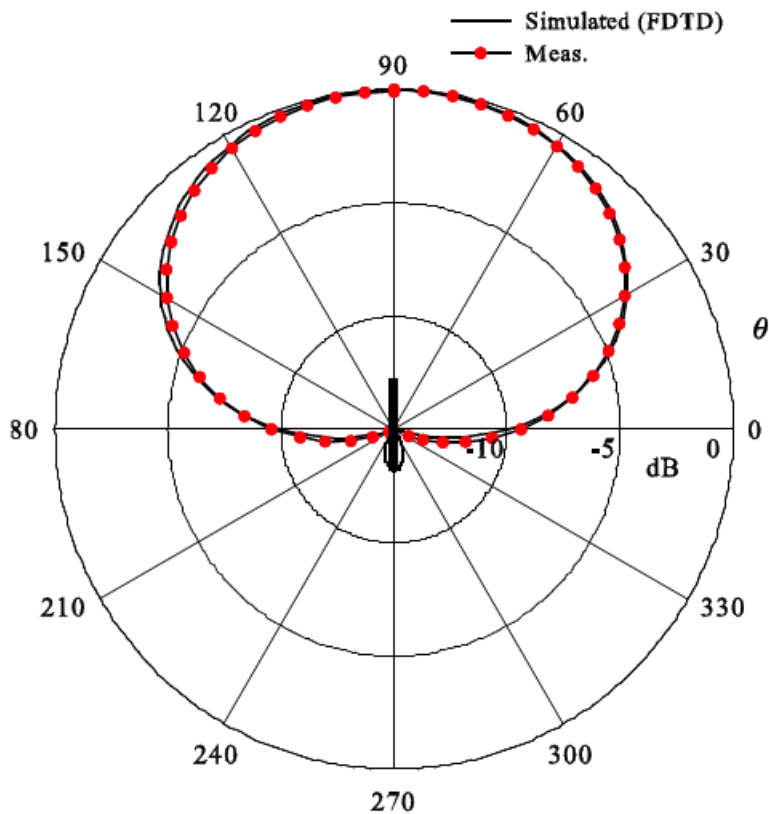


Figure 5.7: Horizontal radiation pattern at $f = 1.05$ GHz for the narrowband, unidirectional, end-fire design with hard-wired switches. Both patterns are normalized to 0 dB [3].

5.4.6 Observations on the Designed Configurations

In the configurations studied, approximately 30% to 60% of the switches were closed. One might expect that examination of the switch states for a particular design would reveal recognizable antenna structures—for example, the end-fire design might show strings of pads forming linear elements arranged like the driven element, reflector, and director of a Yagi-Uda array. However, as seen in Figure 5.3(b), this is not the case. In general, there is no simple, discernible relationship between the switch states and the design goal.

This lack of an obvious physical interpretation is consistent with the experience from conventional fragmented aperture design (Chapter 2): the GA discovers complex, non-intuitive structures that exploit the full electromagnetic physics of the problem. In the case of the Agile Aperture Antenna, the optimization is further complicated by the presence of the unconnected pads, which scatter electromagnetic energy and must be accounted for in the design. It is clear, however, that the switch connections near the feed point are often arranged to improve the impedance match between the antenna and the transmission line.

5.5 Discussion

The broadside and end-fire examples presented above, along with several other designs not shown, demonstrate that the Agile Aperture Antenna concept is viable: a single physical antenna can be reconfigured via its switch states to meet fundamentally different performance specifications. The excellent agreement between FDTD simulations and measurements further validates the design procedure.

However, for the Agile Aperture Antenna to transition from a laboratory concept to a practical technology, several challenges must be addressed. Most critically, a switch technology must be developed that can be electronically controlled without interfering with the electromagnetic performance of the antenna. The switches must introduce minimal insertion loss when closed, provide high isolation when open, and the control circuitry (bias lines, drivers) must not distort the antenna's radiation characteristics. **(Add any discussion of PIN diodes, MEMS switches, or other switch technologies that were investigated.)**

5.6 Acknowledgement

The author would like to thank Professor Glenn Smith for his dedication in writing the original IEEE paper [3] on which much of this chapter is based. The author also acknowledges the contributions of the full research team as described in [4].

References

- [1] J.G. Maloney, M.P. Kesler, P.H. Harms, and G.S. Smith, Fragmented Aperture Antennas and Broadband Ground Planes, U.S. Patent, No. 6,323,809 B1, November 27, 2001.

- [2] J. G. Maloney, M. P. Kesler, L. M. Lust, L. N. Pringle, T. L. Fountain, and P. H. Harms, "Switched Fragmented Aperture Antennas", in Proc. 2000 IEEE Antennas and Propagation Symposium, Salt Lake City, 2000, pp. 310-313.
- [3] L. N. Pringle, P. H. Harms, S. P. Blalock, G. N. Kiesel, E. J. Kuster, P. G. Friederich, R. J. Prado, J. M. Morris, and G. S. Smith, "A Reconfigurable Aperture Antenna Based on Switched Links Between Electrically Small Metallic Patches," IEEE Trans. Antennas Propagat., Vol. AP-52, pp. 1434-1445, June 2004.
- [4] (Add full reference for Maloney/Smith antenna chapters)
- [5] R. T. Lee and G. S. Smith, "A Design Study for the Basic TEM Horn Antenna," IEEE Antennas and Propagation Magazine, Vol. 46, pp. 86-92, February 2004.
- [6] Antenna Standards Committee of the IEEE Antennas and Propagation Society, IEEE Standard Test Procedures for Antennas, Institute of Electrical and Electronic Engineers, Inc., 1979.
- [7] D.L. Carroll, "FORTRAN Genetic Algorithm Front-End Driver," available on the web at cuaerospace.com/carroll/ga.html.

Chapter 6

Fragmented Array Elements

6.1 Direct Element Design

- direct element design
- use large scan paper to describe method for including scan (IEEE conf paper and slides)
- example of whole x-band for the IEEE paper
- 4:1 bandwidth
- discuss similarity to current sheets of Munk and Harris
- usually balanced fed with differential feeds and electronics

6.2 First Success

[2].

Figure A.1 is a schematic drawing showing a typical volume in which Maxwell's equations are to be solved. The volume is divided into unit cells each of volume.

References

- [1] K. S. Yee, "Numerical Solution of Initial Boundary Value Problems Involving Maxwell's Equations in Isotropic Media," *IEEE Trans. Antennas Propagat.*, Vol. AP-14, pp. 302-307, May 1966.
- [2] J. G. Maloney, G. S. Smith, and W. R. Scott, Jr., "Accurate Computation of the Radiation from Simple Antennas Using the Finite-Difference Time-Domain Method," *IEEE Trans. Antennas Propagat.*, Vol. AP-38, pp. 1059-1068, July 1990.

FRAGMENTED ANTENNA APERTURE OPTIMIZED TO OPERATE
FROM 800 MHZ TO 2.5 GHZ SYSTEM GAIN

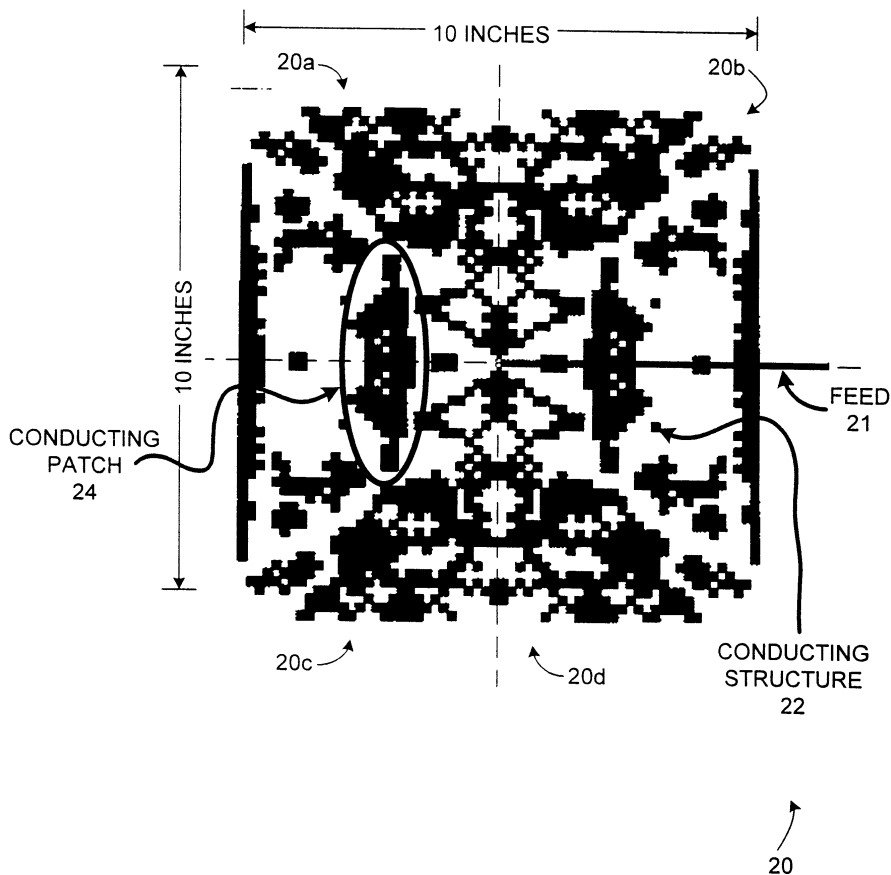


FIG. 3

Figure 6.1: Comparison of fragmented design to uniform aperture limit $2\pi A/\lambda^2$

- [3] J. J. Boonzaaier and C. W. Pistorius, "Thin Wire Dipoles ? A Finite-Difference Time-Domain Approach," *Electronics Lett.*, Vol. 26, pp. 1891-1892, 25 October, 1990.
- [4] D. S. Katz, M. J. Picket-May, A. Taflove, and K. R. Umashankar, "FDTD Analysis of Electromagnetic Wave Radiation from Systems Containing Horn Antennas," *IEEE Trans. Antennas Propagat.*, Vol. AP-39, pp. 1203-1212, August 1991.

Chapter 7

Wideband, Antenna Arrays

7.1 Introduction

Students of antenna design are taught that one can estimate the gain of an array antenna by multiplying the pattern of a single element by the array factor. This simplistic formula ignores mutual coupling between elements, which has traditionally bedeviled designers of phased arrays by introducing areas of scan blindness (combinations of frequency and scan angle for which the array is poorly matched). As the sophistication of numerical modeling codes has increased in concert with the availability of inexpensive parallel computing power, antenna designers have developed the ability to include the effects of mutual coupling in performance predictions. This in turn suggests the possibility of exploiting mutual coupling rather than avoiding it.

- connected array discovery
- show connected was key
- show progression with size
- mention need for ground plane or radiate both ways
- show two sided patterns again
- 10:1 bandwidth
- addition of reards to prevent unwanted resonances
- mention exceeding the bandwidth of current sheet antennas
- 33:1 bandwidth
- front back advantage of additional parasitic layers
- more complex backplane required for be ζ 12:1
- 100:1 design
- mostly backplane design

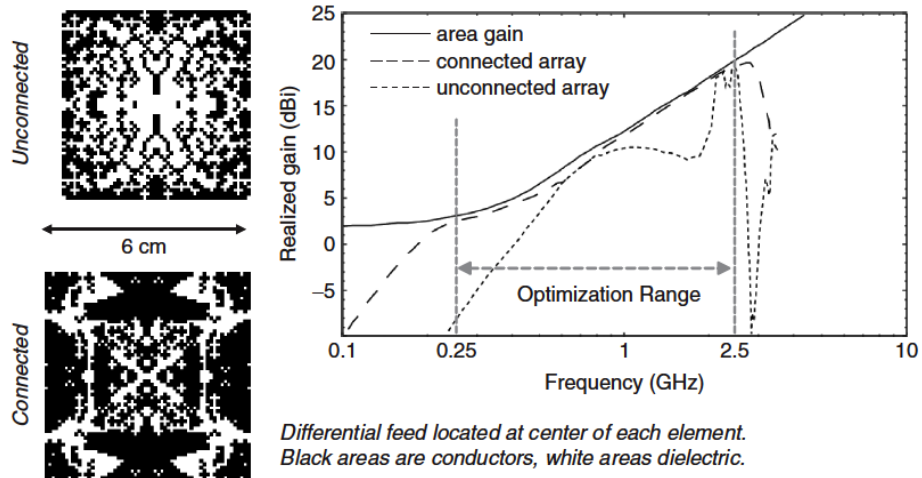


Figure 7.1: This design experiment compared performance of two 8x8 arrays. (a) Connected array element, (b) Unconnected array element, (c) Embedded element gain comparison for a central element in an 8x8 array. Notice that the connected array element far out performs the unconnected element. [Used with permission of Wiley]

7.2 Fragmented Array Antennas

The fragmented aperture design approach extended naturally into efforts to extend the instantaneous bandwidth of practical array antenna elements. The insight that led to a breakthrough in achievable bandwidths was the recognition that DC electrical connection between elements was actually useful and should be exploited. Subsequent multiple-octave array designs consistently featured these connections, which support continuous current paths that span multiple elements. For example, in an array with an 8:1 bandwidth, the radiated wavelength changes from approximately the width of two elements at the highest frequency to 16 elements at the lowest. With the connected array, continuous conducting pathways of sufficient length to support the necessary currents are present on the aperture.

As an experiment to demonstrate the importance of connected arrays, the 6-cm elements of Figure 3 were designed to operate from 0.25 - 2.5 GHz in an array with no ground plane. The aperture limited gain was thus approximately $2\pi A/\lambda^2$, since the apertures radiate equally in both hemispheres. The first element design was optimized with electrical connections between elements permitted, i.e., a connected array. The second element was optimized with a boundary enforced around each element to prevent conducting pathways between elements. The realized gain achieved by an 8 x 8 finite array of each element design is shown in the Figure 3(c). Because of the continuous current paths across element boundaries, the connected design is able to maintain a good impedance match over the full 8:1 bandwidth and thus achieves superior performance.

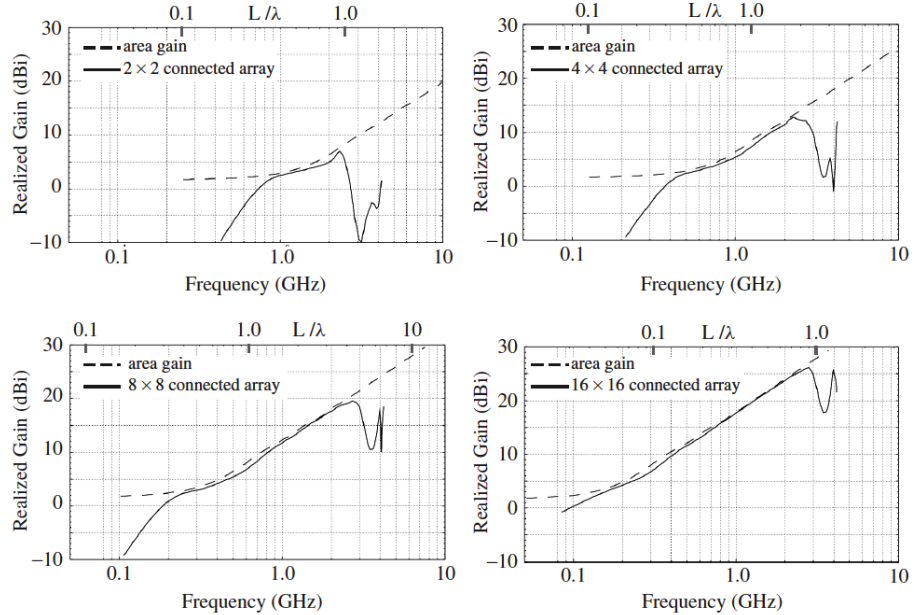


Figure 7.2: The connected element from Figure 7.1 was simulated in arrays of various sizes. The results show that the low-frequency performance limit is essentially proportional to overall array size. [Used with permission of Wiley]

Another key feature of the connected geometry is that the overall size of the array becomes a limiting factor on the lowest operating frequency. When the previous connected design was modeled in arrays of various sizes (again without a ground plane), the resulting low end performance was proportional to array size, as shown in Figure 4. Arrays of 2×2 , 4×4 , 8×8 , and 16×16 elements were simulated. For all cases, the upper frequency limit remained relatively constant, being limited by the element lattice spacing and resulting grating lobe formation. The low frequency limit, on the other hand, was approximately proportional to the overall array dimension.

To confirm the validity of these simulations, a fragmented array with 3 cm elements was designed and measured in 1999. The quantity modeled and measured was the embedded element realized gain (EERG), where one central element was active and others were terminated in matched resistive loads. This quantity measures the performance of an element in the array environment. An angle pattern cut of the EERG can be used to predict the scan performance of an array of these elements. This highlights the performance of the radiator without the need for expensive beam forming networks. As can be seen from Figure 5, the array achieves near aperture-limited gain at broadside over a 10:1 bandwidth, with excellent model-measurement agreement.

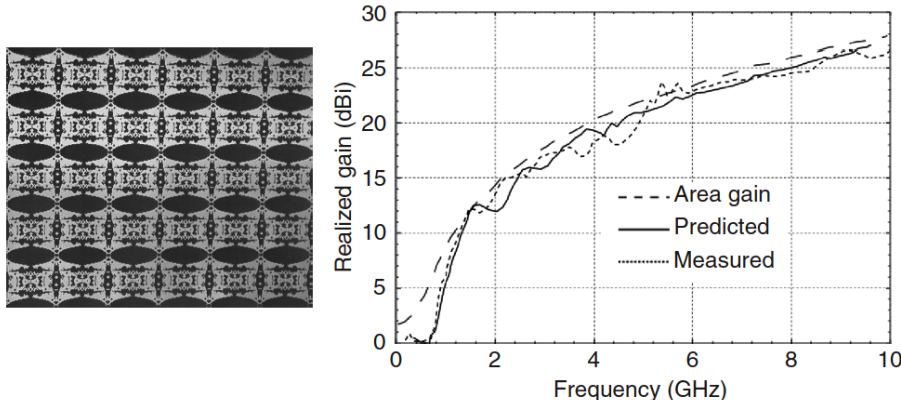


Figure 7.3: Embedded element realized gain for a central element of a 10×17 array with 3-cm square unit cells. [Used with permission of Wiley]

7.3 Wideband Backplanes: Planar 10:1 Arrays

Early explorations of the fragmented arrays (2000 and earlier) focused on basic questions of element connections, bandwidth limits, and natural impedance values [3]. These investigations typically either used no ground plane behind the radiating surface or accepted the limitations of simple ground planes. Ideally, a ground plane should be located $\lambda/4$ behind the broadside radiating surface of a planar antenna. Notionally, the backward-radiated energy travels a path length with a phase progression of 180 degrees that, together with the 180 degree phase inversion at the perfect electrical conductor (PEC) surface of the ground plane, causes the reflected energy to arrive in phase with the forward going radiation. Wideband antennas pose a difficulty, however, since λ varies widely over the operating bandwidth. In fact, when the ground plane is $\lambda/2$ behind the radiating surface (or an integer multiple of $\lambda/2$) the backward going radiation is reflected and arrives exactly out of phase with the forward radiation. This situation is illustrated in Figure 6, which shows the results of a simulation of a fragmented aperture radiator placed 2.5 cm in front of a PEC ground plane. The broadside gain is normalized to the area gain for this antenna. Without the ground plane, the radiator is well matched across the band, but because it is radiating in both directions the forward radiation only approaches -3dB, represented by the dashed line in the plot. With the ground plane, the gain approaches the maximum around 3 GHz, where the 2.5 cm represents a quarter of the free space wavelength and the ground plane provides almost a 3 dB increase in broadside gain. At 6 GHz, however, the ground plane is a half wavelength behind the radiating surface and the gain suffers a deep null. The null will be repeated every multiple of $\lambda/2$ (12 GHz, 18 GHz, etc.) Practical experience indicates that fragmented aperture designs can be extended to approximately 8:1 bandwidths before the half-wave null impact must be addressed.

The problem is made more complicated if the array is intended to scan over any significant volume, because the null frequency is dependent on the scan angle, as illus-

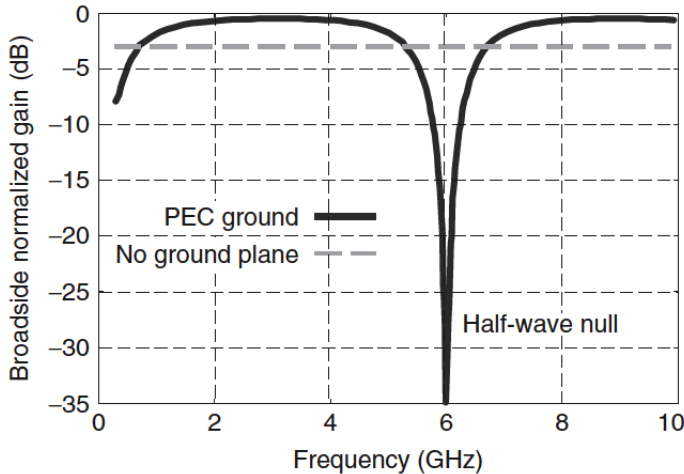


Figure 7.4: When a broadband radiating sheet is placed in front of a simple PEC ground plane, the resulting gain pattern will suffer nulls at frequencies where the separation distance is an integer multiple of a half wavelength (in this case, 6 GHz for a 2.5 cm separation). [Used with permission of Wiley]

trated in Figure 7. As the scan angle moves away from broadside the null frequency increases. The contour plot in the figure shows this trend.

Since the problem can be attributed to backward radiated energy, one is tempted to address it with absorbing solutions. Interestingly, the Salisbury screen absorbing structure has the desirable characteristic that its tuned absorption frequency increases with incidence angle, exactly analogous to the scan angle-frequency dependence of the half wave null. This was the inspiration for the “broadband screen” backplane which was developed to extend the frequency performance of fragmented apertures over a ground plane. As an example, Figure 7.6 shows the performance of a typical planar half way between the aperture layer and the ground plane. The backplane is most absorptive at exactly the frequency/angle combinations where the half-wave null occurs (and in fact at every odd multiple of half-wavelengths).

Figure 7.7 shows the normalized realized gain at broadside with the first generation broadband screen backplane. Now the aperture has recovered enough gain at the problem frequency to achieve near 50% efficiency. However, one can do better. For overall antenna performance, the impedance value, position, and even the number of r-card layers may be considered as free variables in the design. For example, if the 377-ohm r-card is replaced with a 225-ohm card, the realized gain is maintained within 2 dB of the aperture limit across the operating band of the antenna.

Figure 10 pictures a 10:1 design that was developed as a proof of concept using a single r-card broadband screen. The array demonstrated better than 50% efficiency over the operating band of 1-10 GHz. The plot in the right half of the figure shows normalized predictions of realized gain, or equivalently, insertion loss. The top curve

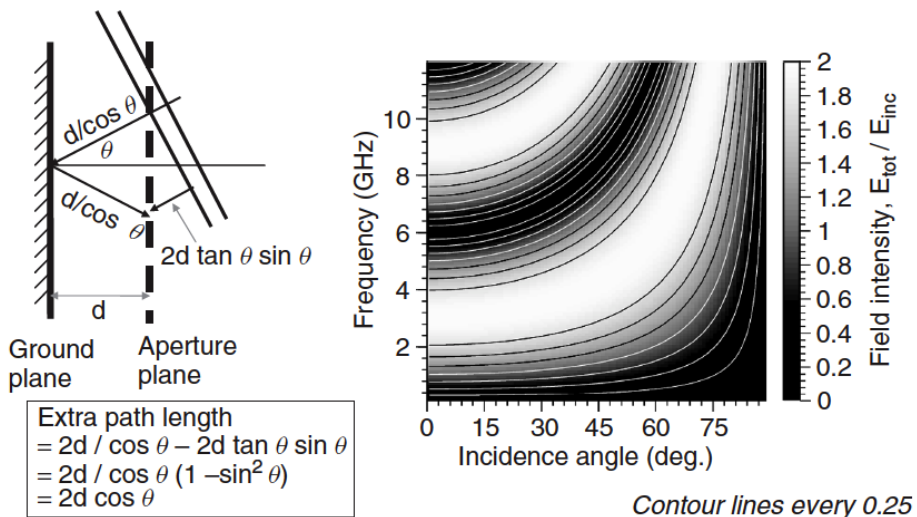


Figure 7.5: For normal incidence (or when a phased array is scanned to broadside) pattern nulls will occur when the ground plane is at a half wavelength separation. At scan angles off normal, the null will occur at higher frequencies. This geometry is illustrated in the diagram on the left above. The contour plot on the right shows the relationship between field intensity at the radiating surface and frequency and angle for a 2.5 cm separation. [Used with permission of Wiley]

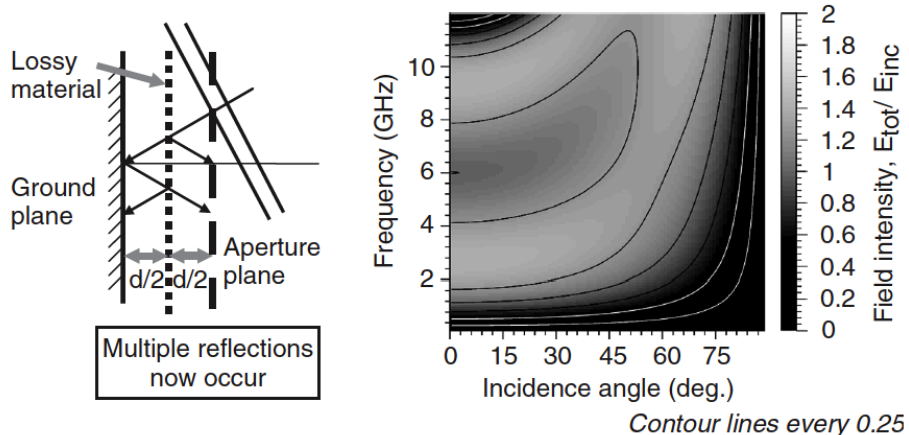


Figure 7.6: Here the radiating surface is located 2.5 cm in front of the PEC ground plane, but a 377-ohms/square r-card layer is placed halfway between radiator and ground plane, eliminating the deep null at $\lambda/2$. [Used with permission of Wiley]

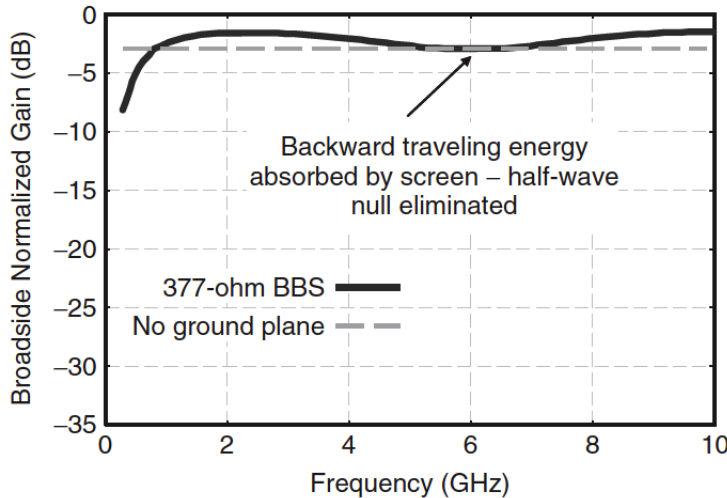


Figure 7.7: This plot of the normalized realized gain at broadside for the configuration of Figure 8 shows that the deep null at 6 GHz has been improved to only 3 dB insertion loss. [Used with permission of Wiley]

(normalized gain) shows the effects of resistive loss. The bottom curve (normalized realized gain) shows the combined effects of resistive and mismatch loss. Thus, the distance between the two curves is a measure of the impedance match for this design.

With a simple conducting ground plane behind a planar radiating surface, a standing wave occurs when the separation distance is one half wavelength (or an integer number of half wavelengths), which places a field null at the radiating surface. The resulting impedance mismatch is the cause of the deep dropout in the gain curve. In addition to the energy they dissipate, r-cards inserted in the backplane stack introduce additional reflection boundaries that ?break up? or redistribute the standing wave to avoid field cancellation at the radiating surface. As the operating bandwidth of the array spans more octaves, a simple ground plane introduces more half-wave nulls and the problem of defeating the standing wave becomes more complicated. Figure 11 shows an example of a radiating surface located three inches in front of a simple conducting ground plane. The resulting standing wave produces interference nulls approximately every 2 GHz. When the empty cavity is replaced by an optimized broadband screen with six r-card layers in the backplane stack, the standing wave nulls are eliminated. Figure 12 compares the performance of the empty cavity with the broadband screen over frequency and scan angle. The nulls are effectively controlled to scan angles of 60 degrees or more.

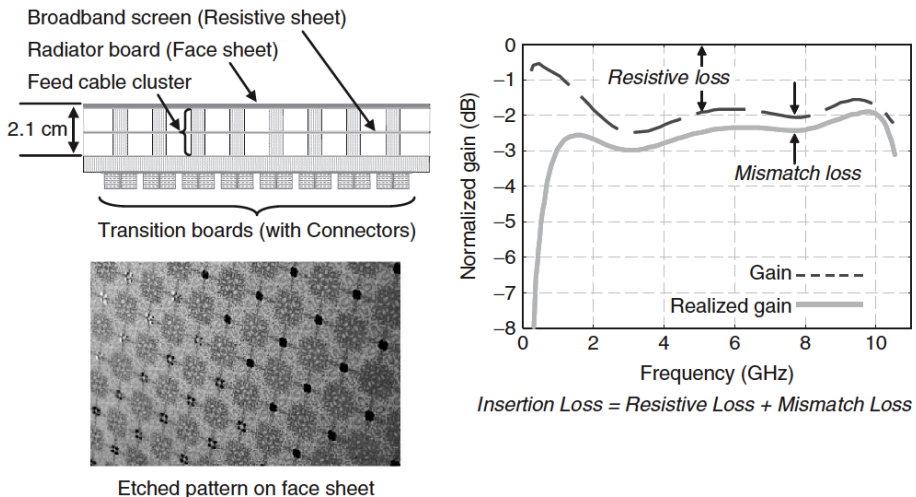


Figure 7.8: The first array built using the broadband screen backplane was this 10:1 design. Efficiency was better than 50% (< 3 dB insertion loss) from 1 to 10 GHz. [Used with permission of Wiley]

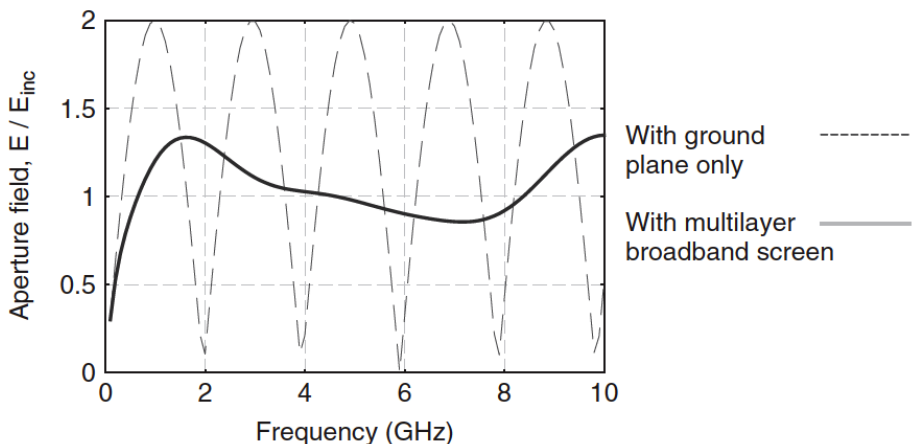


Figure 7.9: Aperture fields 3 inches in front of a PEC surface, with and without a broadband screen backplane in place. [Used with permission of Wiley]

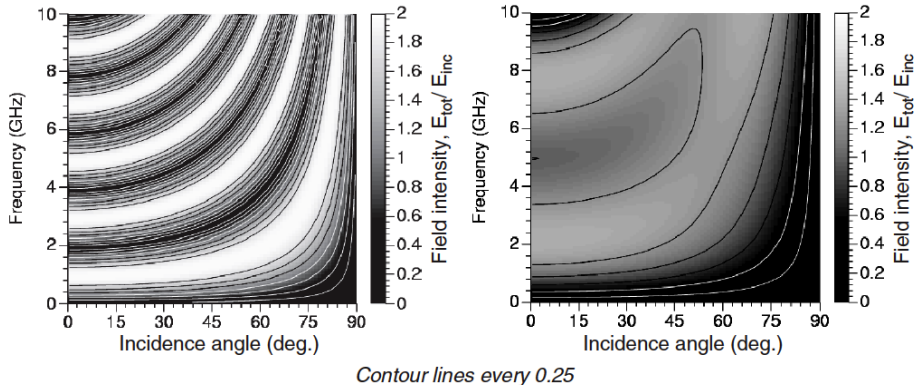


Figure 7.10: Contour plots comparing the configurations of Figure 7.9 over a range of scan angles. [Used with permission of Wiley]

7.4 Multi-layer Radiators: 33:1 Bandwidth Arrays

A broadband screen backplane can control half-wave nulls, but it uses a loss mechanism to do so. While it is not necessary to attenuate all of the backward radiated energy, some loss is inevitable with this approach. It would be better to radiate energy only into the forward hemisphere, and eliminate the possibility of backward-radiated energy reflecting off of a ground plane to add out of phase with the forward directed radiation. As a thought experiment, consider the ideal planar radiator with no thickness in Figure 13. Notionally, radiation must occur equally into both hemispheres since nothing distinguishes one side from the other. However, if the radiating layer has some thickness, then asymmetries may be introduced that cause the surface to radiate preferentially in one direction, as in the second antenna of Figure 13. For example, if 90% of the energy is made to radiate into the forward hemisphere, then even if the backward radiated energy is reflected and returns 180 degrees out of phase, it will only reduce the transmitted power to 80% of the maximum value.

This principle may be exploited by using multiple radiating layers in front of the ground plane. The radiating layers may be actively driven, or they may be parasitic, analogous to the directors in a Yagi-Uda antenna. In Figure 14, two radiating layers approximately 8 mm apart with no ground plane were optimized using the fragmented aperture design process. The design goal was to maximize gain in the forward hemisphere. The plot shows the normalized forward-going and backward-going radiation, demonstrating good preferential radiation, or front-to-back ratio (F/B), over the upper octave of the design region (1-10 GHz). As the wavelength gets longer, the electrical separation between radiating layers becomes insufficient to direct the radiation. The region of effectiveness for this approach is enough to produce the 10:1 design of Figure 15, where the realized gain remains within 3 dB of the maximum across the band. This design is for illustrative purposes only, as it has no realistic feed structures or loss.

The extent to which using multiple radiating face sheet layers may improve the

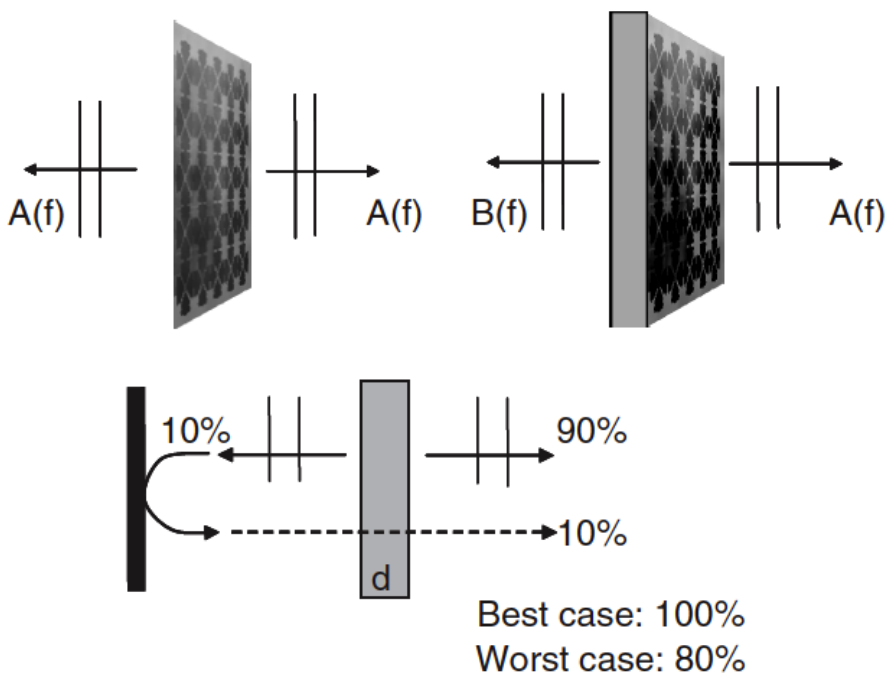


Figure 7.11: Thought experiment demonstrating the benefit of preferentially radiating in one direction to mitigate ground plane nulls. This is possible with asymmetric radiation, which can be achieved with a radiator thickness $\gtrless 0$. [Used with permission of Wiley]

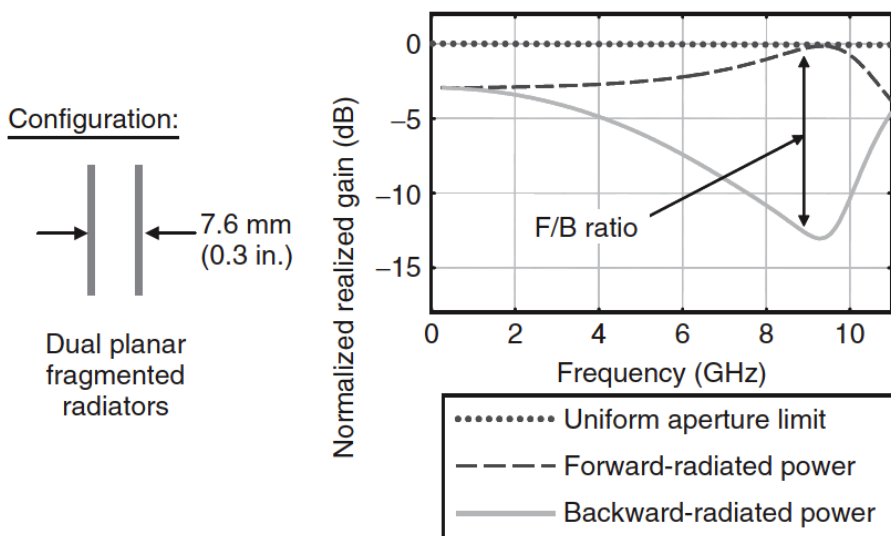


Figure 7.12: Idealized design with simultaneously optimized radiating layers. The design goal was to maximize front-to-back ratio. [Used with permission of Wiley]

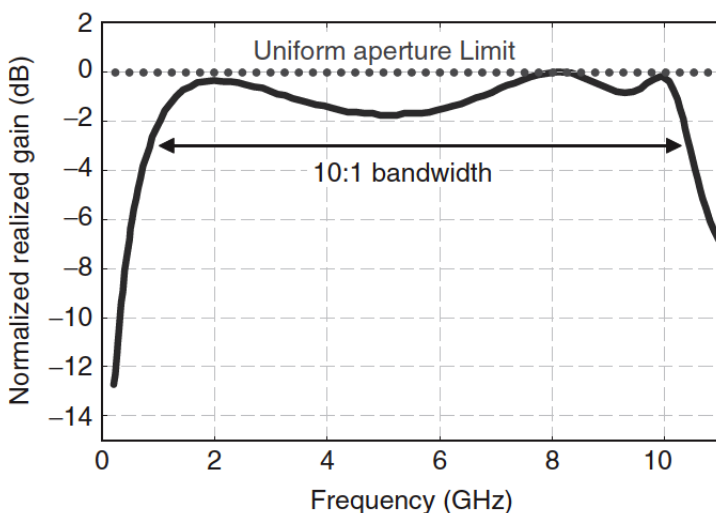


Figure 7.13: The use of parasitic layers to direct radiation forward may also be accomplished in the presence of a PEC backplane, as in this example, where insertion loss is kept below 2 dB over most of a 10:1 bandwidth. [Used with permission of Wiley]

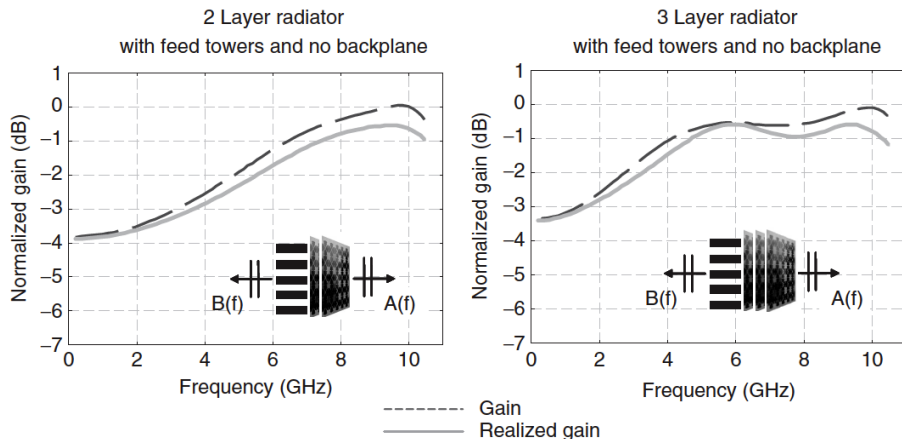


Figure 7.14: Design experiments with two and three radiating face sheets. The ground plane has been replaced in each simulation with a perfectly absorbing layer as the back boundary condition. Thus, normalized gain levels above -3 dB may be attributed to the F/B ratio. [Used with permission of Wiley]

bandwidth of the antenna depends on the number and spacing of the face sheets. In Figure 16, the antenna designs use two and three face sheets, respectively. These simulations include realistic feed structures, but the ground planes have been replaced by perfectly matched absorbing layers in the simulation. With two face sheets, the antenna exhibits enhanced gain over most of the upper octave. With three, antenna gain is enhanced over the upper two octaves.

Design of fragmented elements for phased arrays with operating bandwidths beyond 10:1 are best executed through a judicious combination of a multi-layer radiator with a broadband screen backplane. In partnership with Northrop Grumman Electronics Systems, GTRI has built and measured two laboratory proof-of-concept radiators with 33:1 bandwidths, each incorporating both design strategies. Each design consisted of a three-layer radiator stack over a six r-card backplane stack. In the first design, two face sheets were driven by the feeds and the third was parasitic. In order to simplify the manufacturing process, the second design had only the innermost face sheet driven, with two parasitic outer layers. Figure 17 shows the performance of the second design in a periodic simulation, which eliminates finite array edge effects. The simulation includes realistic feed structures and material properties. Gain is normalized to the element area gain, so the 0 dB line represents ideal performance. Note that the design achieves nearly 1 dB or better insertion loss over the upper octave, with better than 3 dB insertion loss over the entire 0.3 ? 10 GHz design bandwidth. Representative measurements of the second design are presented below.

The simulations were supported with measurements of a test piece on three different antenna ranges covering the entire operating bandwidth. These measurements were not only consistent across all three ranges, but they validated the simulation results. The test antenna was a 23 x 23 element, dual linear polarized array with the center

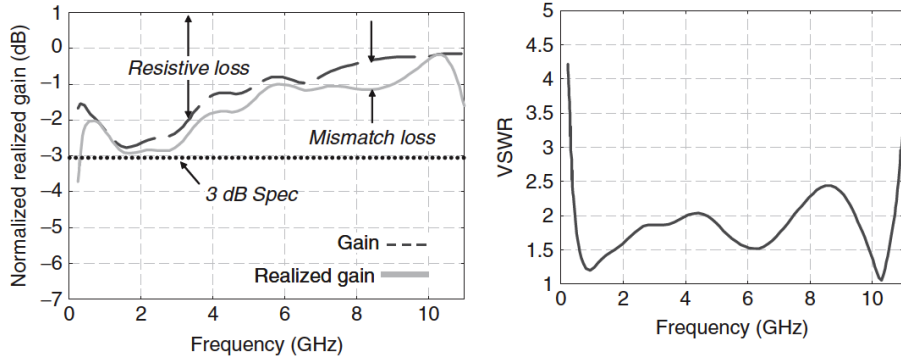


Figure 7.15: Predicted performance of the 33:1 antenna design. In this periodic simulation, antenna efficiency is shown to be better than 50% over the entire bandwidth of 0.3-10 GHz for an actual antenna designed with realistic feed structures. [Used with permission of Wiley]

element actively driven and all surrounding elements terminated in matched 188-ohm impedances at the feed points. Figure 18 illustrates the composition of one element of the array in cross section, with cartoons of the etched unit cell pattern on each face sheet and a photo of the test antenna.

Broadside frequency scans of the embedded element realized gain (EERG) are plotted in Figure 19. The EERG is obtained by driving one element and terminating the rest with matched loads. This greatly reduces the cost of the measurement setup and test piece, as beamformer electronics are not required. Achievable scan volume may be inferred from the beamwidth of the EERG angle pattern cuts.

The figure compares the measurement results at broadside to predictions. The element area gain, which represents the physical limit for antenna performance, is denoted by the dashed line. The predicted EERG at broadside is denoted by the solid line. Compared to these are four measured data sets from the three different antenna ranges, including three different calibration horns spanning the 33:1 bandwidth. Data was also measured on both V-pol and H-pol feeds (both sets should be equivalent at broadside for this symmetric design). The measured data show excellent consistency across ranges and at both sets of feed points, and excellent agreement with the predictions. The measurements showed approximately one dB more insertion loss at the high end than predicted. The difference is more than can be attributed to resistive loss in the feed cables and on the metal radiating surfaces. It is likely due to slight imperfections in the assembly of the radiator. Performance at the high end is particularly sensitive to the position of the three layers at the end of the feed cables, and their planarity in the assembled test piece was affected by warping in the etched sheets. This slight drop-off is removed in Figure 20 to facilitate angle pattern comparisons. These patterns allow detailed comparison of measured and modeled EERG over angle cuts at several discrete frequencies. Again, model-measurement agreement is excellent, with the models predicting features such as the ripple at 2 GHz due to finite array edge effects and the

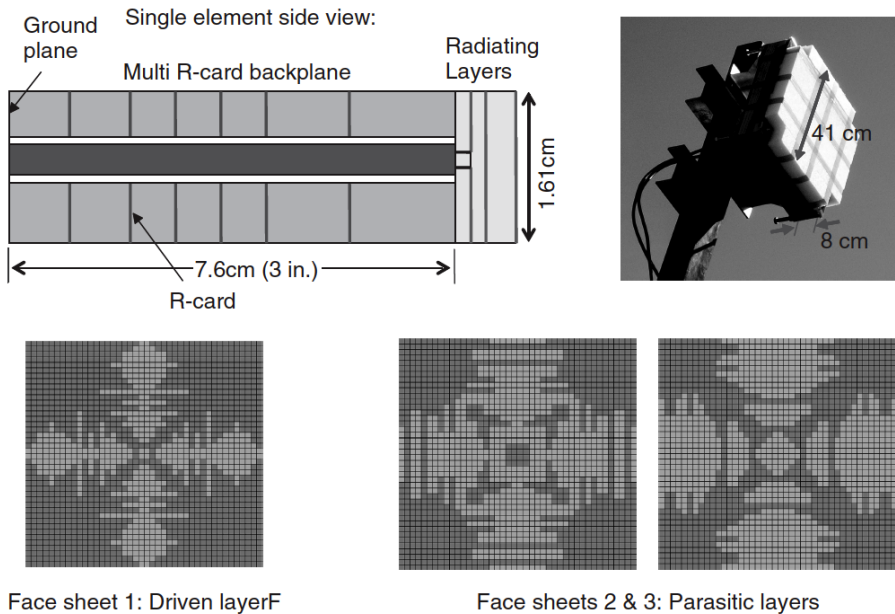


Figure 7.16: Construction details of one 33:1 antenna design, including a photo of the test piece used to measure embedded element realized gain (EERG). [Used with permission of Wiley]

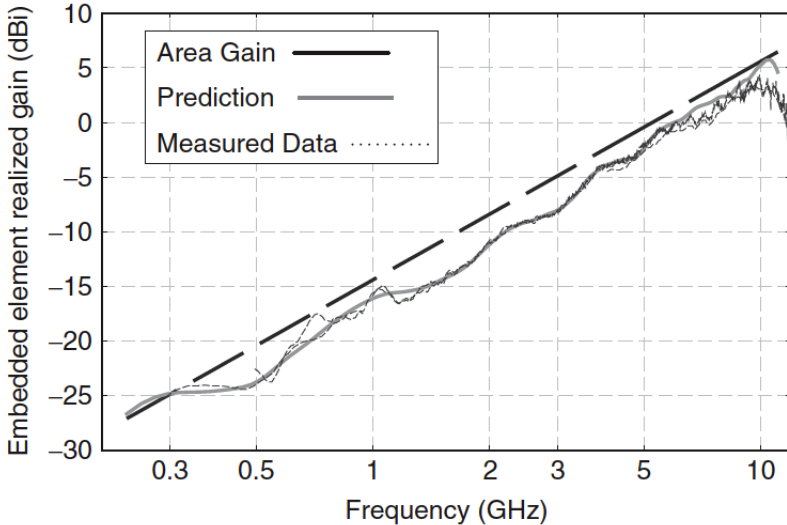


Figure 7.17: The plot shows a compilation of measured data at broadside for the 33:1 test antenna (3 antenna ranges, two polarizations). The measured data is plotted against numerical predictions of performance, along with the element area gain representing ideal performance. [Used with permission of Wiley]

narrowing of the scan volume above 8 GHz.

Figure 21 presents the measured EERG data from three different overlapping data sets for H-plane scans and two for E-plane scans. The contour plots show angle cuts plotted horizontally at each frequency. Each angle cut (horizontal line across the contour plot) has been normalized so that the maximum value at each frequency is zero (i.e., frequency slope has been removed from the data sets.) The resulting image shows the achievable scan volume as a function of frequency for a fully driven array antenna with this design. That scan volume, as defined by the 3 dB points, is approximately +/- 60 degrees over most of the band, with some narrowing above 9 GHz in the H-plane and above 7 GHz in the E-plane. Note also that the featured scan volume shows no evidence of any suck-outs or scan blindness over the operating bandwidth.

Our experience with several wideband phased array designs has produced empirical evidence for a rule of thumb regarding the thickness of these wideband radiators. Figure 22 compiles results for five fragmented array designs with bandwidths greater than an octave. Designs with bandwidths less than 10:1 used simple ground planes; antennas with bandwidths of 10:1 or greater incorporated broadband screen backplanes. In each case, the overall thickness is dictated not by the bandwidth, but by the lowest operating frequency. For cavities filled with air or low-dielectric foams, the antenna thickness will be approximately $\lambda/12$ at the lowest frequency.

Conclusions The successful design of ultra wideband phased arrays has been enabled by several factors. These designs require high-fidelity time domain EM solvers. The necessity to optimize over many frequencies would be time prohibitive if the de-

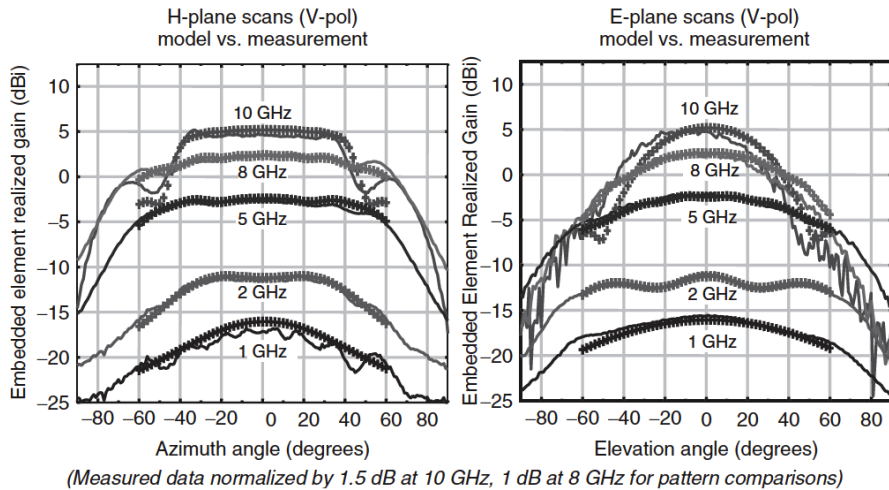


Figure 7.18: Comparison of modeled (solid lines) and measured (data markers) EERG pattern cuts at several discrete frequencies. Again, note the excellent agreement between prediction and measurement. [Used with permission of Wiley]

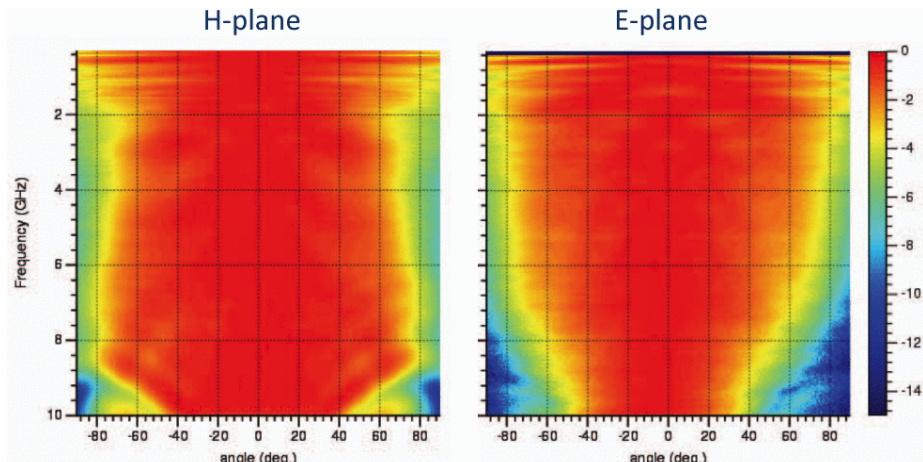


Figure 7.19: Compilation of measured angle cuts normalized to the maximum value at each frequency. Resulting contours indicate achievable scan volume. Note the lack of scan blindness in the operating regions. [Used with permission of IEEE]

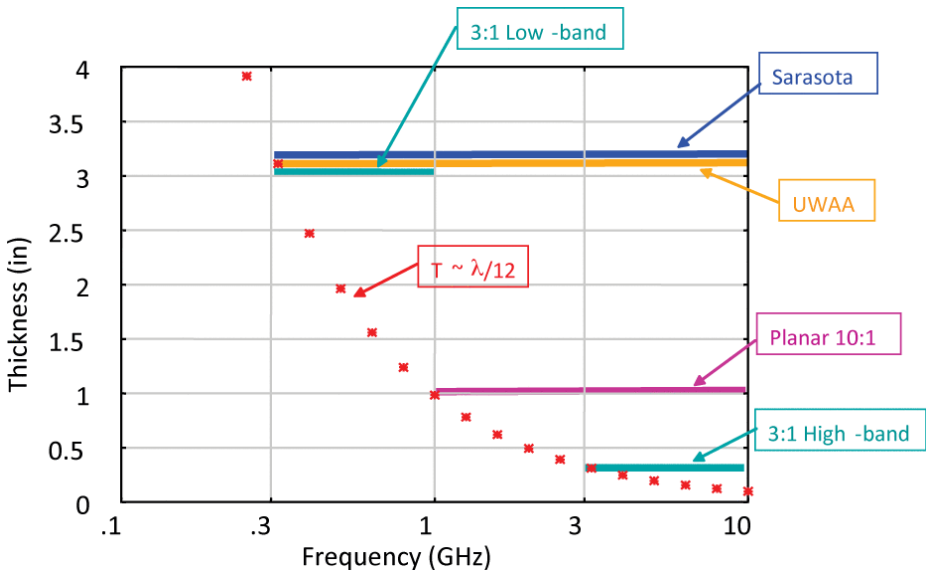


Figure 7.20: Results of several design exercises for fragmented arrays. For air-filled cavities, the antenna thickness is approximately $l/12$ at the lowest operating frequency. [Used with permission of IEEE]

signs were done with frequency domain codes. Designs referenced in this chapter were all developed using a finite-difference time-domain code, the results of which can then be Fourier transformed to produce the requisite range of frequency predictions. The code is highly validated, but it was developed in house so we understand how to enhance the speed of simulations by sacrificing some accuracy when necessary. In early design stages, it is important to move through iterations rapidly to converge on a ?pretty good? design. Then in the design?s final stages, accurate predictions are required to account for realistic details such as feed structures and material characteristics. These highly accurate modeling codes require computing hardware with sufficient processing power and memory to handle fine details, and this is accomplished using relatively inexpensive Beowulf clusters of Linux-based PCs.

With the appropriate modeling tools and computing infrastructure, GTRI was able to develop the essential features for ultra wideband planar phased arrays: (1) Connected arrays to span several octaves; (2) Broadband backplane stacks to mitigate half-wave nulls introduced by a ground plane; (3) Multi-layer radiators to enhance high frequency performance with front-to-back ratio, thus leveraging the backplane improvements at low frequencies; and (4) Fragmented aperture radiators to accomplish impedance matching in the presence of feed structures, material substrates, multiple layers, etc. Measured results confirm the success of these designs for bandwidths up to 33:1. Preliminary work suggests that phased array operation over bandwidths of 100:1 or more is possible.

7.5 Acknowledgement

Personally, the author would like to thank Mr. Paul Friederich, for his efforts in converting the “How to make a 33:1 bandwidth array antenna” presentation into the original chapter that is the source material for this chapter [1].

References

- [1] W. Croswell, T. Durham, M. Jones, D. Schaubert, P. G. Friederich and J. G. Maloney, "Wideband Arrays," Chapter 12, Modern Antenna Handbook, Balanis, 2011.
- [2] K. S. Yee, "Numerical Solution of Initial Boundary Value Problems Involving Maxwell's Equations in Isotropic Media," IEEE Trans. Antennas Propagat., Vol. AP-14, pp. 302-307, May 1966.
- [3] J. G. Maloney, G. S. Smith, and W. R. Scott, Jr., "Accurate Computation of the Radiation from Simple Antennas Using the Finite-Difference Time-Domain Method," IEEE Trans. Antennas Propagat., Vol. AP-38, pp. 1059-1068, July 1990.
- [4] J. J. Boonzaaier and C. W. Pistorius, "Thin Wire Dipoles ? A Finite-Difference Time-Domain Approach," Electronics Lett., Vol. 26, pp. 1891-1892, 25 October, 1990.
- [5] D. S. Katz, M. J. Picket-May, A. Taflove, and K. R. Umashankar, "FDTD Analysis of Electromagnetic Wave Radiation from Systems Containing Horn Antennas," IEEE Trans. Antennas Propagat., Vol. AP-39, pp. 1203-1212, August 1991.

Chapter 8

MetaMaterials and Antennas

JOHN SCHULTZ AND JAMES G. MALONEY

8.1 Introduction To MetaMaterials

Bla Bla BLA

8.2 Slicing

In the Yee algorithm, both space and time are discretized, with the increments in space for rectangular coordinates being Δx , Δy , Δz and the increment in time being Δt [1]-[2].

Figure A.1 is a schematic drawing showing a typical volume in which Maxwell's equations are to be solved. The volume is divided into unit cells each of volume. The partial derivatives in Maxwell's equations are approximated by ratios of differences, as shown in 8.1.

$$\frac{\partial E_x}{\partial z} \approx \frac{\Delta E_x}{\Delta z}, \quad \frac{\partial H_y}{\partial t} \approx \frac{\Delta H_y}{\Delta t} \quad (8.1)$$

8.2.1 examples

This section contains some example designs based on Figure A.1

8.3 Dicing

In section 8.2, slicing was introduced. In this section we will discuss dicing the material in a cubical fashion.

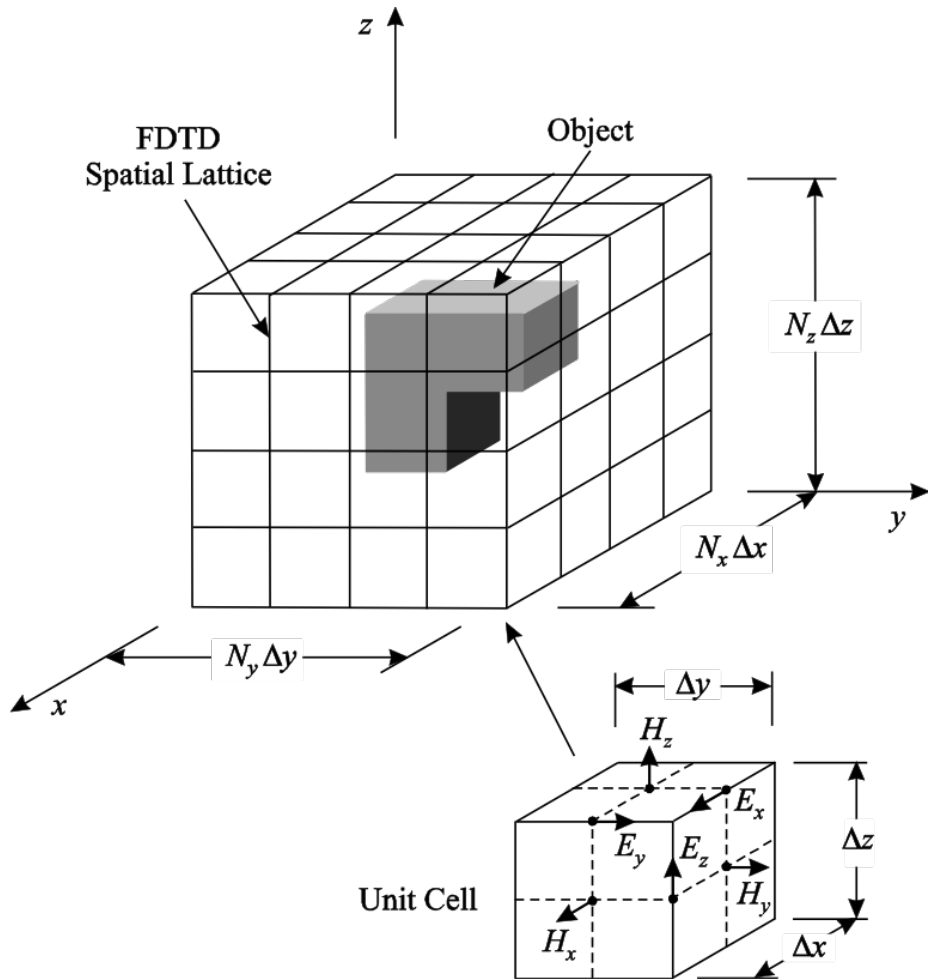


Figure 8.1: Schematic drawing showing the computational volume, FDTD spatial lattice, and unit cell.

References

- [1] K. S. Yee, "Numerical Solution of Initial Boundary Value Problems Involving Maxwell's Equations in Isotropic Media," IEEE Trans. Antennas Propagat., Vol. AP-14, pp. 302-307, May 1966.
- [2] J. G. Maloney, G. S. Smith, and W. R. Scott, Jr., "Accurate Computation of the Radiation from Simple Antennas Using the Finite-Difference Time-Domain Method," IEEE Trans. Antennas Propagat., Vol. AP-38, pp. 1059-1068, July 1990.
- [3] J. J. Boonzaaier and C. W. Pistorius, "Thin Wire Dipoles ? A Finite-Difference Time-Domain Approach," Electronics Lett., Vol. 26, pp. 1891-1892, 25 October, 1990.
- [4] D. S. Katz, M. J. Picket-May, A. Taflove, and K. R. Umashankar, "FDTD Analysis of Electromagnetic Wave Radiation from Systems Containing Horn Antennas," IEEE Trans. Antennas Propagat., Vol. AP-39, pp. 1203-1212, August 1991.

Appendix A

Computational Modeling of Antennas

A.1 Acknowledgement

To start, I would like to personally thank Professor Glenn Smith, Georgia Tech Regents Professor Emeritus, for his tremendous help in compiling this chapter on the modeling of antennas. The material was recently most published in [41], and earlier in [7].

A.2 Introduction

The finite-difference time-domain (FDTD) method is a computational procedure for solving Maxwell's equations that is based on a clever algorithm first proposed by Kane S. Yee in 1966 [1]. When Yee proposed his algorithm, the method was computationally intensive in terms of both storage and run time, and only problems of very modest size could be solved using the best computational facilities (mainframe computers). Since then the power of computers has steadily increased, as has the popularity of the FDTD method. The first comprehensive analyses of practical antennas using the method were performed during the early 1990's, and today such computations are routinely performed on personal computers [2]-[6].

The purpose of this article is to introduce the reader to the rudiments of the FDTD method as applied to practical antennas. It is hoped that after viewing the article, the reader will understand the power and limitations of the method and be in a position to decide whether or not the FDTD method is suitable for analyzing his/her antenna problem. Because of the limited space, we cannot provide the details for implementing the method in a computer program. Readers interested in writing their own program are referred to reference [7] for the details; others may wish to use one of the commercially available FDTD computer codes.

A.3 The Basic FDTD Algorithm

In the Yee algorithm, both space and time are discretized, with the increments in space for rectangular coordinates being $\Delta x, \Delta y, \Delta z$ and the increment in time being Δt [8], [9]. Figure A.1 is a schematic drawing showing a typical volume in which Maxwell's equations are to be solved. The volume is divided into unit cells each of volume. The electromagnetic constitutive parameters ($\epsilon = \epsilon_r \epsilon_0, \mu = \mu_r \mu_0, \sigma$) can vary from cell to cell, and they are used to define different objects within the volume¹. The six components of the electromagnetic field ($E_x, E_y, E_z; H_x, H_y, H_z$) are distributed over a unit cell (Yee cell) as shown in the inset. Notice that all of the components are located at different points within the cell, and the components of H are displaced from those of E by one half of a spatial increment, e.g., $\Delta x/2$. Although not shown in the figure, the components of H are also evaluated at points displaced by one half of a time increment, viz, $\Delta t/2$, from those of E .

The partial derivatives in Maxwell's equations are approximated by ratios of differences, for example,

$$\frac{\partial E_x}{\partial z} \approx \frac{\Delta E_x}{\Delta z}, \quad \frac{\partial H_y}{\partial t} \approx \frac{\Delta H_y}{\Delta t} \quad (\text{A.1})$$

For the spatial derivatives, the increment that occurs in the numerator is formed by differencing corresponding field components from adjacent unit cells, and for the temporal derivatives, it is formed by differencing field components from two adjacent time steps, e.g., t and $t + \Delta t$. The discretized Maxwell's equations are arranged to form two sets of difference equations known collectively as "update equations." The first set of difference equations, which we will call A, determines the change in the magnetic field, $H(t + \Delta t/2) - H(t - \Delta t/2)$, from the electric field at an intermediate time step, $E(t)$, and the second set of difference equations, which we will call B, determines the change in the electric field, $E(t + \Delta t) - E(t)$, from the magnetic field at an intermediate time step, $H(t + \Delta t/2)$.

At the start of the computation, we have the initial conditions: Throughout the computational volume, the electric field is known at time $t = 0$, and the magnetic field is known at the earlier time $t = -\Delta t/2$. The update equations A are then used with the initial conditions to obtain the magnetic field at time $t = \Delta t/2$. Next, the update equations B are used with the magnetic field that we just obtained at time and the electric field at time $t = 0$ to obtain the electric field at time $t = \Delta t$. This procedure of alternately applying update equations A and B to advance the solution in time is known as "marching-in-time" or "stepping-in-time." It is repeated until the electromagnetic field is known throughout the computational volume at the desired time $t = t_{\max} = N_t \Delta t$.

The choice for the increments of space and time ($\Delta x, \Delta y, \Delta z$, and Δt) is critical to the success of the algorithm, because their size determines how well the solution to the difference equations approximates the solution to Maxwell's equations. The spatial and temporal increments cannot be chosen independently; we can show that for

¹Here we mention only simple materials with constant permittivity, permeability, and electrical conductivity. In the FDTD method there are techniques to handle more complicated materials, such as those with dispersive and anisotropic properties [9].

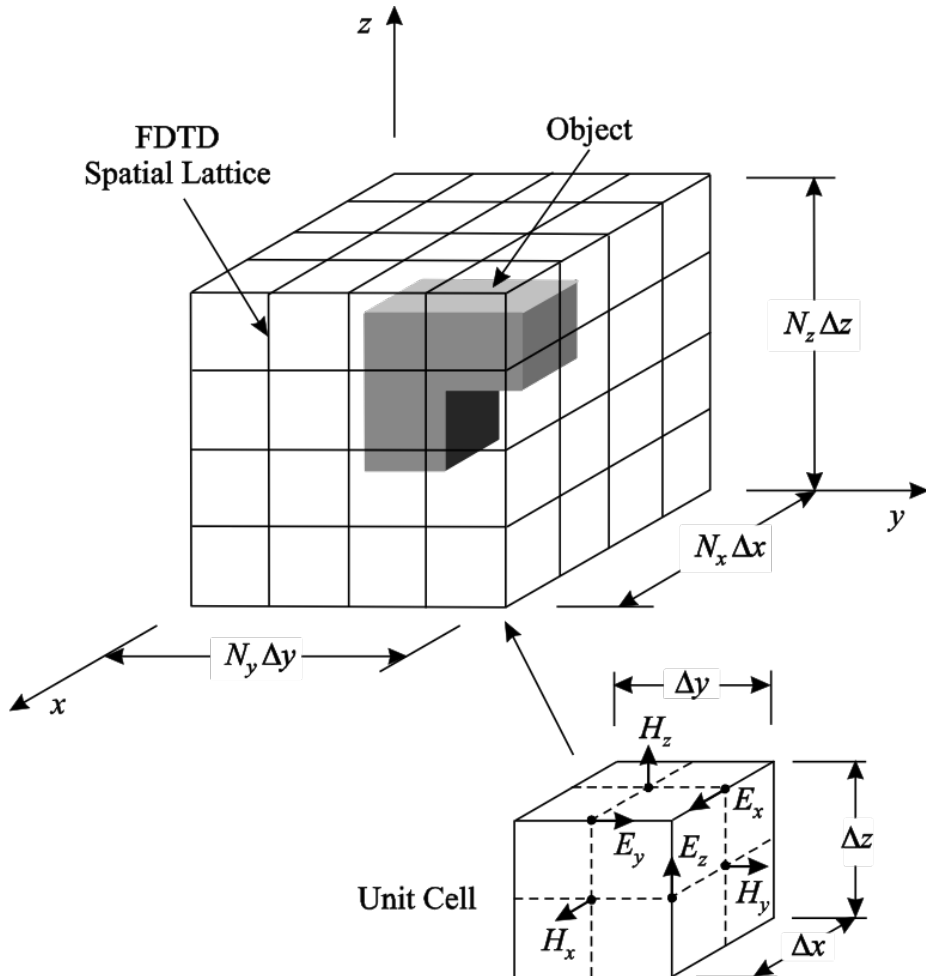


Figure A.1: Schematic drawing showing the computational volume, FDTD spatial lattice, and unit cell.

convergence (as $\Delta x \rightarrow 0$, $\Delta t \rightarrow 0$, etc.) and stability of the algorithm the increments must satisfy the Courant-Friedrichs-Lowy condition, which for free space is

$$c\Delta t \sqrt{\frac{1}{\Delta x^2} + \frac{1}{\Delta y^2} + \frac{1}{\Delta z^2}} \leq 1. \quad (\text{A.2})$$

For cubical cells, $\Delta x = \Delta y = \Delta z$, (2) becomes $S = c\Delta t\Delta x \leq \sqrt{1/3}$, where S is referred to as the “Courant number,” and a reasonable choice is $S = 1/2$.

Additional restrictions for the spatial and temporal increments can only be obtained from knowledge of the variation of the field (the solution) in space and time. We basically have to make Δz and Δt in (A.1) small enough that the errors incurred by replacing the derivatives by the ratios of differences are acceptable. One obvious requirement is that the size of the spatial cells must be small enough to resolve all of the important structural features and the local field surrounding these features. Another requirement is that the error introduced by a phenomenon known as “numerical dispersion” must be negligible.

When there is numerical dispersion, a pulse that starts out with one shape ends up with a different shape after propagating through the FDTD lattice. Numerical dispersion is caused by the different frequency components of the pulse propagating through the lattice with different phase velocities. It can be quantified by considering a time-harmonic plane wave of angular frequency propagating in free space along one of the axes of the FDTD lattice, say the x axis. Assuming cubical cells, the numerical phase velocity, \bar{v}_p , for the wave, normalized to the speed of light in free space c , is

$$\frac{\bar{v}_p}{c} = \pi \left\{ N_\lambda \sin^{-1} \left[\frac{1}{S} \left(\frac{\pi S}{N_\lambda} \right) \right] \right\}^{-1}, \quad (\text{A.3})$$

in which $N_\lambda = \lambda/\Delta x$ is the number of cells per wavelength [10]. Figure 2 is a graph of this equation showing the relative error in the phase velocity in percent (solid line) and a related quantity, the error in the phase per cell in degrees (dashed line). Notice that the phase velocity is less than the speed of light, and that the error decreases monotonically with an increase in N_λ . For large (say $N_\lambda > 10$), the error in the phase velocity is approximately $(\pi^2/6)(1 - S^2)/N_\lambda^2$, so halving the cell size reduces the error by a factor of four. In theory, any desired accuracy can be obtained by increasing N_λ .

Ideally, given an electromagnetics problem, we would like to be able to estimate accurately the computational resources (computer memory and execution time) required to solve the problem using the FDTD method. Of course, this estimate is highly dependent on the problem and the computer being used. In practice, the estimate is usually made by comparing the requirements for the problem under consideration with those of a “benchmark problem” that has been run using a particular FDTD code on a particular computer. Even though the specific requirements for the algorithm are computer dependent, general rules for the scaling of the required memory and execution time with cell size are easily obtained.

Consider a computational volume that is a cube composed of cubical FDTD cells, then the total number of cells is $N = N_x^3$. Because only the most recent values of the electric and magnetic fields are needed at each step of the algorithm, the total storage required scales as N or N_x^3 , i.e., as the third power of the number of cells along the edge

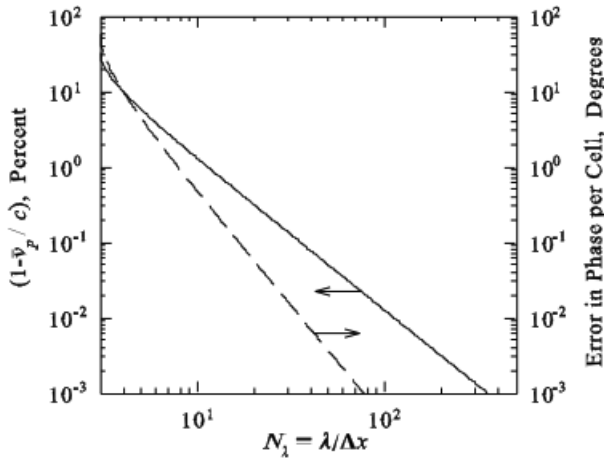


Figure A.2: Numerical dispersion as a function of the number of cells per wavelength, N_λ , for a time-harmonic plane wave propagating along one of the axes of an FDTD lattice of cubical cells. Solid line, the relative error in the phase velocity in percent. Dashed line, the error in the phase per cell in degrees. $S = 0.5$.

of the cubical volume. The simulation must be run for a time roughly proportional to that required for light to cross the volume, $t_{\max} \propto N_x \Delta x / c$. Thus, the number of time steps required is $N_t = t_{\max} / \Delta t \propto N_x / D \propto N_x$. Now the execution time is proportional to the product of the number of cells with the number of times the cells must be updated: $N \times N_t \propto N_x^4$. The execution time scales as the fourth power of the number of cells along the edge of the cubical volume. Thus, if we half the dimensions of the cells, the storage will increase by a factor of 8, and the execution time will increase by a factor of 16.

A.4 Formulation of the Antenna Problem in the FDTD Method

Antennas are customarily used in two states: transmission and reception. While the two states are related due to the reciprocity inherent in Maxwell's equations, not all quantities for one state can be obtained from the other. Thus, we must have two separate FDTD formulations for the antenna problem, one for the transmitting antenna and the other for the receiving antenna.

A.4.1 Transmitting Antenna

Figure 3(a) is a schematic drawing showing the basic elements involved in the FDTD analysis of a transmitting antenna. The figure is for a cross section through the computational volume, and the antenna is located near the center of the volume. The arrangement used to excite the antenna is shown in Figure 4(a). The antenna is connected to the source by a transmission line (waveguide) of characteristic impedance Z_0 , and the source is matched to the characteristic impedance (there is no reflection for a wave entering the source).² The specified excitation is the outward-propagating (incident) voltage wave $V_t^+(t)$ for a single mode at the reference plane in the line. Notice, at this reference plane there is also a voltage $V_t^-(t)$ associated with an inward-propagating (reflected) wave.

The finite computational volume in Figure 3(a) is surrounded by an absorbing boundary. The objective for this boundary is to reproduce at its interior surface the same conditions for the electromagnetic field that would exist if the volume were infinite. Stated differently, if we consider the electromagnetic field within the volume to be composed of a spectrum of plane waves, both outward propagating and evanescent, all of these waves should be absorbed without reflection by the boundary. At this time, the most effective absorbing boundaries are the perfectly matched layers (PMLs). Their implementation is discussed in the literature [11], [12].

The FDTD method provides the electromagnetic field for all lattice points within the finite computational volume. However, for many antenna applications, we would like to know the radiated or far-zone field, which is the field in the limit as the radial distance from the antenna becomes infinite ($r \rightarrow \infty$). This field can be obtained by applying what is known as a near-field to far-field (NFFF) transformation. For the implementation of this transformation, a closed surface S is placed around the antenna and inside the absorbing boundary. It is shown by the dashed line in Figure 3. The field (E^t and H^t) on this surface is obtained for the time period of interest, and it is used to calculate the following electric and magnetic surface current densities:

$$J_s(r', t) = \hat{n} \times H^t(r', t), \quad (\text{A.4})$$

$$M_s(r', t) = -\hat{n} \times E^t(r', t), \quad (\text{A.5})$$

Here, as shown in Figure 3(b), r' locates a point on the surface, and \hat{n} is the outward-pointing unit vector normal to the surface at that point. Outside the surface S , these currents produce the same electromagnetic field as the transmitting antenna (E^t , H^t), and inside the surface they produce a null field ($E = 0$, $H = 0$).

At the position r , the radiated or far-zone field (indicated by the additional superscript r) is obtained using these currents with a version of Huygens' principle for electromagnetic fields [8]:

$$E^{tr}(r, t) = \frac{\mu_0}{4\pi r} \iint_S \left\{ \hat{r} \times \hat{r} \times \frac{\partial}{\partial t'} [J_s(r', t')] + \frac{1}{\eta_0} \hat{r} \times \frac{\partial}{\partial t'} [M_s(r', t')] \right\}_{t'=t_r} dS', \quad (\text{A.6})$$

²Throughout the chapter we will assume that the characteristic impedance of a transmission line is real, a resistance.

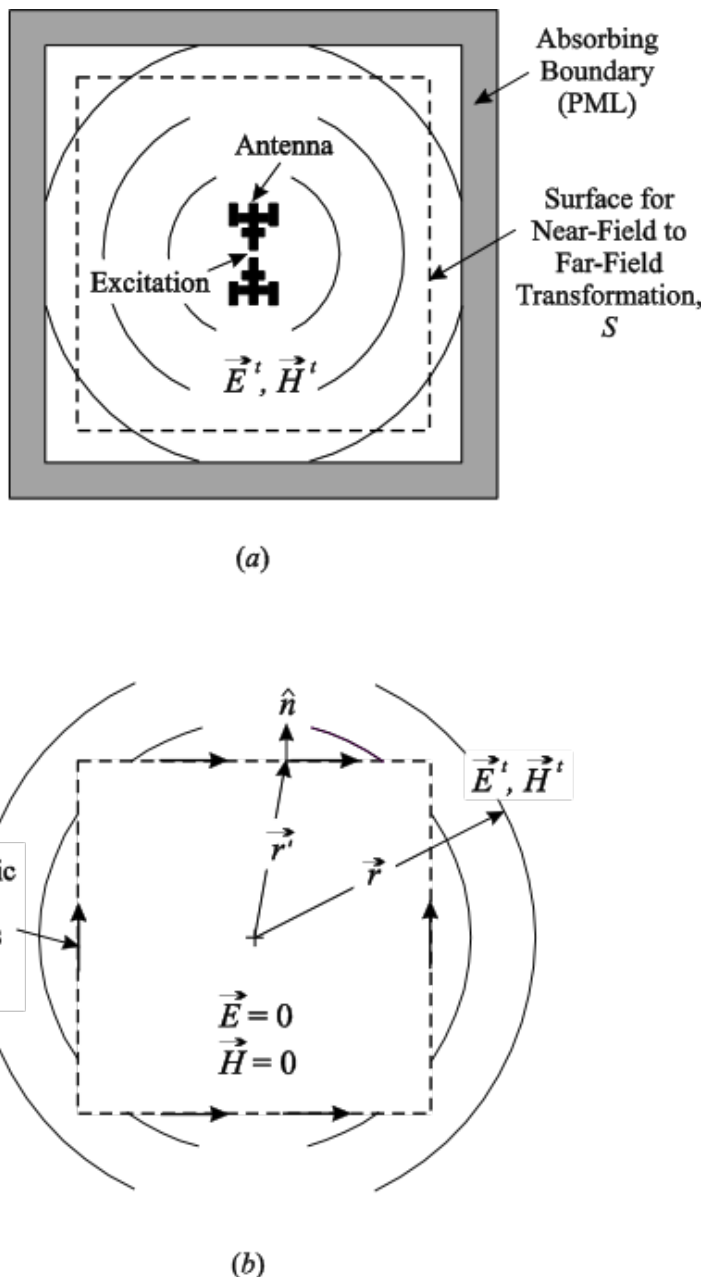


Figure A.3: (a) Schematic drawing showing the basic elements involved in the FDTD analysis of a transmitting antenna. (b) Details for the near-field to far-field transformation.

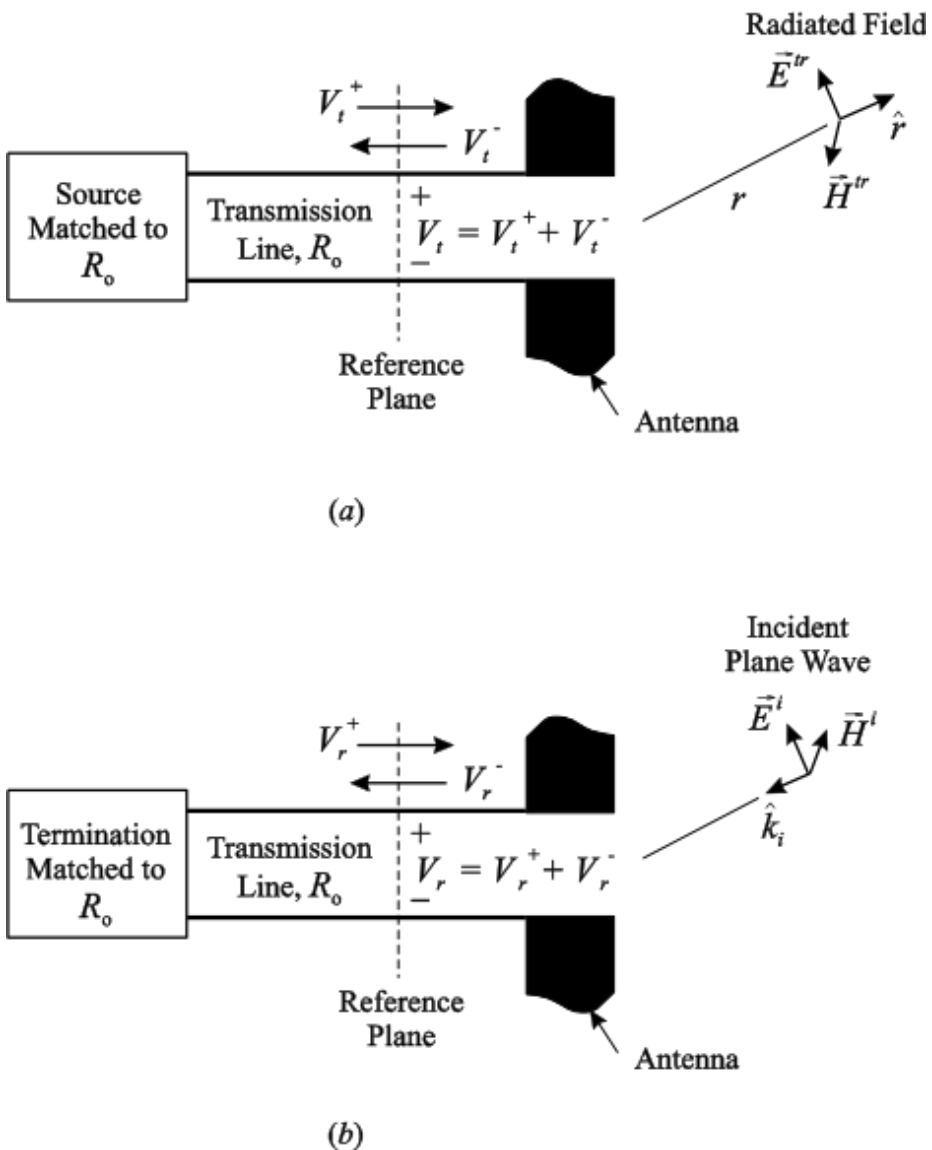


Figure A.4: The details for the feed region of (a) the transmitting antenna and (b) the receiving antenna. The characteristic impedance of the transmission line is R_o , and the source and termination are matched to this impedance

$$H^{tr}(r, t) = \frac{1}{\eta_o} \hat{r} \times E^{tr}(r, t), \quad (\text{A.7})$$

in which the retarded time is

$$t_r = t - (r - \hat{r} \cdot \vec{r}')/c \quad (\text{A.8})$$

and $\eta_o = \sqrt{\mu_o/\epsilon_o}$ is the wave impedance of free space

In some situations, we may require the near field at points that are so far from the antenna that it is impractical to extend the computational volume to include these points. We can then use a near-field to near-field (NFFN) transformation to obtain these results: The FDTD analysis is performed for a volume, such as that shown in Figure 3(a), and the field on the surface of the volume is transformed to obtain the near field outside the volume. Details for the NFFN transformation can be found in [13], [14].

A.4.2 Receiving Antenna

Figure 5(a) is a schematic drawing showing the basic elements involved in the FDTD analysis of a receiving antenna. As for the transmitting antenna, the figure is for a cross section through the computational volume, and the finite computational volume is surrounded by an absorbing boundary. The excitation for the antenna is an incident, transverse electromagnetic (TEM) plane wave propagating in the direction \hat{k}_i with the field

$$E^i(t, t), \quad H^i(r, t) = \frac{1}{\eta_o} \hat{(k)}_i \times E^i(r, t). \quad (\text{A.9})$$

Here, the vector E^i is transverse to \hat{k}_i , viz., $\hat{k}_i \cdot E^i = 0$.

The closed surface S with outward-pointing unit normal vector \hat{n} is placed around the antenna and inside the absorbing boundary. And, as shown in Figure 5(b), the following electric and magnetic surface currents densities are placed on this surface to produce the incident field (E^i, H^i) inside the surface and a null field ($E = 0, H = 0$) outside the surface:

$$J_s(r, t) = -\hat{n} \times H^i(r, t), \quad M_s(r, t) = \hat{n} \times E^i(r, t). \quad (\text{A.10})$$

For the receiving antenna, we generally want to know the voltage produced in the antenna by the incident wave, and the arrangement used to accomplish this is shown in Figure 4(b). The antenna is connected to the termination by a transmission line (waveguide) of characteristic impedance R_o , and the termination is matched to the characteristic impedance (there is no reflection for a wave entering the termination). The desired response is the inward-propagating voltage wave $V_r^-(t)$ for a single mode at the reference plane in this line.

The scattered field is the field produced by the currents induced in the antenna by the incident field. Notice from Figure 5(a) that the field inside the surface S is the total field, i.e., the sum of the incident and scattered fields ($E^r = E^i + E^s, H^r = H^i + H^s$). However, the field outside the surface, in the region between the surface and the absorbing boundary, is only the scattered field (E^s, H^s). If we are interested

in the scattering properties of the antenna, we can obtain them from knowledge of the field in this region. For example, the far-zone scattered field can be determined using a near-field to far-field transformation, as in the case for the transmitting antenna. The surface for the transformation must be placed between the surface for the plane-wave source and the absorbing boundary.

A.4.3 Reciprocity

As mentioned earlier, some quantities for the states of transmission and reception are related through reciprocity. For example, when the arrangements shown in Figure 4 are used for the source and termination, the following relationship applies [15]:

$$V_t^+(t) * V_r^-(t) = \frac{2\pi R_o}{\eta_o} \left[c \int_{t'=-\infty}^t E^i(0, t') dt' \right] \cdot * \left[r E^{tr}(-r\hat{k}_i, r + r/c) \right], \quad (\text{A.11})$$

in which $*$ indicates time convolution, and $\cdot *$ indicates the scalar product with time convolution. Here, the origin for the spherical coordinate system is centered on the antenna, as in Figure 4(a), and the incident electric field E^i is evaluated at the origin ($r = 0$) of this system. The radiated electric field E^{tr} is evaluated at the radial distance r in the direction ($-\hat{k}_i$) from which the incident field arrives and at the time $t + r/c$. Sometimes this relationship can be used to eliminate the need for analyzing one of the two states (transmission or reception) when the other is known, or it can be used for verifying results from one state with results from the other.

A.4.4 Frequency Domain

The FDTD method is inherently a time-domain technique. When quantities are needed in the frequency domain (angular frequency ω), they are obtained using the Fourier transformation (discrete), which is indicated by $V(t) \leftrightarrow V(w)$. The quantities customarily used for evaluating the performance of an antenna in the frequency domain are determined from the transformed variables. For the transmitting antenna, the voltage reflection coefficient Γ_A and input impedance Z_A are

$$\Gamma_A(\omega) = \frac{V_t^-(\omega)}{V_t^+(\omega)}, \quad (\text{A.12})$$

$$Z_A(\omega) = R_o \left[\frac{1 + \Gamma_A(\omega)}{1 - \Gamma_A(\omega)} \right], \quad (\text{A.13})$$

and the realized gain (gain including mismatch) and gain G in the direction are

$$G_{\text{Rel}}(\hat{r}, \omega) = \frac{4\pi r^2 \hat{r} \cdot \text{Re}[S_c^{tr}(r, \omega)]}{\text{Power available from source}} = \frac{4\pi R_o r^2 |E^{tr}(r, \omega)|^2}{\eta_o |V_t^+(\omega)|^2}, \quad (\text{A.14})$$

$$G_{\text{Rel}}(\hat{r}, \omega) = \frac{4\pi r^2 \hat{r} \cdot \text{Re}[S_c^{tr}(r, \omega)]}{\text{Power accepted by antenna}} = \frac{1}{1 - |\Gamma_A(\omega)|^2} G_{\text{Rel}}(\hat{r}, \omega), \quad (\text{A.15})$$

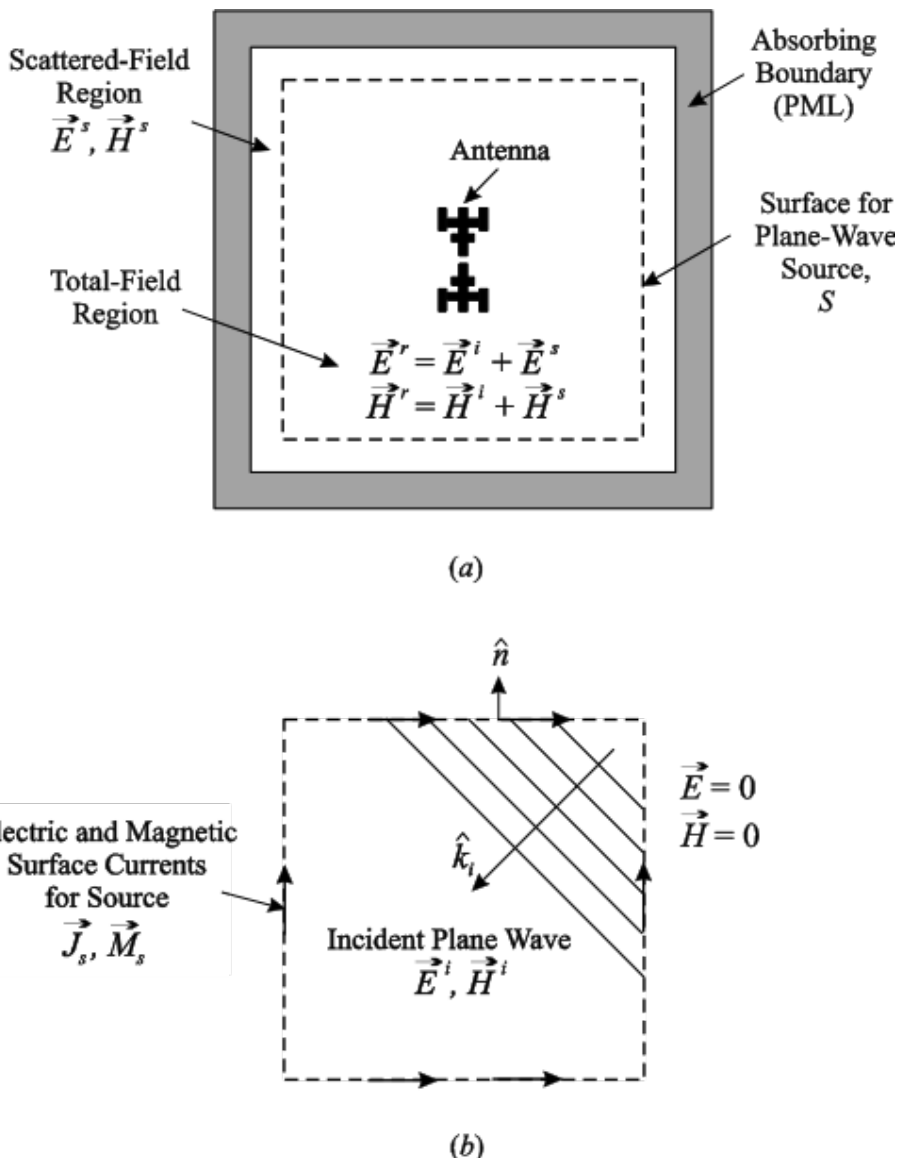


Figure A.5: (a) Schematic drawing showing the basic elements involved in the FDTD analysis of a receiving antenna. (b) Details for the plane-wave source.

in which S_c is the complex Poynting vector.

For the receiving antenna, the realized effective area $A_{\text{Rel}}(\hat{k}_i, \omega)$ and the effective area $A_e(\hat{k}_i, \omega)$ for an incident plane wave propagating in the direction \hat{k}_i are

$$A_{\text{Rel}}(\hat{k}_i, \omega) = \frac{\text{Power accepted by termination}}{\hat{k}_i \cdot \text{Re}[S_c^i(r, \omega)]} = \frac{\eta_o |V_r(r, \omega)|^2}{R_o |E_i(\omega)|^2}, \quad (\text{A.16})$$

and

$$A_e(\hat{k}_i, \omega) = \frac{\text{Power available from antenna}}{\hat{k}_i \cdot \text{Re}[S_c^i(r, \omega)]} = \frac{1}{1 - |\Gamma_A(\omega)|^2} A_{\text{Rel}}(\hat{k}_i, \omega), \quad (\text{A.17})$$

The gain and the effective area are related through reciprocity (11); for a polarization match, i.e., , we have³

$$\begin{aligned} f(t) &= \exp \left[-(t/\tau_p)^2 / 2 \right], \\ F(\omega) &= \sqrt{2\pi}\tau_p \exp \left[-(\omega\tau_p)^2 / 2 \right], \end{aligned} \quad (\text{A.18})$$

in which is the characteristic time. However, the spectrum for the Gaussian pulse contains significant low-frequency content (including dc), and this usually is not radiated by the antenna (the dc component never is). Thus, the field near the antenna may take an unacceptably long time to settle when a Gaussian pulse is used.

When we are interested in the performance of an antenna over a band of frequencies, a pulsed input signal with zero mean is useful, followed by the Fourier transform to obtain the desired frequency-domain response. For this case, the appropriate choice for the input signal might be the differentiated Gaussian pulse shown as a dashed line in Figure 6(a),

$$\begin{aligned} f(t) &= - \left(\frac{t}{\tau_p} \right) \exp \left\{ - \left[(t/\tau_p)^2 - 1 \right] / 2 \right\}, \\ F(\omega) &= j\sqrt{2\pi}\omega\tau_p^2 \exp \left\{ - \left[(\omega\tau_p)^2 - 1 \right] / 2 \right\}, \end{aligned} \quad (\text{A.19})$$

or the sinusoid of frequency amplitude modulated by a Gaussian pulse shown in Figure 6(b),

$$\begin{aligned} f(t) &= \exp \left[-(t/\tau_p)^2 / 2 \right] \sin(\omega_o t), \\ F(\omega) &= j\sqrt{2/\pi}\tau_p \end{aligned} \quad (\text{A.20})$$

³For a polarization match, the state of polarization for the incident plane wave in a particular direction (reception) is matched to the state of polarization for the radiated field in the same direction (transmission). For example, if the radiated electric field is linearly polarized, the electric field of the incident plane wave is linearly polarized and points in the same direction. If the radiated electric field is right-handed circularly polarized, the electric field of the incident plane wave is right-handed circularly polarized.

Table A.1: Characteristics for Various Input Signals

The differentiated Gaussian pulse has a rather large fractional bandwidth that is fixed; for example, the bandwidth associated with the points at which the spectrum is 10% (-20dB) of the maximum is , where $w_{pk} = 1/\tau_p$ is the frequency at the peak. The modulated sinusoid has a variable fractional bandwidth that is controlled by the relative width of the modulating pulse, $\omega_o\tau_p$; for example, the bandwidth associated with the points at which the spectrum is 10% of the maximum is $\Delta\omega/\omega_o \approx 4.29/\omega_o\tau_p$ (when $\omega_o\tau_p < 1$). For the case shown in Figure 6(b), $\omega_o\tau_p = 15$, so the fractional bandwidth is $\Delta\omega/\omega_o \approx 0.29$, which is much narrower than the fractional bandwidth for the differentiated Gaussian pulse shown in Figure 6(a).

A.5 Examples of the Use of the Method for Antenna Analysis

In the previous sections, we presented the rudiments of the FDTD method and described in general how the method is used to analyze an antenna for both transmission and reception. In this section, we will show results obtained by applying the method to analyze particular antennas. These examples were chosen to illustrate specific issues that arise and must be dealt with when applying the method.

A.5.1 Cylindrical Monopole: Theoretical Model Versus Experimental Model

The ultimate test for any physical theory is how well its predictions agree with experimental measurements, and, of course, this is the case for electromagnetic theory when applied to antennas. One of the most important factors that affect the agreement is how closely the theoretical model for the antenna agrees with the experimental model. To examine this issue we will consider the FDTD analysis of the cylindrical monopole, the image equivalent of the cylindrical dipole, which is arguably the most fundamental antenna.

The monopole antenna, shown in Figure 7(a), is formed by extending the metallic center conductor of a coaxial line the distance h above an infinite metallic image plane [2], [8]. The dimensions of the transmission line, inner conductor radius a and outer conductor radius b , are chosen so that only the TEM mode propagates in the line for the signals of interest. The FDTD model for the transmitting monopole is shown in Figure 7(b). All of the conductors in the model are perfect (perfect electric conductors, PECs), and the structure is surrounded by a PML, not shown in the figure [16]. Because of the rotational symmetry of the structure and the excitation, a two-dimensional cylindrical lattice (ρ, z) with the spatial increments $\Delta\rho$ and Δz is used in the FDTD analysis. A “one-way source” excites the coaxial line. This consists of the electric and magnetic surface currents

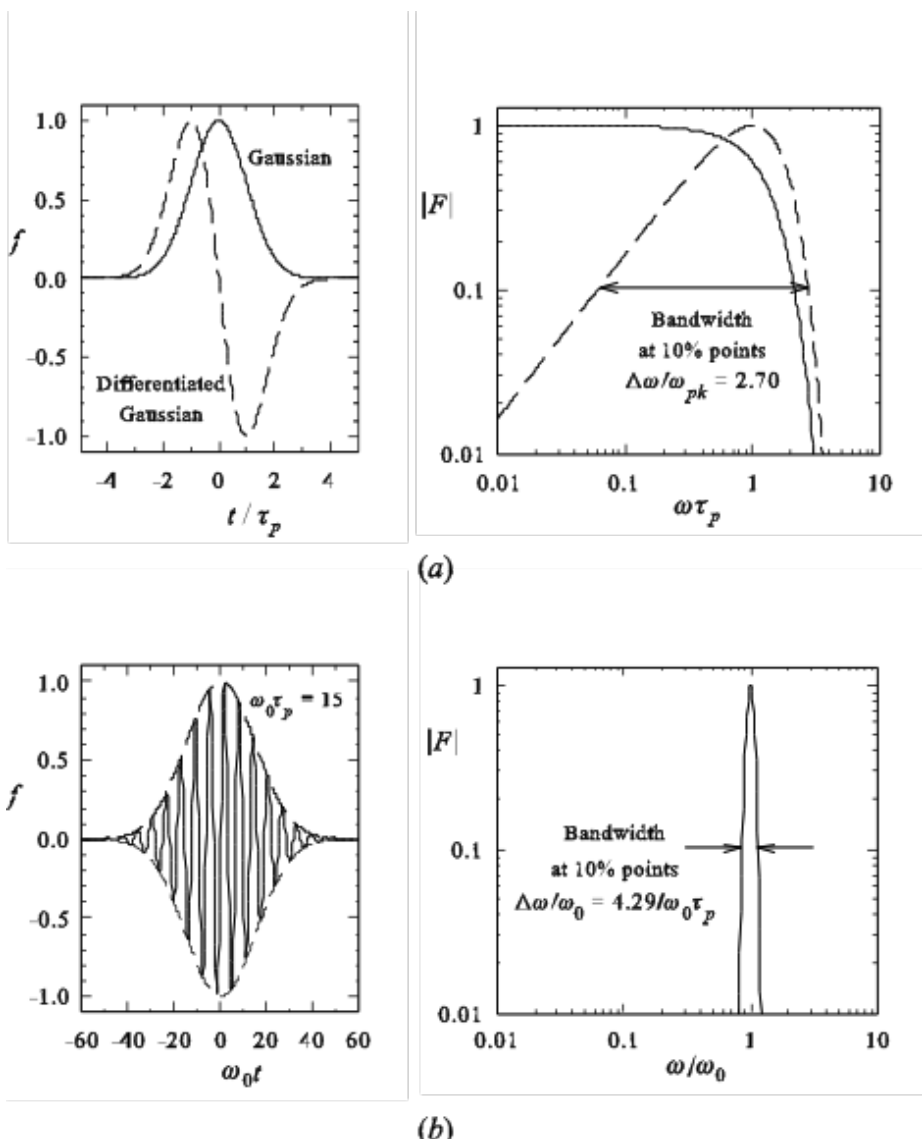


Figure A.6: (a) The Gaussian pulse (solid line) and the differentiated Gaussian pulse (dashed line) and the magnitude of their Fourier transforms. (b) The sinusoid of frequency amplitude modulated by a Gaussian pulse and the magnitude of its Fourier transform. All waveforms are normalized to have a maximum value of 1.0.

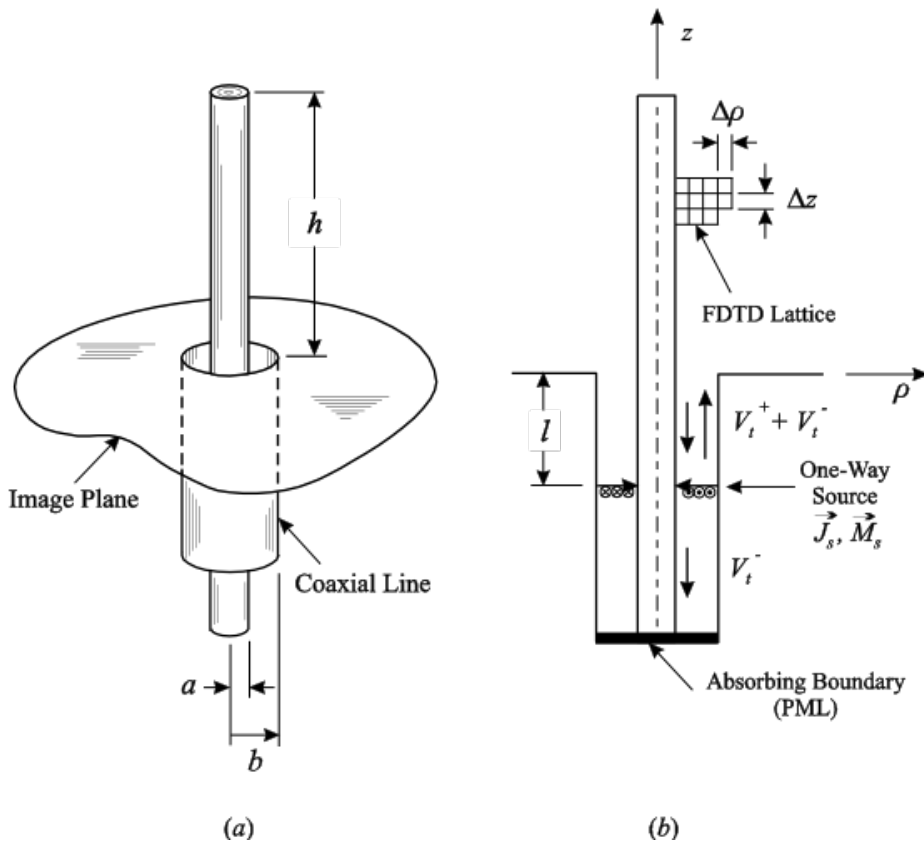


Figure A.7: (a) Cylindrical monopole antenna fed through an image plane from a coaxial transmission line. (b) FDTD model for the cylindrical monopole antenna. The PML that surrounds the computational space is not shown.

$$J_s(\rho, t) = -\frac{V_t^+(t)}{2\pi R_o \rho} \hat{\rho}, M_s(\rho, t) = -\frac{\eta_o V_t^+(t)}{2\pi R_o \rho} \hat{\phi} \quad (\text{A.21})$$

on the plane $z = -l$ that produce the incident TEM voltage wave, V_t^+ , above the source and a null field below the source. An absorbing boundary is placed at the bottom of the line. With this configuration, only the reflected TEM voltage wave, V_t^- , appears below the source, so it is easily determined. Notice the similarity of this arrangement to the plane wave source used with the receiving/scattering antenna in Figure 5.

Figure 8 is a comparison of results from the FDTD simulation (solid line) with measurements (dots) made on an experimental model corresponding to the geometry in Figure 7(a). The height of the monopole is $h = 5.0$ cm, and the dimensions of the coaxial line (precision line with APC-7 connector) are $a = 1.52$ mm, $b = 3.5$ mm, which gives a characteristic impedance of $R_o = (\eta_o/2\pi)\ln(b/a) = 50\Omega$. The excitation V_t^+ is a unit-amplitude Gaussian pulse in time (19), with the characteristic time $\tau_p = 0.161\tau_a$, where $\tau_{a,u} = h/c$ is the time for light to travel the length of the monopole. In the experiment the reflections from the edges of the finite sized image plane were windowed out in time.

Figure 8(a) is for the reflected voltage, V_t^- , in the transmission line, and Figure 8(b) is for the electric field on the image plane at the radial distance $\rho/h = 12.7$, both are shown as a function of the normalized time t/τ_a . In Figure 8(a), we see the initial reflection of the incident pulse from the drive point (A), followed by its initial reflection from the open end of the monopole (B). As expected, these events are separated by roughly the time for light to make a round trip on the monopole, $(t_B - t_A)/\tau_a \approx 2$. Additional reflections of decreased amplitude occur each time the pulse encounters the drive point and the open end. In Figure 8(b), we see that radiation occurs each time the pulse encounters the drive point or the open end of the monopole. As expected, the initial radiation from the drive point (A) is separated from the initial radiation from the open end of the monopole (B) by roughly the time for light to travel the length of the monopole, $(t_B - t_A)/\tau_a \approx 1$. The agreement of the theoretical and measured results is seen to be very good.

The FDTD method inherently provides information about the electromagnetic field within the computational volume over the entire period of the simulation. Only a small fraction of this information is used when investigating conventional antenna parameters, such as the results shown in Figure 8. Sometimes this additional information can be used to perform “numerical experiments” that improve our understanding of the radiation process for the antenna. This is illustrated in Figure 9, where we show the instantaneous Poynting vector in the region surrounding the monopole [17]. On the right-hand side of these figures, the logarithm of the magnitude of the Poynting vector, $|S|$, is plotted on a color scale. The intensity of the field increases as the hue goes from blue to red, and the range for the values of $|S|$ displayed is $10^4 : 1$. On the left-hand side of these figures, the arrows indicate the direction of the Poynting vector, and the length of an arrow is proportional to the logarithm of $|S|$. The excitation is a Gaussian voltage pulse with $\tau_p = 0.0537\tau_a$. For this value of τ_p , about three non-overlapping pulses fit along the length of the monopole, so the reflections associated with different points are separated and easily identified.

In Figure 9(a), the pulse has just left the drive point and is traveling up the monopole.

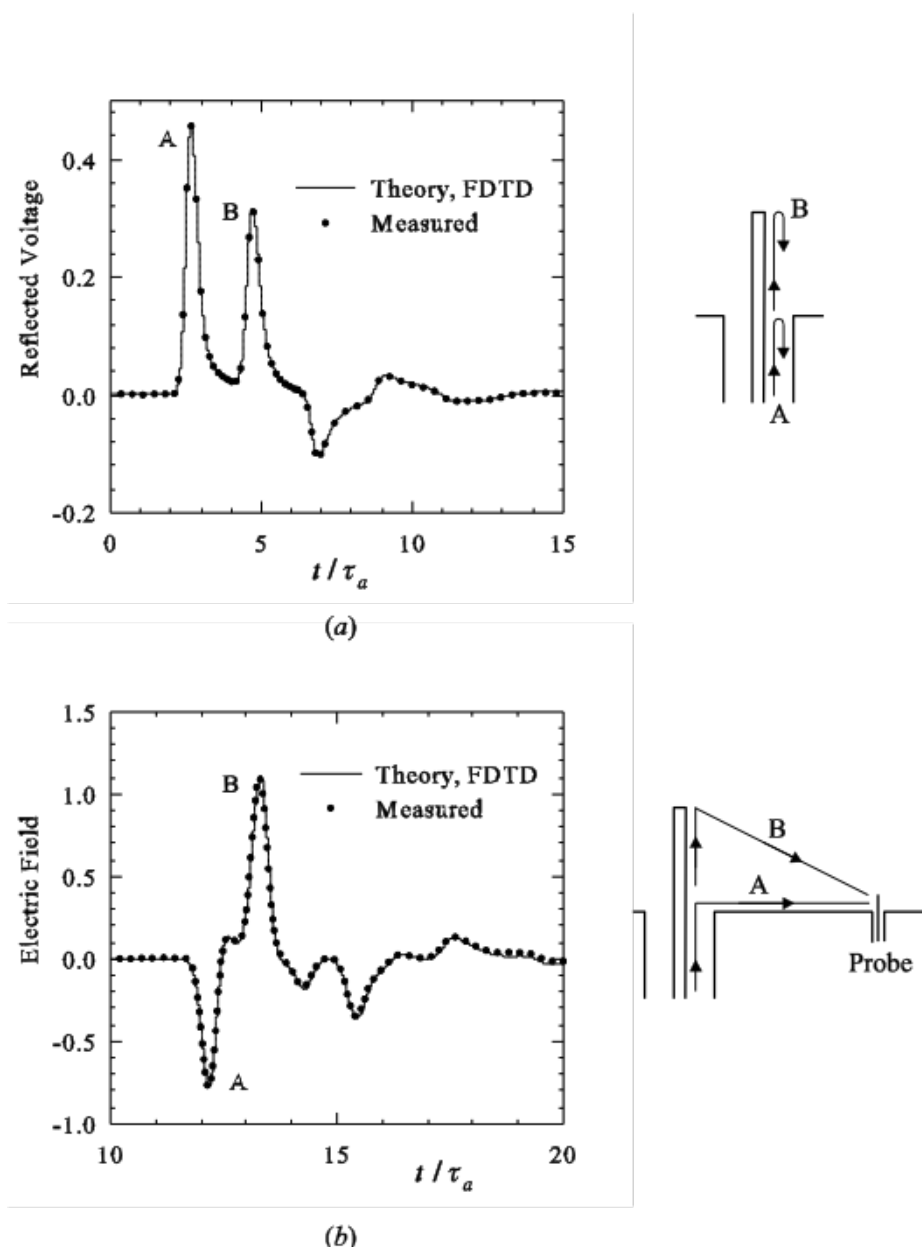


Figure A.8: Comparision of theoretical and measured results for the cylindrical monopole antenna. (a) Reflected voltage in the coaxial line. (b) Electric field on the image plane at $\rho/h = 12.7$.

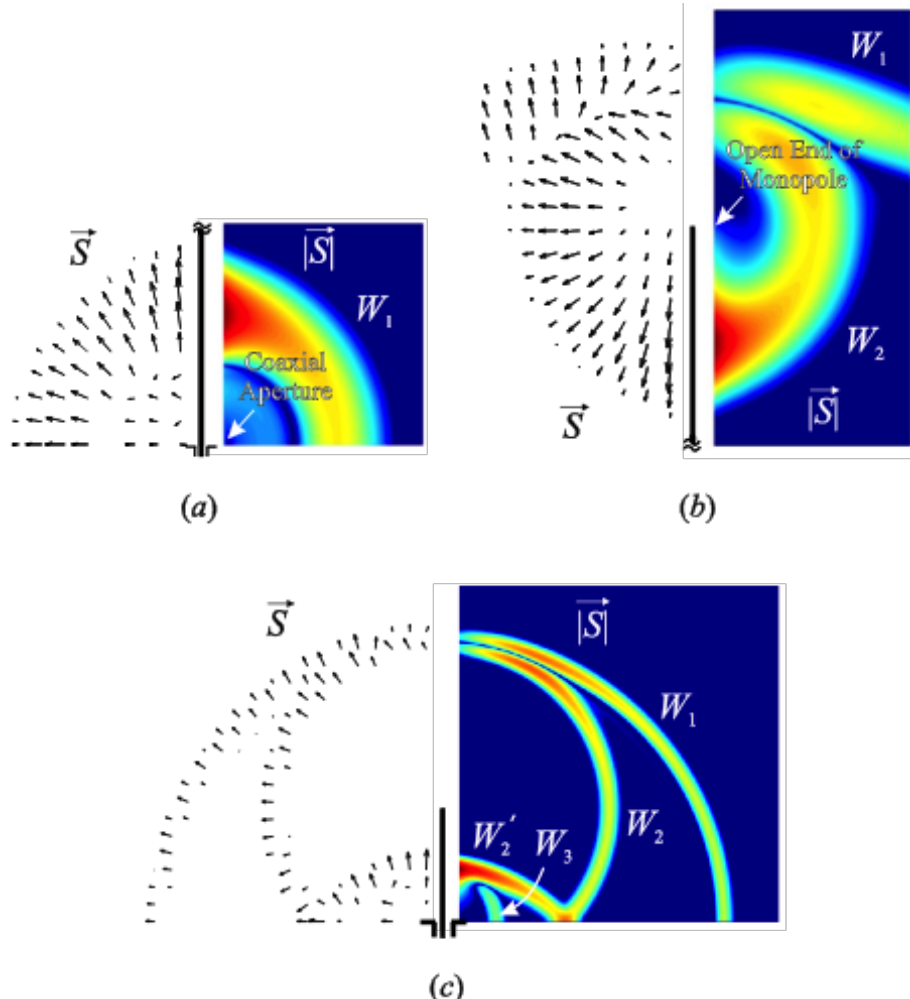


Figure A.9: Three snapshots in time showing the magnitude (right) and direction (left) of the Poynting vector surrounding the cylindrical monopole antenna: (a) near the coaxial aperture at time t_1 , (b) near the open end of the monopole at time t_2 , and (c) around the whole structure at time t_3 . Logarithmic scaling is used for both plots. Notice that (a) and (b) only show a portion of the monopole. (After Smith and Hertel [17], 2001 IEEE.)

A spherical wavefront W_1 centered on the drive point has formed, and it is attached to the outward propagating pulses of charge/current on the monopole and image plane. In Figure 9(b), the pulse has encountered the open end of the monopole, and it is traveling back down the monopole. A second spherical wavefront W_2 centered on the open end has formed, and it connects the inward propagating pulse of charge/current on the monopole with the wavefront W_1 . Additional wavefronts, W'_2 , W_3 , etc., shown in Figure 9(c), are produced each time the pulse encounters the drive point and the open end. All of these spherical wavefronts travel outward at the speed of light. The Poynting vectors are seen to be predominantly normal to the wavefronts, which indicates that energy is being transported away from both the drive point and the open end.

The input impedance or admittance $Y_A(\omega) = 1/Z_A(\omega) = G_A(\omega) + jB_A(\omega)$ of the monopole antenna is a useful parameter for practical applications, and it is also a sensitive measure of the accuracy of any theoretical model. It is easily calculated from the FDTD time-domain results using (12) and (13). In Figure 10 the input admittance is graphed as a function of frequency for a monopole with the same dimensions as used for Figure 8 [18]. FDTD results (lines) for three different levels of discretization (A, B, C) are compared with measurements (dots). The parameters for the three levels of discretization are given in Table 2. In this graph we observe the convergence of the FDTD method. Consider the input susceptance, ; the result for discretization A is slightly displaced from the measured values, while the results for discretizations B and C are essentially the same as the measured values. Hence, we can conclude that, for practical purposes, the FDTD results for the input admittance have converged to the measured values at discretization B, which is for four FDTD cells across the gap in the coaxial line or 101 cell along the length of the monopole. We should mention that the dimensions of the FDTD cell for this example had to be chosen so that an integral number of cells fit along the dimensions of the antenna, so the cells are not perfectly square. Notice that discretization B corresponds to 135 cells per wavelength at the highest frequency ($f = 4.5$ GHz) and a relative error in the phase velocity ((3) and Figure 2 for $S = 0.5$) of only $6.77 \times 10^{-3}\%$. For this example, it is not the error in the phase velocity that determines the accuracy of the solution. The fine details of the structure must be accurately modeled, and this requires cells that are much smaller than needed for a small error in the phase velocity.

The very good agreement of the theoretical results with the measurements evident in Figs. 8 and 10 is a consequence of the close match of the theoretical model for the monopole, Figure 7(b), to the experimental model, Figure 7(a). In some cases, additional constraints on the analysis require a reduction in the fidelity of the FDTD model, and such good agreement cannot be expected. To illustrate the effect a reduction in the fidelity of the model can have on the accuracy of the results, we will examine some common simplifications used for the FDTD model of the monopole.

For the models shown in Figure 11, the cylindrical conductor of the monopole has been replaced by an equivalent square conductor of side [19]. Thus, the monopole now can be analyzed using the conventional three-dimensional rectangular FDTD lattice rather than the two-dimensional cylindrical lattice of Figure 7(b).

The excitation for the monopole has also been changed from that in Fig 7(b). For the model in Figure 11(a), the so called “hard source” is used. This specifies the total voltage $V_t = V_t^+ + V_t^-$ across the gap of length l_g at the base of the monopole. And

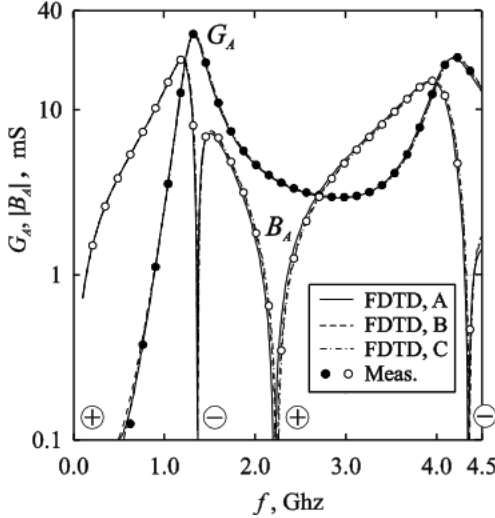


Figure A.10: Comparison of theoretical and measured results for the input admittance of the cylindrical monopole antenna. Results are shown for three levels of discretization (A, B, C) in the FDTD method. (After Hertel and Smith [18], 2003 IEEE.)

for the model in Figure 11(b), a virtual one-dimensional transmission line is connected across the gap at the base of the monopole [20]. This transmission line contains the same elements as the transmission line in Figure 7(b), in particular, a one-way source that specifies the incident voltage V_t^+ . We refer to this line as virtual because it does not appear in the FDTD lattice surrounding the monopole. It is in a different location and coupled to the monopole through the voltage and current at its terminals. The hard source, while simple to implement, suffers from two drawbacks not present with the transmission line feed. There is no damping in the hard source, unless resistance is added, so the currents, etc. on the antenna can ring for a long period of time. And the total voltage is specified, so the reflected voltage, a quantity often of interest in time-domain simulations, is not readily available.

In Figure 12, FDTD results for the input admittance for both models in Figure 11 are compared with measurements made with the configuration shown in Figure 7(b) [18]. The level of discretization used is such that the simulations have converged for practical purposes. The theoretical results for the input conductance, G_A , for both models are in very good agreement with the measurements; however, those for the input susceptance, B_A , differ from the measurements, particularly for the hard source (dashed line). The difference in susceptance is a consequence of the geometry for the simplified models not accurately representing the experimental model, Figure 7(a), in the vicinity of the drive point (the aperture of the coaxial line). The susceptance for the simplified models can be brought into better agreement with the measured results by adding a small capacitance in parallel with the terminals of the monopole [18].

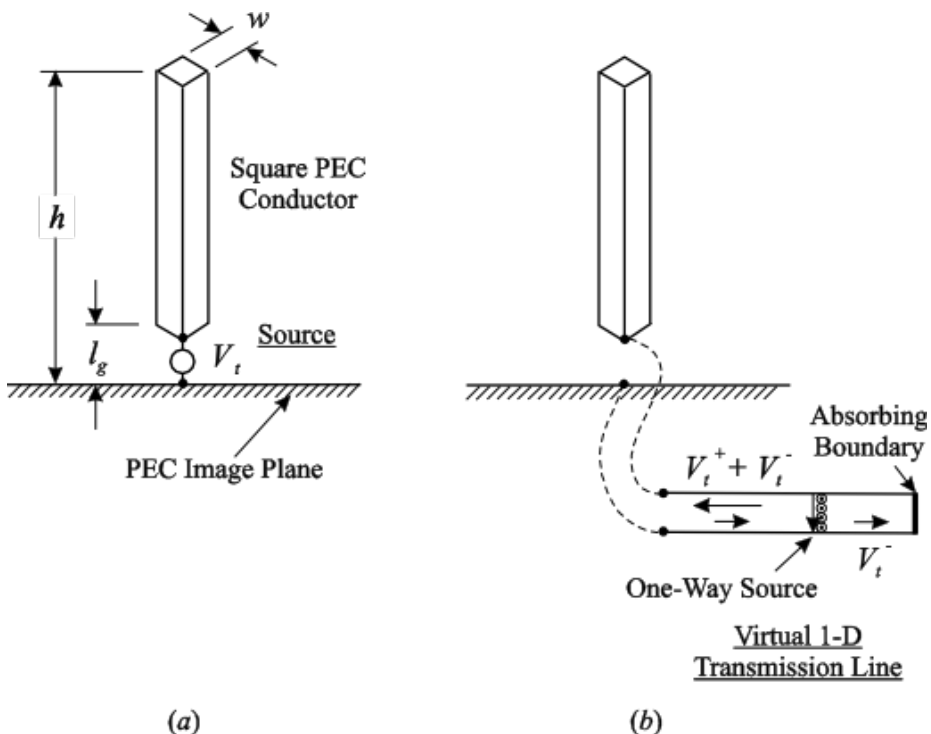


Figure A.11: Simplified models for the cylindrical monopole antenna. (a) Model incorporating a ?hard source.? (b) Model incorporating a virtual one-dimensional transmission line. The monopole conductor has a square cross section in both models.

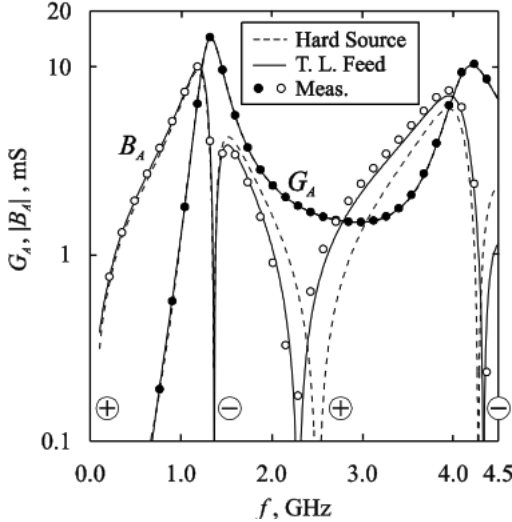


Figure A.12: Comparison of theoretical and measured results for the input admittance of the cylindrical monopole antenna. Results are shown for the two simplified FDTD models. (After Hertel and Smith [18], 2003 IEEE.)

A.5.2 Metallic Horns and Spirals: Stair-Stepped Surfaces

For the monopole antennas discussed in the previous section, the boundaries of the FDTD cells as well as the boundaries of all material regions (PECs) coincided with surfaces of constant coordinate. Thus, the boundaries of material regions never passed obliquely through an FDTD cell. This is a special case that is not encountered for most antennas.

Figure 13(a) illustrates the more general case. It shows the cross section of a PEC object with the rectangular FDTD lattice superimposed. The curved surface of the object does not coincide with any of the lattice lines. Note, for the computation we only need to know the field in the FDTD cells that are exterior to the PEC, because both E and H are zero inside the PEC. There are different approaches that can be used for this case. One approach is to introduce non-rectangular FDTD cells that conform to the surface of the object; these cells could be used throughout the computational volume or just adjacent to the object [21]-[23]. Another much simpler approach, shown in Figure 13(b), is to deform the curved surface of the object so that it conforms to the rectangular FDTD lattice. The surface of the object is said to be replaced by a “stair-stepped” or “staircase” approximation. The stair-stepped approximation will introduce an error, and often the error can be made negligible by simply choosing the size of the staircase to be small compared to the physical dimensions of the object [24], [25]. The stair-stepped approximation is commonly used, and it is the only approach we will consider in this introductory treatment.

We will now consider two practical antennas for which the stair-stepped approximation was used in modeling the structure in the FDTD analysis. As these examples

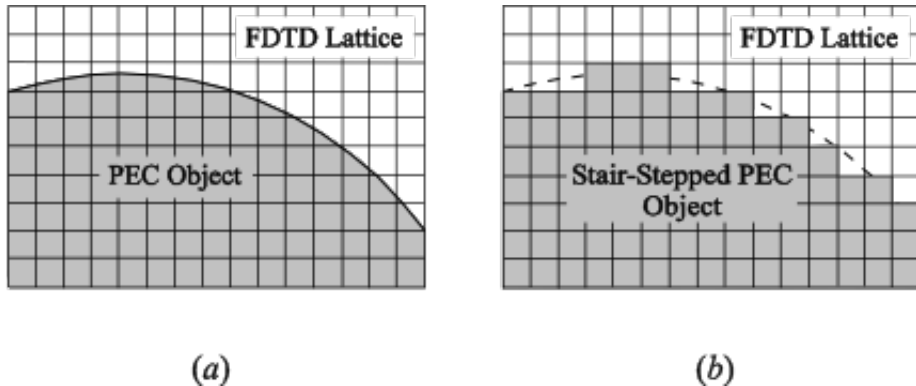


Figure A.13: (a) Rectangular FDTD lattice superimposed on the cross section of an object that is a perfect electric conductor (PEC). (b) The surface of the object has been deformed to conform to the rectangular lattice; the surface of the object has been replaced by a stair-stepped approximation.

will show, when properly used, the approximation can yield results that are in good agreement with experimental measurements. The first example is the metallic, pyramidal horn shown in Figure 14 (Flann Microwave Instruments Ltd. Model 1624-20). Antennas like this are used in many microwave applications, and sometimes they serve as gain standards (standard gain horns). The small drawings at the bottom of the figure show the lengths and angles that describe this particular horn antenna: $a = 10.95$ cm, $b = 7.85$ cm, $D = 2.284$ cm, $l_w = 5.08$ cm, $\alpha = 10.74^\circ$, and $\beta = 8.508^\circ$. The waveguide feeding the horn is type WR-90 (X-Band, with the operational bandwidth 8.2 GHz ? 12.4 GHz).

In the FDTD model, the cubical cells have the side length $\Delta x = 0.635$ mm, and the perfectly-conducting walls are plates two cells thick. The inset shows the faces of the individual cells that model the bottom wall of the horn; the cells are shown seven times actual size. The slanted sides of the horn are stair stepped, as indicated in the figure, with a “tread length-to-rise” of approximately six cells to one. The horn is fed by a probe inserted into the section of rectangular waveguide, and the incident and reflected voltages in a one-dimensional transmission line ($R_o = 50\Omega$) connected to the probe are used in the analysis.

The structure is symmetrical about the x-z plane, and this symmetry was used in the analysis to reduce the size of the computational volume, which was 519 x 116 x 183 cells. The sides of the antenna were 20 cells from the PML absorbing boundary (10 cells thick), except the front side (radiating aperture), which was 40 cells from the absorbing boundary.

The pyramidal horn was first analyzed as a transmitting antenna. The excitation in the transmission line, $V_t^+(t)$, was a differentiated Gaussian pulse (20) with the characteristic time $\tau_p = 1.59 \times 10^{-11}$ s. This pulse has significant energy over the operational bandwidth of the horn: 8.2 - 12.4 GHz. The peak of the spectrum for the pulse is at 10.0 GHz, and the spectrum drops to 10% of the peak at 600 MHz and 27.6 GHz.

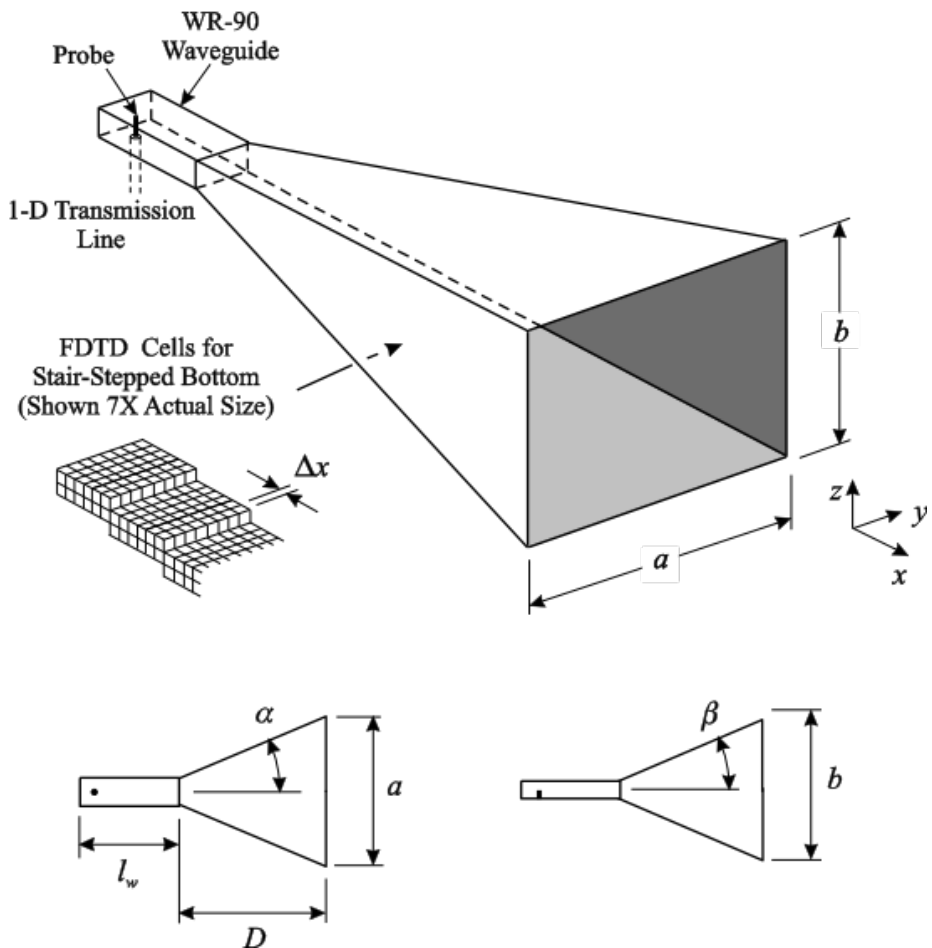


Figure A.14: Schematic drawing for the pyramidal horn antenna. The inset shows the FDTD cells used to model the bottom of the horn.

At the highest frequency (shortest wavelength) within the operational bandwidth of the horn we have $\Delta x = 0.0226\lambda$, which corresponds roughly to 38 cells per wavelength. From this result, we can estimate the numerical dispersion using Figure 2 or equation (3). The relative error in the phase velocity is about 0.1%, which is equivalent to 8.1×10^{-3} degrees of phase error per cell, or a total error of 4.2 degrees of phase error for propagation across the longest side of the computational volume.

Figure 15 is a comparison of the FDTD results (solid line) for this antenna with measurements (dots). The measured data were kindly supplied by Dr. David G. Gentle of the National Physical Laboratory, Teddington, Middlesex, U.K. Figures 15(a) and 15(b) show the E- and H-plane field patterns at the frequency 10 GHz, and Figure 15(c) shows the gain on boresite as a function of frequency. The results from the FDTD calculations are seen to be in very good agreement with the measurements. The small differences that do exist in the H-plane field pattern are for angles at which the field is very weak, 50 dB below the peak. We note that the precise details of the probe feeding the waveguide in the FDTD model do not affect the calculation of the gain (15) of the horn. This would not be the case if the realized gain (14) (gain including mismatch) were determined.

The pyramidal horn was also analyzed as a receiving antenna. For this case, a plane wave was incident from the boresite direction ($\hat{k}_i = -\hat{x}$) with the electric field pointing in the z direction. The incident electric was a differentiated Gaussian pulse in time (20) with the same characteristic time as used for the transmitting case, $\tau_p = 1.59 \times 10^{-11} s$. The effective area obtained from the receiving analysis was converted to a gain using equation (18), and the result is shown as a dashed line in Figure 15(c). As expected from reciprocity, the results from the two FDTD calculations (transmitting and receiving) are nearly identical.

The FDTD method provides the field throughout the computational volume, and it can be used to construct graphical results that illustrate the process of radiation for the transmitting horn antenna. For such illustrations, we want an excitation whose spectrum lies within the operational bandwidth of the antenna. Frequencies outside of this band will either be cutoff in the waveguide or overmode the waveguide. A good choice for the voltage $V_t^+(t)$ is the sinusoid of frequency ω_o amplitude modulated by a Gaussian pulse, i.e., (21) shown in Figure 6(b). With $f_o = \omega_o/2\pi = 10.0$ GHz, and $\tau_p = 7.96 \times 10^{-11} s$, the spectrum for this signal is 10% of its peak at $f = 5.7$ GHz and $f = 14.3$ GHz.

Figure 16 shows three gray scale plots for the magnitude of the electric field on the x-z plane of the transmitting antenna. In Figure 16(a) the pulse has entered the horn from the waveguide, but it has not reached the aperture. The spacing between the white lines (nulls) roughly corresponds to one half of a guide wavelength. Notice that this spacing decreases on going from the throat of the horn towards the aperture. In the rectangular waveguide, the guide wavelength is about 1.3 times the free-space wavelength, whereas at the aperture of the horn it is closer to the free-space wavelength. Figure 16(b) is for a time when the pulse has reached the aperture. Notice that the white lines in the horn near the aperture are distorted; there is a small segment that is concave to the right. This is caused by the reflection from the aperture that is traveling back toward the throat of the horn. Directly in front of the aperture, the radiated wave is roughly planar. In Figure 16(c), the field has propagated away from the horn, and

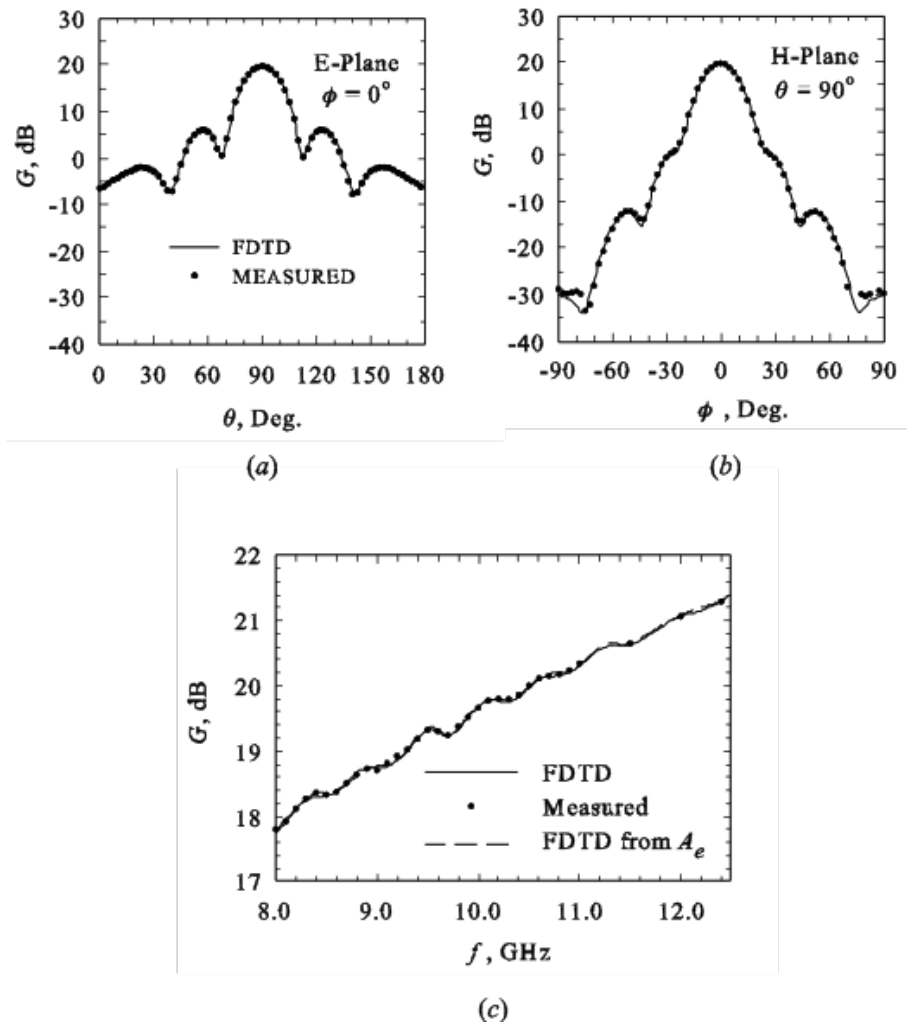


Figure A.15: Comparison of theoretical and measured results for the pyramidal horn antenna. (a) E-plane pattern and (b) H-plane pattern at 10 GHz. (c) Boresite gain versus frequency.

a spherical wavefront has formed that is approximately centered on the aperture. The change in the shade of gray in going around the antenna (dark in front to light in back) clearly shows a large “front-to-back ratio” for the horn. In the forward direction, minima appear along the wavefront, and these minima will define the main beam in the far zone. Back in the horn, the field has several minima and maxima across its width. They indicate the presence of higher order modes that were excited when the initial pulse encountered the aperture.

The second example we will consider is the two-arm, conical spiral antenna shown in Figure 17 [26]. It is used in applications that require an antenna to radiate circular polarization over a broad bandwidth. This antenna is formed by winding two metallic strips around the surface of a truncated cone. The angles and dimensions for the particular antenna we will consider are $d = 1.9$ cm, $D = 15.2$ cm, $\theta_o = 7.5^\circ$, $\alpha = 75^\circ$, and $\delta = 90^\circ$. It is designed to have constant gain and input impedance ($Z_A \approx 100\Omega$) over an operational bandwidth extending from $f_{\min} = 0.5$ GHz to $f_{\max} = 3.3$ GHz.

In the FDTD model, the arms of the spiral are formed by making selected faces of the cubical cells ($\Delta x = 0.8$ mm) PEC. The result is the stair-stepped approximation in Figure 18. For clarity, only the lower 10% of the antenna is shown in the figure. The spiral is fed by a one-dimensional transmission line ($R_o = 100\Omega$) connected at the bottom of the antenna; the same arrangement as used with the monopole antenna in Figure 11(b). The excitation in the transmission line, $V_t^+(t)$, is a differentiated Gaussian pulse (20), whose spectrum is centered on the operational bandwidth of the antenna.

The computational volume was 691 x 240 x 240 cells, with the sides of the antenna 15 cells from the PML absorbing boundary (10 cells thick), except the bottom side (main direction for radiation), which was 30 cells from the absorbing boundary. At the highest frequency (shortest wavelength) within the operational bandwidth of the horn we have $\Delta x = 0.0093\lambda$, which corresponds roughly to 107 cells per wavelength. From this result, we can estimate the numerical dispersion using Figure 2 or equation (3). The relative error in the phase velocity is about 0.01%, which is equivalent to 3.6×10^{-4} degrees of phase error per cell, or a total error of 0.25 degrees of phase error for propagation across the longest side of the computational volume. As with the earlier case of the monopole antenna, it is not the error in the phase velocity that determines the accuracy of the solution but the degree to which the fine details of the structure are modeled.

Figure 19 is a comparison of the FDTD results (solid line) for this antenna with measurements (dashed line). Figure 19(a) shows the magnitude of the reflection coefficient at the terminals of the antenna, and Figure 19(b) shows the realized gain (14) at boresite ($-\hat{z}$ direction) as a function of frequency. The results from the FDTD calculations are seen to be in fairly good agreement with the measurements. The differences that do exist are most likely caused by elements in the experimental model that were not included in the theoretical model. In the experimental model, the metallic arms were on a very thin dielectric substrate (Kapton, thickness 0.051 mm), which was not included in the theoretical model. In addition, the terminal measurements were made through a balun, and the imperfections in the balun were not taken into account.

The FDTD method provides detailed information about the electromagnetic field surrounding the spiral, and it can be used to graphically illustrate how energy is radiated from this structure [27]. Figure 20 shows three gray scale plots of the magnitude of

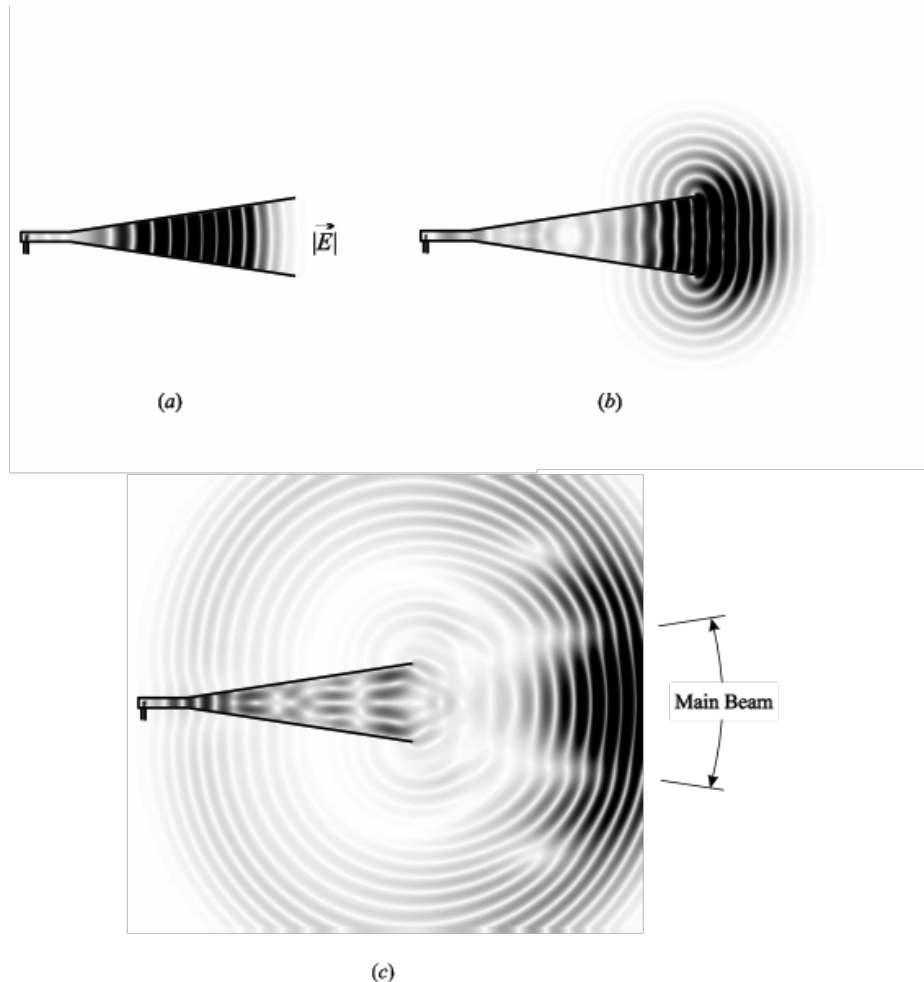


Figure A.16: Gray scale plots for the magnitude of the electric field on the vertical symmetry plane of the transmitting horn antenna. The excitation is a sinusoid amplitude modulated by a Gaussian pulse.

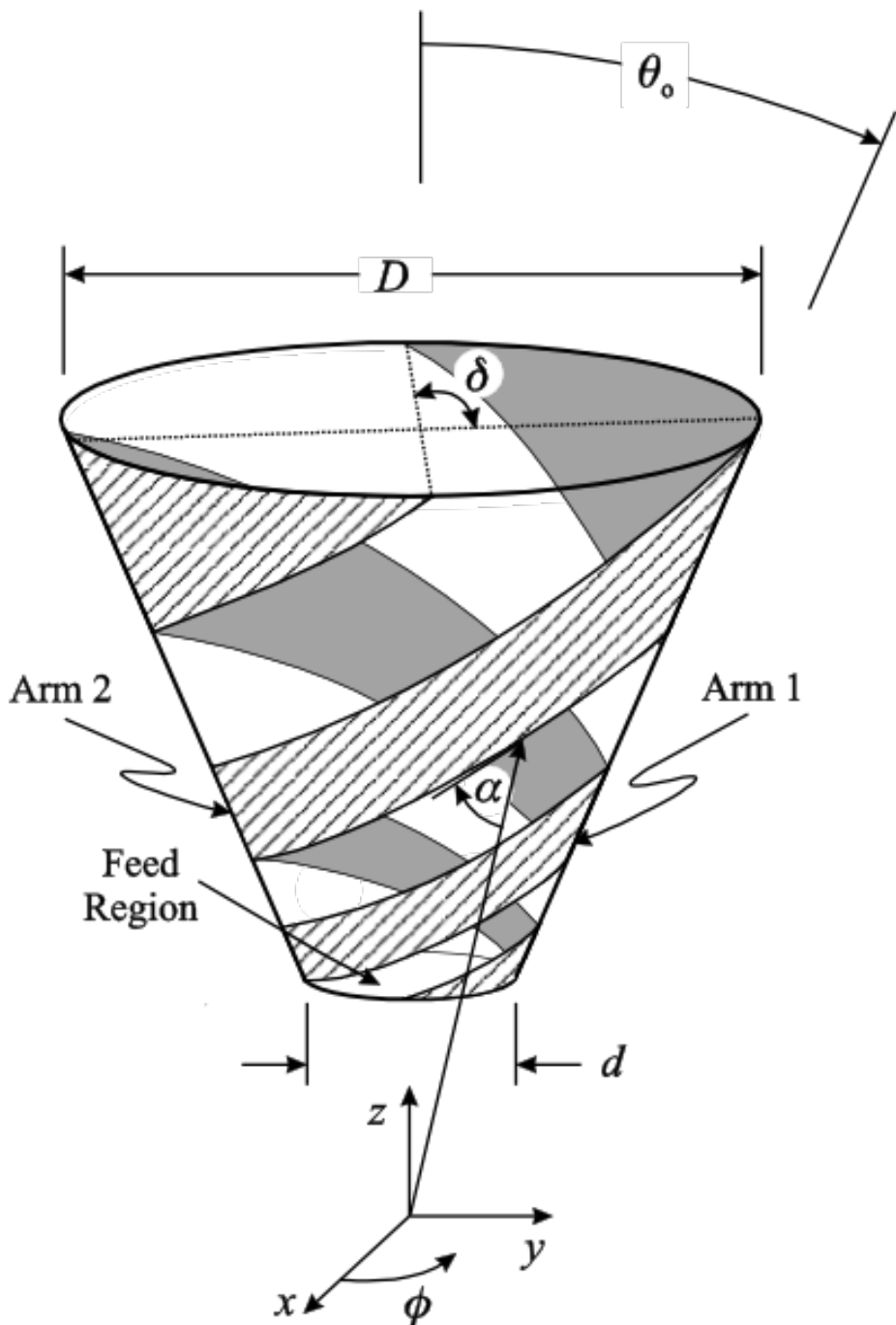


Figure A.17: Geometry for the two-arm conical spiral antenna. (After Hertel and Smith [26], 2002 IEEE.)

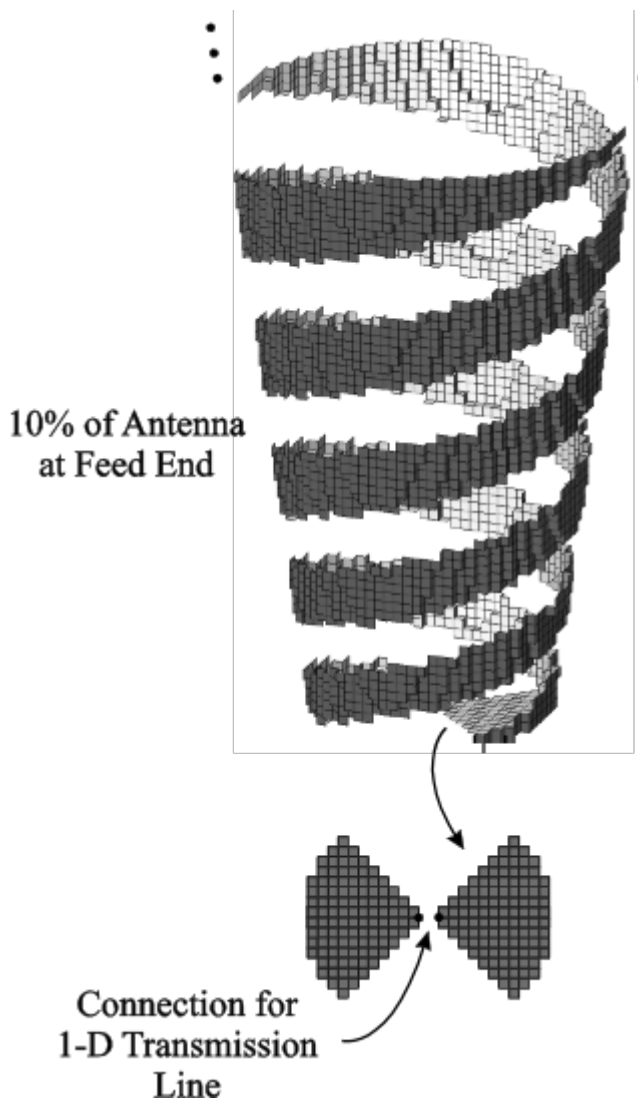


Figure A.18: Schematic drawing showing the arrangement of FDTD cells used to model the conical spiral antenna. For clarity, only the lower 10% of the antenna is shown. (After Hertel and Smith [26], 2002 IEEE.)

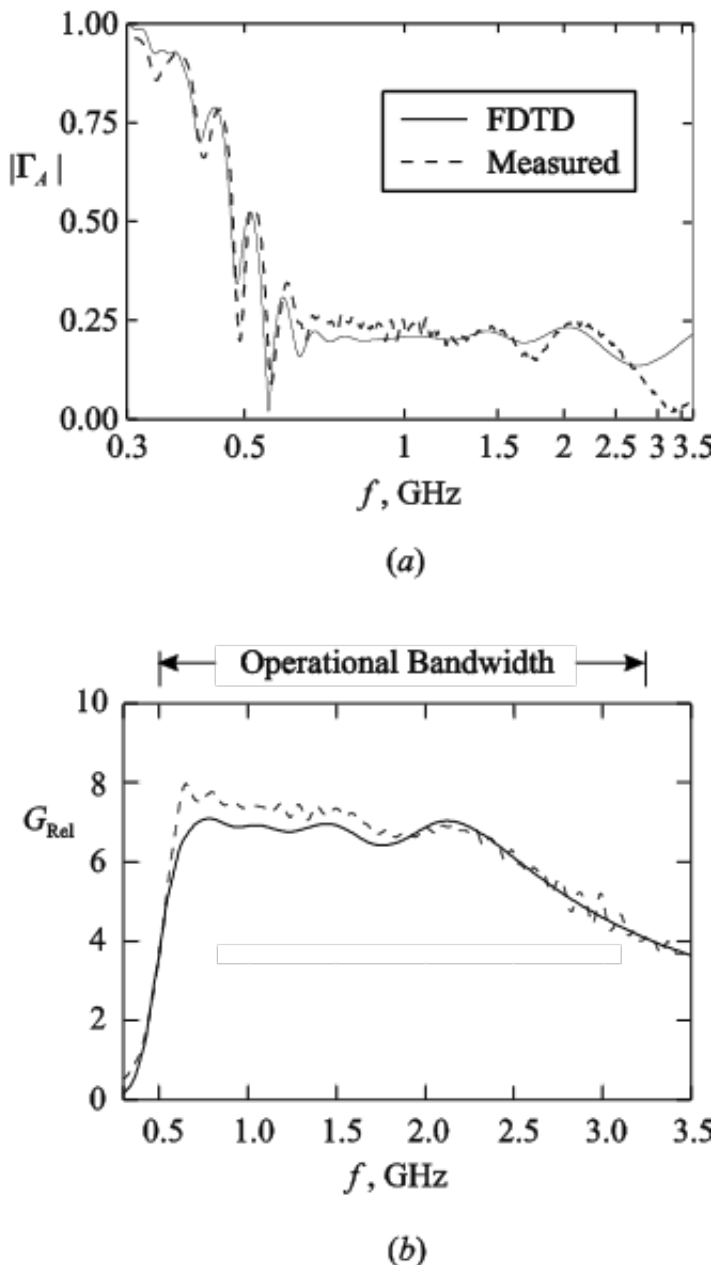


Figure A.19: Comparison of theoretical and measured results for the conical spiral antenna. (a) Magnitude of reflection coefficient versus frequency. (b) Realized gain in the boresite direction versus frequency. (After Hertel and Smith [26], 2002 IEEE.)

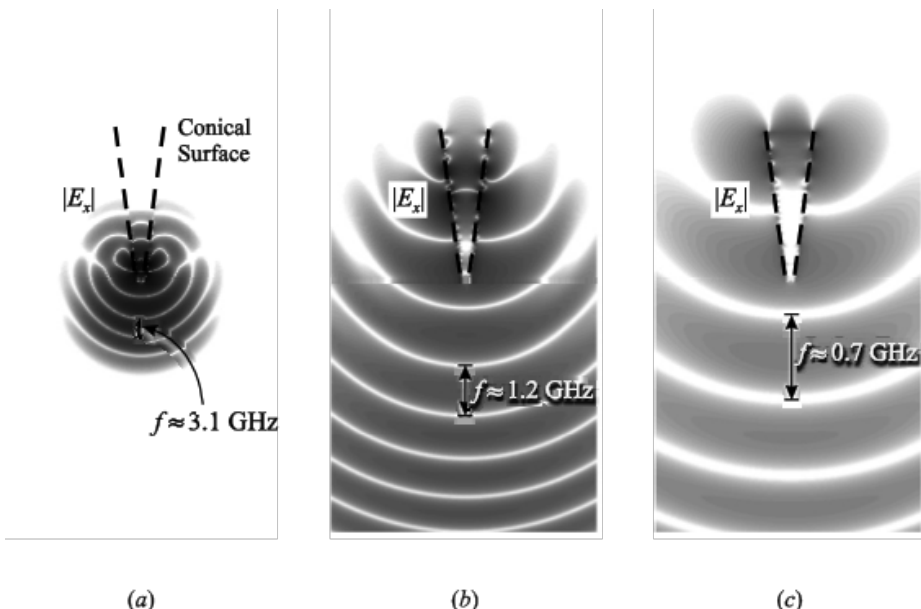


Figure A.20: Gray scale plots for the magnitude of the electric field near the conical spiral antenna for three instants in time: (a) $t/\tau_L = 0.1$, (b) $t/\tau_L = 0.6$, and (c) $t/\tau_L = 1.1$, where τ_L is the time for light to travel the length of the spiral arm. (After Hertel and Smith [27], 2003 IEEE.)

the x component of the electric field on the x-z plane. Each plot is for a different normalized time t/τ_L , where τ_L is the time for light to travel the length of the spiral arm. We can see that the radiation is roughly periodic with the spacing between the nulls (white lines) being $\lambda/2$. The frequency corresponding to this wavelength is indicated on each plot. These plots clearly show that the region from which radiation leaves the antenna changes with the wavelength, moving from the small end (diameter d) for the shortest wavelengths (highest frequencies) to the large end (diameter D) for the longest wavelengths (lowest frequencies). This is in keeping with the ?active-region concept,? which states that the radiation originates at the cross section of the spiral that is approximately one wavelength in circumference [28].

In the previous two examples, the stair-stepped approximations used for the geometry of the antennas in the FDTD models were adequate for obtaining theoretical results that were in good agreement with the measurements. This is a consequence of choosing the size of the steps to be small compared to the dimensions defining the geometry of the antennas. For example, for the pyramidal horn, the height of the stair step is only about 10% of the smallest dimension of the antenna (the height of the rectangular waveguide). We will now consider a case in which the stair-stepped approximation leads to significant errors in the calculated results.

The transverse electromagnetic (TEM) horn is a simple antenna used for applications that require broad bandwidth. The FDTD model for the monopole version of this

antenna is shown in Figure 21(a). It is formed from a PEC plate that is an isosceles triangle of side length s and angle at the apex α . The plate is inclined at the angle $\beta/2$ to the PEC image plane, and the antenna is fed by a transmission line connected between the apex of the plate and the image plane. The plate/image plane forms a TEM transmission line, and for the example to be discussed ($\alpha = 25.4^\circ$, $\beta = 11.2^\circ$), the characteristic impedance of this line is $R_o \approx 50\Omega$ [29]-[31]. The transmission line feeding the antenna has the same characteristic impedance.

The plate for this antenna is stair stepped in the FDTD model in the manner shown in Figure 21(b). Two different sizes for the staircase will be examined: Case A for which the rise is $\Delta z = 1\text{mm}$ and the tread length is $\Delta s = 1\text{cm}$, and case B for which $\Delta z = 2\text{mm}$ and $\Delta s = 2\text{cm}$. Notice that the level of discretization for case B is twice as coarse as that for case A. The smallest dimensions for the horn are at the drive point, where the initial tread for both cases is 4 mm above the image plane. So for case A, the rise of the staircase, Δz , is about 25% of the smallest dimension of the horn; whereas, for case B it is about 50% of the smallest dimension of the horn.

Figure 22(a) shows the reflected voltage, $V_t^-(t)$, in the feeding transmission line of the horn when the incident voltage, $V_t^+(t)$, is a unit-amplitude, differentiated Gaussian pulse (20) with the characteristic time $\tau_P = 5.31 \times 10^{-11}\text{s}$. The peak of the spectrum for the pulse is at 3.0 GHz. The solid line is for case A and the dashed line is for case B. The initial reflection from the drive point is evident and is similar for both cases, and the reflection from the open end of the horn has been windowed out. There is a pronounced ripple in the result for the coarser staircase, case B. The ripple is clearly due to the staircase, because its period roughly corresponds to the round trip time on a tread, which is $\Delta t = 2\Delta s_B/c \approx 2.5\tau_P$. Notice that the amplitude of the ripple decreases with time. This is because the reflections that occur later in time are from stair steps further out along the antenna, where the rise of the staircase, Δz , is a smaller fraction of the separation between the plate and the image plane.

Figure 22(b) shows the magnitude of the Fourier transform (spectrum) of the reflection coefficient for the antenna. Notice that the results for the two cases, A and B, are quite different. Specifically, for case B there is a distinct dip in the reflection coefficient near $2f\Delta s_B/c = 1$ ($f = 7.5\text{GHz}$). At this frequency, $\Delta s_B/\lambda = 1/2$, so the small reflections from all of the steps in the staircase add in phase.

To avoid the problem described above, we must use a finer staircase, such as in case A. For TEM horns with low characteristic impedance (generally small β), this can require a very fine level of discretization. A similar problem is encountered with bow-tie antennas with low characteristic impedance [32].

A.5.3 Microstrip Patches: Excessive Ringing for Narrow-Band Antennas

The antennas we examined in the previous section, a conical spiral and horns, are fairly wideband antennas. Now we will consider the other extreme, namely, narrowband antennas. For our example, we will use the basic, rectangular microstrip patch antenna shown in Figure 23.

In the mid 1980's, Chang et al. made extensive measurements of this antenna, and first we will compare our FDTD results with their measurements [33]. The dimensions

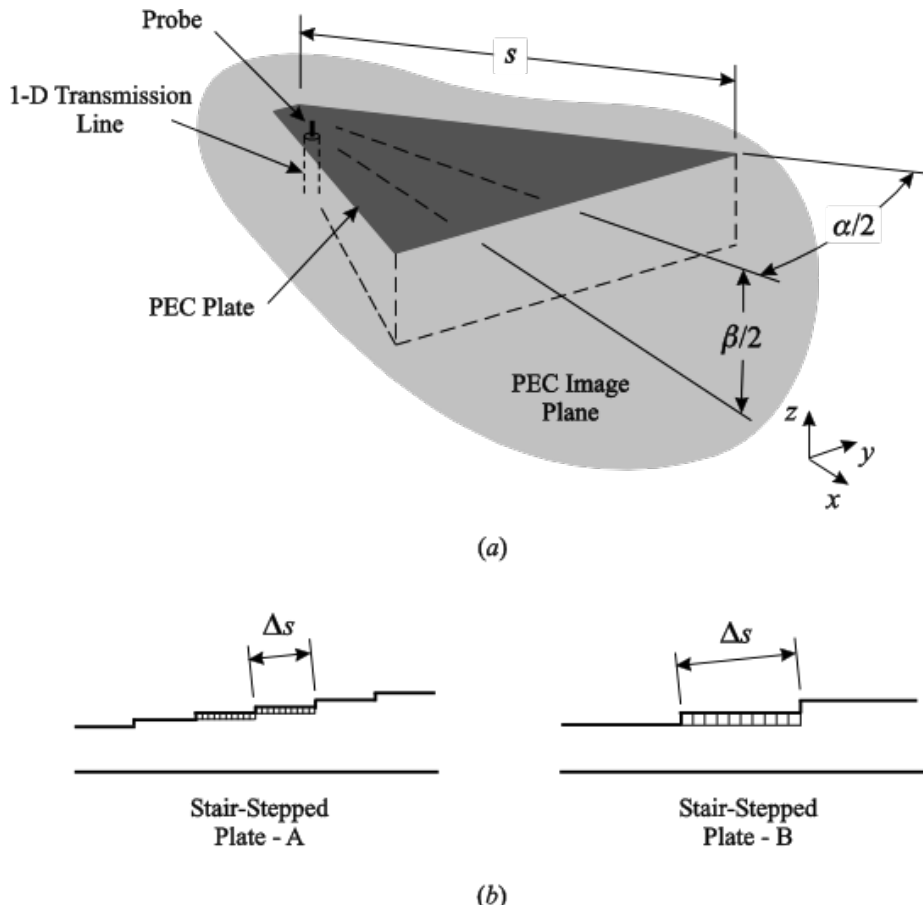


Figure A.21: (a) Schematic drawing for the TEM horn antenna (monopole configuration). (b) Cross sections showing the stair-stepped approximation to the plate for two different cases, A and B.

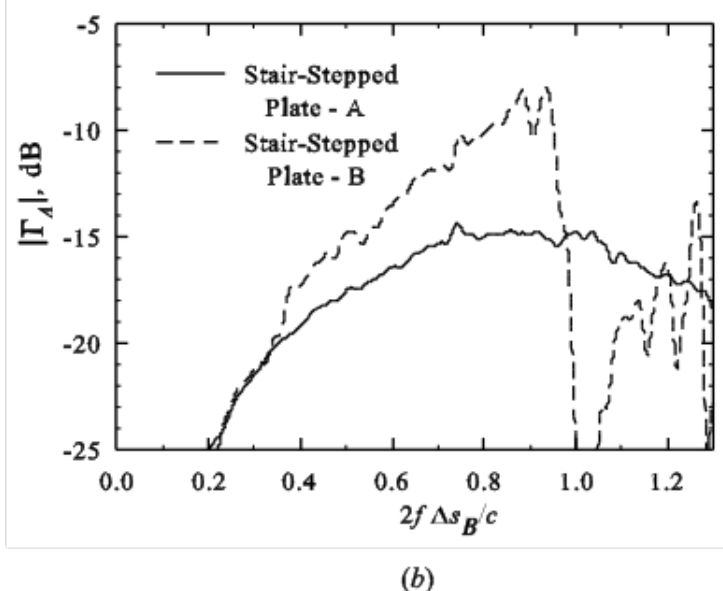
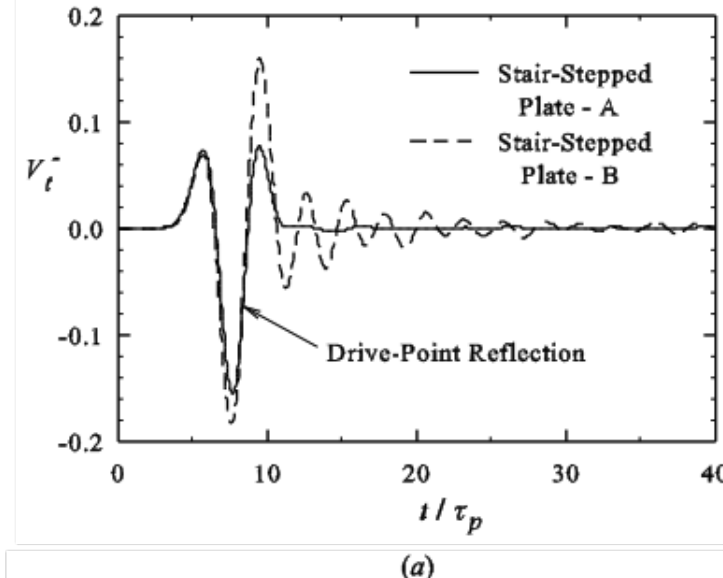


Figure A.22: Results for two different stair-stepped approximations (A and B) applied to the TEM horn antenna. (a) The reflected voltage in the feeding transmission line; the reflection from the open end of the horn has been windowed out. (b) The magnitude of the Fourier transform of the reflection coefficient for the antenna.

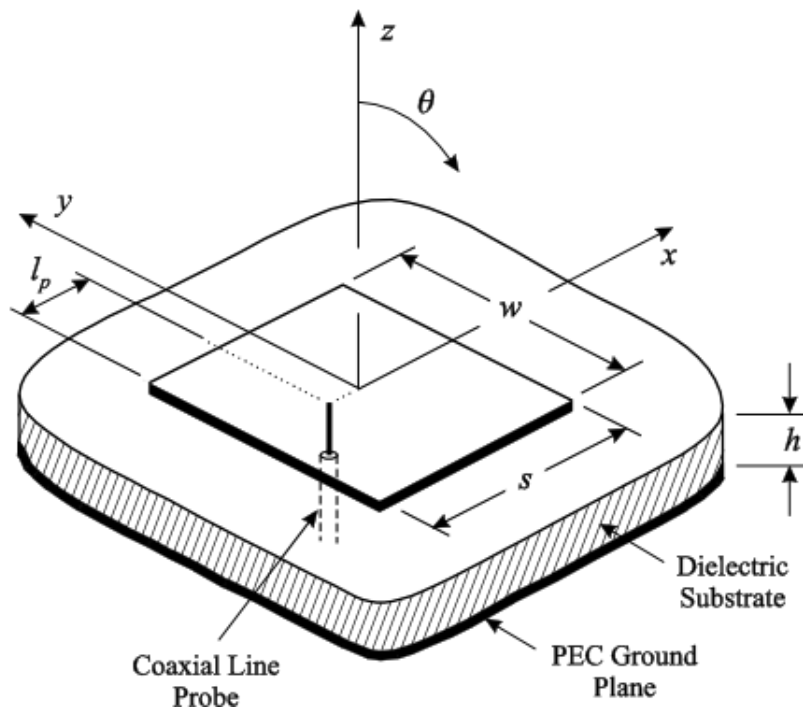


Figure A.23: Rectangular microstrip patch antenna fed by a coaxial line probe.

for a patch designed for frequencies around $f = 7.0$ GHz are $s = 1.1$ cm, $w = 1.7$ cm, and $h = 3.175$ mm. As shown in the figure, the probe of the feeding coaxial line ($R_o = 50\Omega$) is displaced from the broad side of the patch by $l_p = 1.5$ mm. In the model, the dielectric substrate is 10 cm x 10 cm with the electrical properties $\epsilon_r = 2.33$ and $\sigma = 2.1 \times 10^{-3}$ S/m, and the ground plane is infinite. The incident voltage, $V_t^+(t)$, in the feeding transmission line is a unit-amplitude, differentiated Gaussian pulse (20) with the characteristic time $\tau_P = 2.65 \times 10^{-11}$ s. The peak of the spectrum for this pulse is at 6.0 GHz.

The dimensions of the FDTD rectangular cells ($\Delta x = 0.529$ mm, $\Delta y = 0.500$ mm, $\Delta z = 0.500$ mm) were chosen so that all of the details of the coaxial feed line could be included in the model, and the time step was $\Delta t = 9.44 \times 10^{-13}$ sec. The number of time steps, N_t , required for the simulation was determined by observing the magnitude of the reflected voltage in the feeding transmission line versus the normalized time $t/\Delta t$; this is shown in Figure 24(a). Notice that the vertical scale is logarithmic. When $t/\Delta t = 3000$, the reflected voltage has dropped by six orders of magnitude from its peak, and it is at the noise level for the computation. So any number of time steps greater than three thousand was deemed adequate for the simulation ($N_t = 4000$ was actually used).

Figure 25 is a comparison of the FDTD theoretical results with the measurements. The graph in Figure 25(a) shows the magnitude of the reflection coefficient versus frequency: theory (solid line) and measurement (dots). The agreement is reasonably good, particularly when we consider that some of geometrical detail for the measurement, such as the precise geometry at the feed, were not known for use in the FDTD model.

The field patterns were measured with the 10 cm x 10 cm substrate mounted at the center of a circular aluminum image plane of diameter 1 m. We chose not to model this configuration with the same fine resolution used for the FDTD calculation of the reflection coefficient, because of the large amount of memory that would be required. Instead, larger cells were used with the dimensions $\Delta x = 1.59$ mm, $\Delta y = 1.42$ mm, $\Delta z = 1.57$ mm. The use of the larger cells causes little error in the far-zone field patterns. The FDTD and measured field patterns for the frequency $f = 6.8$ GHz are compared in Fig. 25(b). These plots show the gain (15) versus the angle θ , normalized to 0 dB at the peak. Results are given for both the E plane (x-z plane, solid line and dots) and the H plane (y-z plane, dashed line and triangles). Again the agreement is reasonably good.

For our second example, we chose a rectangular microstrip patch antenna designed to operate around $f = 1.9$ GHz that is similar to one reported in the literature [34]. The dimensions for the patch are $s = 5.12$ cm, $w = 6.0$ cm, and $h = 1.575$ mm, and the probe of the feeding coaxial line ($R_o = 50\Omega$) is displaced from the broad side of the patch by $l_p = 1.64$ cm. The dielectric substrate ($\epsilon_r = 2.2$ and $\sigma = 1.1 \times 10^{-3}$ S/m) and the ground plane are the same size: 11.5 cm x 11.5 cm. The incident voltage, $V_t^+(t)$, in the feeding transmission line is a unit-amplitude, differentiated Gaussian pulse (20) with the characteristic time $\tau_p = 1.061 \times 10^{-10}$ s, and the peak of the spectrum for this pulse is at 1.5 GHz. Again, the parameters for the FDTD simulation allow complete modeling of the details of the coaxial feed line ($\Delta x = 0.529$ mm, $\Delta y = 0.500$ mm, $\Delta z = 0.500$ mm), $\Delta t = 9.91 \times 10^{-14}$ sec.). The electrical thickness of the substrate

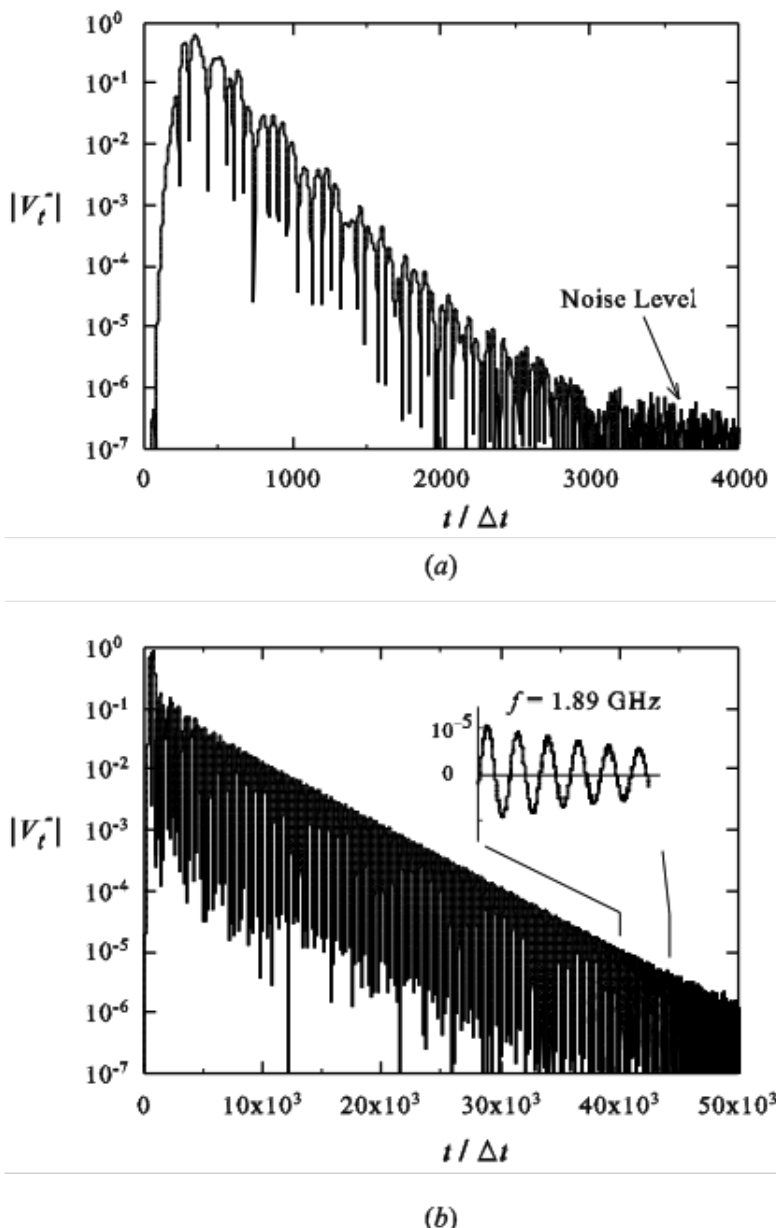


Figure A.24: The magnitude of the reflected voltage in the feeding coaxial line versus the normalized time. (a) Rectangular microstrip patch. (b) Narrow-band, rectangular microstrip patch.

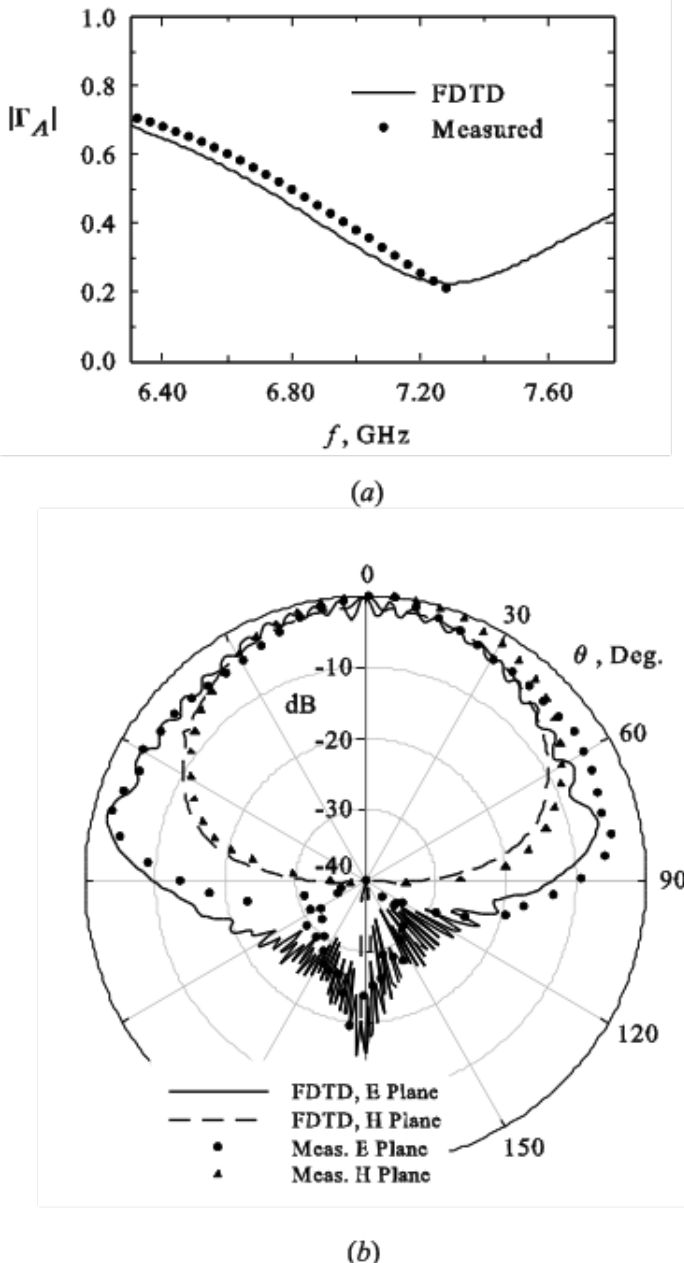


Figure A.25: Comparison of theoretical and measured results for the rectangular microstrip patch antenna. (a) Magnitude of reflection coefficient versus frequency. (b) Field patterns for E and H planes at the frequency $f = 6.8$ GHz. Measured results from [33]

for this example is about one eighth of that for the previous example, $h/\lambda = 0.010$ (for $f = 1.9$ GHz) versus $h/\lambda = 0.077$ (for $f = 7.3$ GHz), so we expect this antenna to have a significantly narrower bandwidth [35].

Figure 24(b) shows the magnitude of the reflected voltage $|V_t|$ in the feeding transmission line (logarithmic scale) versus the normalized time $t/\Delta t$. As a consequence of the narrower bandwidth, the reflected voltage decreases much more slowly with increasing $t/\Delta t$ than in the previous example, Fig. 24(a). The reflected voltage has dropped by six orders of magnitude from its peak and is approaching the noise level for the computation when $t/\Delta t = 50,000$. So about fifty thousand time steps ($N_t = 50,000$) are required for the simulation, as compared to three thousand for the previous example! The inset in the Fig. 24(b) shows the magnitude of the reflected voltage, plotted on a linear scale, for times around $t/\Delta t = 40,000$. The voltage is seen to be a slowly decaying sinusoid at the frequency $f \approx 1.89$ GHz.

In Fig. 26 we show the magnitude of the reflection coefficient versus frequency for simulations with different numbers of time steps: $N_t = 8,000$, $N_t = 24,000$, and $N_t = 50,000$. For each case, a Hanning window is applied in time to eliminate truncation artifacts. The antenna is seen to be matched at the frequency $f = 1.89$ GHz, and the “apparent” bandwidth for the match is seen to depend on the number of time steps used for the simulation. Thus, if one were to underestimate the number of time steps required for the simulation to converge, one would think that the antenna had a much wider bandwidth for the reflection coefficient than it actually has. With the detailed analysis presented above, this point may appear to be obvious. However, sometimes, particularly when a computation is automated, this degree of analysis may not be performed every time a parameter for the antenna, such as the thickness of the substrate, is changed.

In some cases, special techniques can be applied to shorten the computation for a narrow bandwidth antenna. For example, because of the well-defined, decaying sinusoidal waveform in the reflection coefficient for this antenna, a shorter computation time, say $N_t = 20,000$, could be used with an extrapolation for the remainder of the waveform. Such techniques are discussed in the literature [36].

A.6 Summary and Conclusions

In this chapter, we have presented an introduction to the finite-difference time-domain method, aimed at individuals who have little or no experience with the method. Thus, we have limited the presentation to the basics of the method, and we have avoided mention of many refinements that are generally restricted to particular applications. To give the reader a sense of the breadth of application allowed by these refinements we present a partial list below.

- Techniques for handling materials with dispersive properties (properties that are a function of the frequency), anisotropic properties (properties that depend on the direction of the field components), and nonlinear properties.
- Methods for incorporating impedance boundary conditions.
- Subcell methods for treating material sheets that are thinner than a FDTD cell.

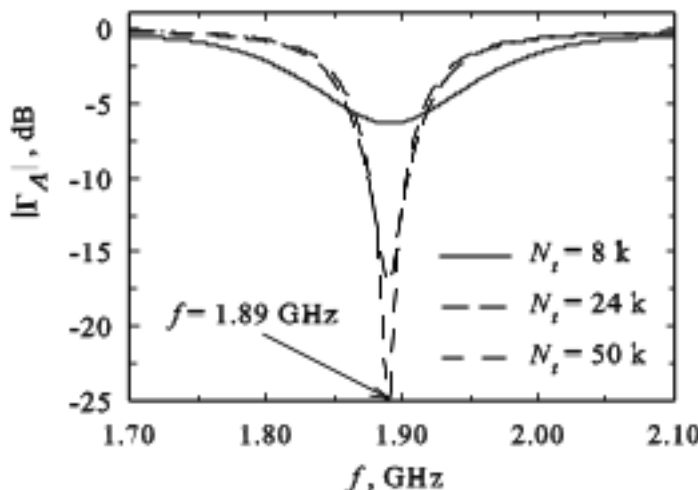


Figure A.26: Narrow-band, rectangular microstrip patch antenna. Magnitude of reflection coefficient versus frequency for three different numbers of time steps.

- Methods for incorporating periodic boundary conditions, which are useful in treating antenna arrays.
- Higher order FDTD schemes that have lower error (numerical dispersion) than the conventional Yee algorithm.
- Techniques for incorporating nonuniform and nonorthogonal grids.
- Special procedures for handling objects that are bodies of revolution.

The brevity of the contribution precluded the derivation of the mathematical formulas associated with the method, e.g., FDTD update equations, equations for the perfectly matched layer, etc. These formulas can be found in the in-depth treatment of the method contained in the book edited by A. Taflove and S. C. Hagness [9]. A comprehensive web site on the method is maintained by J. B. Schneider at Washington State University: www.fDTD.org. This site contains searchable lists of books, journal papers, conference papers, and dissertations.

To assess the popularity of the FDTD method, a search was done with INSPEC for documents that included either “finite-difference time-domain” or “FDTD” in the title⁴. The results of the search, presented in Fig. 27, clearly show the rapid growth in the popularity of the method over the last twenty-five years.

⁴A few of these documents apply the finite-difference time-domain method to problems other than electromagnetic, such as acoustic problems.

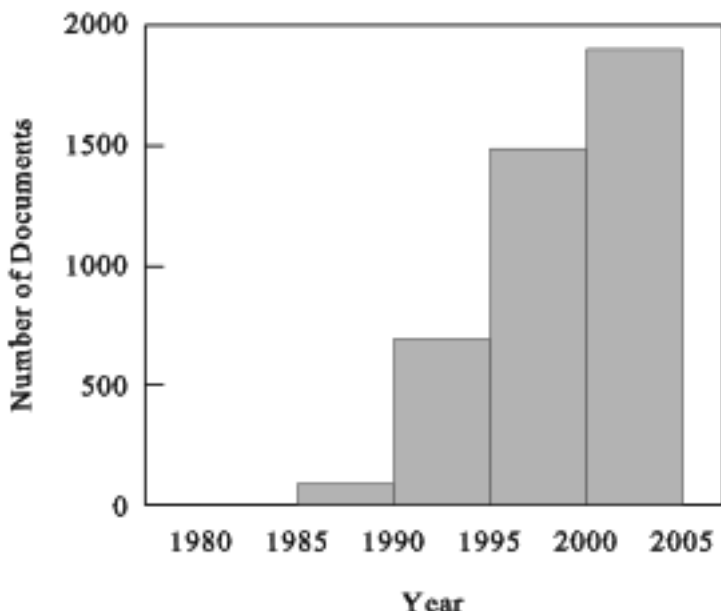


Figure A.27: Number of documents published over the a twenty year span that include the words ?finite-difference time-domain? or ?FDTD? in the title. Each bar shows the total number of documents published during a five year period.

The emphasis throughout the chapter has been on the application of the FDTD method to the analysis of antennas. After brief discussions of the special formulations associated with transmitting and receiving antennas, the details for the analysis of a few different types of antennas were presented. Again, because of the brevity of the contribution, no attempt was made to mention all of the different antennas that have been analyzed with the method. Many individuals have used the method to treat antennas; as an indication of the number, the INSPEC search mentioned above listed over 500 documents with FDTD and antenna(s) in the title.

All of the numerical results presented in the examples were obtained by us or our students. Thus, we have very detailed knowledge for each example, and can make fairly accurate statements about the results. These examples were chosen not only to show the power of the FDTD method, particularly the good agreement with experimental measurements, but also to show that the method has some limitations; albeit, the limitations are sometimes due to the crudeness of the theoretical model for the antenna or the choice of the parameters for the simulation. The refinement of the FDTD method and its application to practical problems is an ongoing story. Undoubtedly, there will be some exciting accomplishments made in the future.

One area with great promise is the use of the method for antenna synthesis. Here we do not mean the conventional approach in which the method is coupled with an optimization routine and used to choose the parameters for a standard antenna (dipole, horn, etc.) so that certain criteria for the performance are met. What we have in mind for antenna synthesis is a quite different, a more modern approach. In this approach, the structure of the antenna is not completely predetermined with only a few parameters to be chosen, but the structure of the antenna is actually developed as part of the synthesis! The FDTD method is well suited for use in such schemes; because of the flexibility of the method, a new structure can easily be introduced. The antenna structure is changed by simply changing the electromagnetic constitutive parameters associated with individual cells. *The early chapters in this book discussed the "fragmented aperture" concept which relied heavily on the FDTD method as described in this chapter [37]-[40].*

References

- [1] K. S. Yee, "Numerical Solution of Initial Boundary Value Problems Involving Maxwell's Equations in Isotropic Media," IEEE Trans. Antennas Propagat., Vol. AP-14, pp. 302-307, May 1966.
- [2] J. G. Maloney, G. S. Smith, and W. R. Scott, Jr., "Accurate Computation of the Radiation from Simple Antennas Using the Finite-Difference Time-Domain Method," IEEE Trans. Antennas Propagat., Vol. AP-38, pp. 1059-1068, July 1990.
- [3] J. J. Boonzaaier and C. W. Pistorius, "Thin Wire Dipoles: A Finite-Difference Time-Domain Approach," Electronics Lett., Vol. 26, pp. 1891-1892, 25 October, 1990.

- [4] D. S. Katz, M. J. Picket-May, A. Taflove, and K. R. Umashankar, "FDTD Analysis of Electromagnetic Wave Radiation from Systems Containing Horn Antennas," *IEEE Trans. Antennas Propagat.*, Vol. AP-39, pp. 1203-1212, August 1991.
- [5] P. A. Tirkus and C. A. Balanis, "Finite-Difference Time-Domain Method for Antenna Radiation," *IEEE Trans. Antennas Propagat.*, Vol. AP-40, pp. 334-340, March 1992.
- [6] R. J. Luebbers and J. Beggs, "FDTD Calculation of Wide-Band Antenna Gain and Efficiency," *IEEE Trans. Antennas Propagat.*, Vol. AP-40, pp. 1403-1407, November 1992.
- [7] J. G. Maloney and G. S. Smith, "Modeling of Antennas," Chapter 7 in A. Taflove, Editor, *Advances in Computational Electrodynamics, The Finite-Difference Time-Domain Method*, pp. 409-460, Artech House, Boston, 1998. Also, J. G. Maloney, G. S. Smith, E. Thiele, O. Ghandi, N. Chavannes, and S. Hagness, Chapter 14 in A. Taflove, and S. Hagness, Editors, *Computational Electrodynamics: The Finite-Difference Time-Domain Method*, 3rd Edition, pp. 607-676, Artech House, Boston, 2005.
- [8] , G. S. Smith, *An Introduction to Classical Electromagnetic Radiation*, Cambridge University Press, Cambridge, UK, 1997.
- [9] A. Taflove and S. C. Hagness, Editors, *Computational Electrodynamics: The Finite-Difference Time-Domain Method*, Artech House, Boston, 2005.
- [10] J. B. Schneider and C. L. Wagner, "FDTD Dispersion Revisited: Faster-Than-Light Propagation," *IEEE Microwave and Guided Wave Lett.*, Vol. 9, pp. 54-56, Feb. 1999.
- [11] S. Gedney, "An Anisotropic Perfectly Matched Layer-Absorbing Medium for the Truncation of FDTD Lattices," *IEEE Trans. Antennas Propagat.*, Vol. AP-44, pp. 1630-1639, December 1996.
- [12] S. Gedney, "Perfectly Matched Layer Absorbing Boundary Conditions," Chapter 7 in A. Taflove and S. C. Hagness, Editors, *Computational Electrodynamics: The Finite-Difference Time-Domain Method*, 3rd Edition, pp. 273-328, Artech House, Boston, 2005.
- [13] K. L. Shlager and G. S. Smith, "Near-Field to Near-Field Transformation for Use With FDTD Method and Its Application to Pulsed Antenna Problems," *Electronics Lett.*, Vol. 30, pp. 1262-1264, 4th, August, 1994.
- [14] K. L. Shlager and G. S. Smith, "Comparison of Two Near-Field to Near-Field Transformations Applied to Pulsed Antenna Problems" *Electronics Lett.*, Vol. 31, pp. 936-938, 8th, June, 1995.
- [15] G. S. Smith, "A Direct Derivation of a Single-Antenna Reciprocity Relation for the Time Domain," *IEEE Trans. Antennas Propagat.*, Vol. AP-52, pp. 1568-1577, June 2004.

- [16] J. G. Maloney, M. P. Kesler, and G. S. Smith, "Generalization of PML to Cylindrical Geometries," 13th Annual Review of Progress in Applied Computational Electromagnetics, Monterey, CA, pp. 900-908, March 1997.
- [17] G. S. Smith and T. W. Hertel, "On the Transient Radiation of Energy from Simple Current Distributions and Linear Antennas," IEEE Antennas Propagat. Magazine, Vol. 43, pp. 49-62, June 2001.
- [18] T. W. Hertel and G. S. Smith, "On the Convergence of Common FDTD Feed Models for Antennas," IEEE Trans. Antennas Propagat., Vol. AP-51, pp. 1771-1779, August 2003.
- [19] R. W. P. King, The Theory of Linear Antennas, pg. 20, Harvard Univ. Press, Cambridge, MA, 1956.
- [20] J. G. Maloney, K. L. Shlager, and G. S. Smith, "A Simple FDTD Model for Transient Excitation of Antennas by Transmission Lines," IEEE Trans. Antennas Propagat., Vol. AP-42, pp. 289-292, February 1994.
- [21] S. Dey and R. Mittra, "A Locally Conformal Finite-Difference Time-Domain (FDTD) Algorithm for Modeling Three-Dimensional Perfectly Conducting Objects," IEEE Microwave and Guided Wave Lett., Vol 7, pp. 273-275, September 1997.
- [22] A. Taflove, M. Celuch-Marcysiak, and S. Hagness, "Local Subcell Models of Fine Geometrical Features," Chapter 10 in A. Taflove and S. C. Hagness, Editors, Computational Electrodynamics: The Finite-Difference Time-Domain Method, 3rd Edition, pp. 407-462, Artech House, Boston, 2005.
- [23] S. Gedney, F. Lansing, and N. Chavannes, "Nonuniform Grids, Nonorthogonal Grids, Unstructured Grids, and Subgrids," Chapter 11 in A. Taflove and S. C. Hagness, Editors, Computational Electrodynamics: The Finite-Difference Time-Domain Method, 3rd Edition, pp. 463-516, Artech House, Boston, 2005.
- [24] A. C. Cangellaris and D. B. Wright, "Analysis of the Numerical Error Caused by the Stair-Stepped Approximation of a Conducting Boundary in FDTD Simulations of Electromagnetic Phenomena," IEEE Trans. Antennas Propagat., Vol. AP-39, pp. 1518-1525, October 1991.
- [25] R. Holland, "Pitfalls of Staircase Meshing," IEEE Trans. Electromagnetic Compatibility, Vol. 35, pp. 434-439, November 1993.
- [26] T. W. Hertel and G. S. Smith, "Analysis and Design of Two-Arm Conical Spiral Antennas," IEEE Trans. Electromagnetic Compatibility, Vol. 44, pp. 25-37, February 2002.
- [27] T. W. Hertel and G. S. Smith, "On the Dispersive Properties of the Conical Spiral Antenna and Its Use for Pulsed Radiation," IEEE Trans. Antennas Propagat., Vol. AP-51, pp. 1426-1433, July 2003.

- [28] J. D. Dyson, "The Characteristics and design of the Conical Log-Spiral Antenna," IEEE Trans. Antennas Propagat., Vol. AP-13, pp. 488-499, July 1965.
- [29] K. L. Shlager, G. S. Smith, and J. G. Maloney, "Accurate Analysis of TEM Horn Antennas for Pulse Radiation," IEEE Trans. Electromagnetic Compatibility, Vol. 38, pp. 414-423, August 1996.
- [30] R. T. Lee and G. S. Smith, "On the Characterteristic Impedance of the TEM Horn Antenna" IEEE Trans. Antennas Propagat., Vol. AP-52, pp. 315-318, January 2004.
- [31] R. T. Lee and G. S. Smith, "A Design Study for the Basic TEM Horn Antenna," IEEE Antennas Propagat. Magazine, Vol. 46, pp. 86-92, February 2004.
- [32] K. L. Shlager, G. S. Smith, and J. G. Maloney, "Optimization of Bow-Tie Antennas for Pulse Radiation," IEEE Trans. Antennas Propagat., Vol. AP-42, pp. 975-982, July 1994.
- [33] E. Chang, S. A. Long, and W. F. Richards, "An Experimental Investigation of Electrically Thick Rectangular Microstrip Antennas," IEEE Trans. Antennas Propagat., Vol. AP-34, pp. 767-772, June 1986.
- [34] H. Abdallah, W. Wasylkiwskyj, K. Parikh, and A. Zaghloul, "Comparison of Return Loss Calculations with Measurements of Narrow-Band Microstrip Patch Antennas," ACES Journal, Vol. 19, pp. 184-186, November 2004.
- [35] D. R. Jackson and N. G. Alexopoulos, "Simple Approximate Formulas for the Input Resistance, Bandwidth, and Efficiency of a Resonant Rectangular Patch," IEEE Trans. Antennas Propagat., Vol. AP-39, pp. 407-410, March 1991.
- [36] S. Chebolu, R. Mittra, and W. D. Becker, "The Analysis of Microwave Antennas Using the FDTD Method," Microwave Journal, Vol. 39, pp. 134-150, January 1996.
- [37] J.G. Maloney, P.H. Harms, M.P. Kesler, T.L. Fountain, and G.S. Smith, "Novel, Planar Antennas Designed Using the Genetic Algorithm," 1999 USNC/URSI Radio Science Meeting, Orlando, FL, pg. 237, July 1999.
- [38] J.G. Maloney, M.P. Kesler, P.H. Harms, T.L. Fountain, and G.S. Smith, "The Fragmented Aperture Antenna: FDTD Analysis and Measurement," Millennium Conference on Antennas and Propagation (AP 2000), Davos, Switzerland, 4 pages, April 2000.
- [39] J.G. Maloney, M.P. Kesler, P.H. Harms, and G.S. Smith, Fragmented Aperture Antennas and Broadband Ground Planes, U.S. Patent, No. 6,323,809 B1, November 27, 2001.
- [40] L. N. Pringle, P. H. Harms, S. P. Blalock, G. N. Kiesel, E. J. Kuster, P. G. Friederich, R. J. Prado, J. M. Morris, and G. S. Smith, "A Reconfigurable Aperture Antenna Based on Switched Links Between Electrically Small Metallic Patches," IEEE Trans. Antennas Propagat., Vol. AP-52, pp. 1434-1445, June 2004.

- [41] Balanis HB, Chapter ?